Magnetorotational core collapse of possible GRB progenitors – II. Formation of protomagnetars and collapsars

M. Á. Aloy [1]⋆ and M. Obergaulinger [1,2]

[1] *Departament d'Astronomia i Astrofísica, Universitat de València, Edifici d'Investigació Jeroni Munyoz, C/ Dr. Moliner, 50, E-46100 Burjassot (València), Spain*
[2] *Institut für Kernphysik, Theoriezentrum, S2|11 Schloßgartenstr. 2, D-64289 Darmstadt, Germany*

ABSTRACT

We assess the variance of the post-collapse evolution remnants of compact, massive, low-metallicity stars, under small changes in the degrees of rotation and magnetic field of selected pre-supernova cores. These stellar models are commonly considered progenitors of long gamma-ray bursts. The fate of the protoneutron star (PNS) formed after the collapse, whose mass may continuously grow due to accretion, critically depends on the poloidal magnetic field strength at bounce. Should the poloidal magnetic field be sufficiently weak, the PNS collapses to a black hole (BH) within a few seconds. Models on this evolutionary track contain promising collapsar engines. Poloidal magnetic fields smooth over large radial scales (e.g. dipolar fields) or slightly augmented with respect to the original pre-supernova core yield long-lasting PNSs. In these models, BH formation is avoided or staved off for a long time, hence, they may produce protomagnetars (PMs). Some of our PM candidates have been run for $\lesssim 10$ s after core bounce, but they have not entered the Kelvin–Helmholtz phase yet. Among these models, some display episodic events of spin-down during which we find properties broadly compatible with the theoretical expectations for PMs ($M_{\rm PNS} \approx 1.85-2.5\,{\rm M_\odot}$, $\bar{P}_{\rm PNS} \approx 1.5-4$ ms, and $b_{\rm PNS}^{\rm surf} \lesssim 10^{15}$ G) and their very collimated supernova ejecta have nearly reached the stellar surface with (still growing) explosion energies $\gtrsim 2 \times 10^{51}$ erg.

Key words: MHD – methods: numerical – gamma-ray burst: general – stars: magnetic field – supernovae: general.

1 INTRODUCTION

The collapse of the core of a massive and sufficiently fast rotating star is needed to form the central engine of a long gamma-ray burst (GRB; for a review, see, e.g., Kumar & Zhang 2015). Likely, the first stage, namely the formation of a protoneutron star (PNS) and the generation of a shock wave at its surface is common to all except for possibly the most massive stars that directly produce black holes (BHs). During the subsequent period of up to several seconds, neutrinos streaming out of the PNS transfer energy to the gas behind the stalled shock wave and, together with hydrodynamic instabilities, rotation and magnetic fields, favour shock revival. If no explosion sets in, or if it proceeds asymmetrically, the PNS may accrete matter until its mass exceeds the upper limit for stability against self-gravity and it collapses to a BH that will continue to accrete the inner layers of the star. The delay before this secondary collapse is negatively correlated with the mass of the PNS at its birth and with the mass accretion rate, both of which depend on the progenitor structure. Otherwise, the PNS formed in the collapse will gradually cool and transform into a young neutron star.

The long-term evolution can branch into additional directions besides those of failed or successful core-collapse supernovae (CCSNe) with a PNS or a BH at the centre. Both a rapidly rotating and strongly magnetized PNS, commonly termed protomagnetar (PM;

see, e.g. Metzger et al. 2011, 2015), and a system consisting of a BH and an accretion torus generated by a core with sufficiently high angular momentum (a collapsar; Woosley, Langer & Weaver 1993) can launch collimated, relativistic outflows that will produce a GRB after they breakout from the stellar surface.

Stellar evolution modelling suggests that the conditions tend to be most favourable for long GRBs in stars of fairly high masses (e.g. Woosley & Heger 2006; Yoon, Langer & Norman 2006). It should be noted, though, that the results of current stellar evolution calculations do not lend themselves to simple rules connecting, e.g. the zero-age main-sequence mass, $M_{\rm ZAMS}$, of the star and its pre-collapse profiles of density, composition, and temperature (but see, e.g. Woosley, Sukhbold & Janka 2020). Those profiles and, in particular, the size of the iron core and the surrounding shells at collapse play an important role in determining the fate of the stellar remnant, as demonstrate systematic studies of core collapse across a large range of stellar masses in spherically symmetric and multidimensional simulations (O'Connor & Ott 2011; Janka 2012; Ugliano et al. 2012; Nakamura et al. 2015; Bruenn et al. 2016; Sukhbold et al. 2016; Ertl et al. 2020; Woosley et al. 2020). O'Connor & Ott (2011) found a useful, yet simple (one dimensional) criteria for distinguishing cores that are likely to explode from those where a failed explosion leads to BH formation in terms of the compactness of the core. However, the compactness criterion neither accounts for rotation nor for the dynamical effects of magnetic fields in the pre-collapsed stellar cores.

One of the most important constraints on the formation of the central engine of long GRBs comes from the requirement of high

⋆ E-mail: miguel.a.aloy@uv.es

angular momentum in the progenitor star. Including rotation in stellar evolution modelling, which is mostly based on spherically symmetric calculations, is non-trivial and depends on many approximations. Nevertheless, several sets of models for rotating pre-collapse cores exists, among which the ones by Woosley & Heger (2006) are most valuable for our purpose as they account for the effect of magnetic fields redistributing angular momentum. Other groups have also computed the evolution of fast-rotating main sequence, low metallicity, single stars systematically predicting rather fast-rotating pre-collapse cores (e.g. Yoon & Langer 2005; Woosley & Heger 2006; Meynet & Maeder 2007; Ekström et al. 2012; Aguilera-Dena et al. 2018). Therefore, we focus here on low-metallicity stars. Rapid rotation can add centrifugal support to the PNS and stabilize it beyond the maximum mass for non-rotating PNSs, besides leading to global asymmetries of the PNS. These effects are most pronounced when rotation is combined with a strong magnetic field that can tap into the rotational energy (see, e.g. Bisnovatyi-Kogan, Popov & Samokhin 1976; Symbalisty 1984; Akiyama et al. 2003; Kotake et al. 2004; Thompson, Quataert & Burrows 2005; Moiseenko, Bisnovatyi-Kogan & Ardeljan 2006; Obergaulinger, Aloy & Müller 2006a; Obergaulinger et al. 2006b; Burrows et al. 2007; Dessart et al. 2007; Winteler et al. 2012; Sawai, Yamada & Suzuki 2013; Mösta et al. 2014, 2015; Obergaulinger & Aloy 2017, 2020a; Bugli et al. 2020; Kuroda et al. 2020). Large-scale fields are most effective at generating jet-like explosions (e.g. Wheeler et al. 2000; Uzdensky & MacFadyen 2007; Dessart et al. 2008; Bugli et al. 2020; Obergaulinger & Aloy 2020b), whereas small-scale fields such as those amplified by turbulence driven by, e.g. the magnetorotational instability (MRI, e.g. Balbus & Hawley 1998), can act as effective viscosity and enhance the heating of the post-shock gas (Thompson et al. 2005). It should, however, be noted that the dynamic relevance of the magnetic field depends crucially on the ratio of the magnetic energy to the kinetic energy, which in most, though not all, typical pre-collapse cores is expected to be rather small (e.g. Meier et al. 1976; Obergaulinger, Janka & Aloy 2014). Hence, processes that amplify the seed field such as flux-freezing compression, winding by the differential rotation, dynamos driven by the MRI or hydrodynamic instabilities are important ingredients to the overall picture (Akiyama et al. 2003; Obergaulinger et al. 2009; Masada et al. 2012; Mösta et al. 2015; Rembiasz et al. 2016a,b,c; Raynaud et al. 2020; Reboul-Salze et al. 2020).

Most studies involving the central engines of long GRBs start from cores where a PM or a system consisting of a BH and an accretion torus are set up by hand in a stellar core rather than from the results of self-consistent simulations of the processes leading up to the formation of those central engines (though with some remarkable exceptions; MacFadyen & Woosley 1999; MacFadyen, Woosley & Heger 2001). Starting from these initial conditions, the GRB engines are then investigated using theoretical analysis and numerical simulations with typically somewhat simplified microphysics in the case of collapsars (Aloy et al. 2000; Proga et al. 2003; Zhang, Woosley & MacFadyen 2003; Zhang, Woosley & Heger 2004; Proga 2005; Lee & Ramirez-Ruiz 2006; Mizuta et al. 2006; Morsony, Lazzati & Begelman 2007, 2010; Nagataki et al. 2007; Barkov & Komissarov 2008; Harikae, Takiwaki & Kotake 2009; Mizuta & Aloy 2009; Nagakura et al. 2011; Lazzati et al. 2013; López-Cámara et al. 2013; Nagakura 2013; López-Cámara, Morsony & Lazzati 2014; Cuesta-Martínez et al. 2015a; Cuesta-Martínez, Aloy & Mimica 2015b; Ito et al. 2015; Batta & Lee 2016; Bromberg & Tchekhovskoy 2016; López-Cámara, Lazzati & Morsony 2016; Aloy, Cuesta-Martínez & Obergaulinger 2018) and of PMs (Wheeler et al. 2000; Zhang & Mészáros 2001; Thompson,

Chang & Quataert 2004; Bucciantini et al. 2007, 2008, 2009, 2012; Burrows et al. 2007; Metzger, Thompson & Quataert 2007; Metzger et al. 2011, 2015)

In a first paper of this series (Obergaulinger & Aloy 2020a, Paper I), we have explored the outcomes of the stellar collapse of cores that may produce the central engine of long GRBs. There, we have focused on the criteria that decide whether small variations of the initial magnetorotational conditions in the stellar progenitor shape the ensuing supernova explosion (or the lack thereof). In this paper, the goal is to understand whether relatively small variations of the magnetorotational profile in the progenitor star determine the final fate of the compact remnant left after core collapse. We restrict our analysis here to rapidly rotating, low-metallicity stars. More specifically, we focus on the following issues:

(i) How sensitive is the type of central engine to *small* variations in the magnetic field topology and strength? Do *small* variations of the pre-collapse rotational profile change the type of the post-collapse compact remnant?

(ii) Can collapsars or PMs be produced given the rotation rates and, in particular for PMs, also magnetic fields predicted by stellar evolution modelling?

The open issues at the centre of our interest depend sensitively on a multitude of closely coupled physical effects, suggesting that they may be addressed by numerical simulations incorporating an accurate treatment of the evolution of MHD and neutrino transport. Therefore, our simulations are based on a state-of-the-art code combining high-order methods for solving the hyperbolic terms of the MHD and transport equations with a post-Newtonian treatment of gravity, as well as a spectral two-moment neutrino transport including corrections due to the velocity (Doppler shifts, aberration) and the gravitation field (gravitational blue/redshift) and the relevant reactions between neutrinos and matter. The neutrino transport, though less costly than, e.g., a full Boltzmann solver, is the computationally most expensive part of the simulations. Its high cost together with the long simulation times we want to reach and the variety of models limit us in most cases to axisymmetric models. Aware that the final answers can only come from unrestricted three-dimensional (3D) models, in order to qualitatively assess the validity of our axisymmetric simulations, we will show the results of low-resolution 3D models for two cases, which are prototypes of collapsar- and PM-forming central engines.

The work by Dessart, O'Connor & Ott (2012) represents a milestone in determining the viability of the formation of a GRB engine from the class of stars we are considering here. It presented simulations of the collapse of a star of $M_{\text{ZAMS}} = 35 \, \text{M}_\odot$ (in fact, one of the stars we are studying) including magnetohydrodynamics (MHD) and neutrino transport. The results suggested a high likelihood of fairly early magnetorotational explosions that inhibit the further growth of the PNS, thus preventing the formation of a collapsar for rapidly rotating cores. Here, we extend the Dessart et al. (2012) study by including additional models, by using improved neutrino physics, and by considering very long simulation times.

This article is organized as follows. We begin describing our initial models and parameters in Section 2, carefully justifying the modifications on the original stellar progenitor properties performed (see also Appendix A). Section 3 describes our results separating models into two classes, namely, BH- and NS-forming models. The long-term evolution after core bounce is specifically considered in Section 4, again distinguishing between BH- and NS-forming models. For the latter ones, we carefully assess whether the PM model of Metzger et al. (2011) (hereafter, M11) is fulfilled. We provide a

small overview of two 3D models that have been run at relatively low resolution and until less than a second post-bounce (Section 5). Finally, Section 6 contains our conclusions and discussion of our results.

2 INITIAL MODELS AND PARAMETERS

The simulations that follow were performed using the neutrino-MHD code presented in Just, Obergaulinger & Janka (2015). With respect to the description of the algorithms, implementation, and tests given there (and in Rembiasz et al. 2017) and to the previous application in simulations of magnetized core collapse (Obergaulinger et al. 2014), we made several modifications for the purpose of running the present set of models. These modifications have already been used in the closely related publication (Obergaulinger & Aloy 2017), as well as in the exploration of magnetorotational collapse of lower mass and solar metallicity progenitors Obergaulinger, Just & Aloy (2018) and the effects of the multipolar structure of large-scale magnetic fields in the outcome of core collapse of low-metallicity, high mass stars (Bugli et al. 2020). We refer to Paper I for a detailed list of all these modifications and an extended description of the microphysics and numerical methods. Our code includes a general relativistic approximate gravitational potential, Φ as in Marek et al. (2006). This allows us to define a lapse function as $\alpha := \exp(\Phi/c^2)$, where c is the light speed in vacuum. Operatively, we say that a BH has formed when either $\alpha < \alpha_{\mathrm{th}} := 0.4$ at $r = 0$ or the maximum density, ρ_{max} is larger than $\rho_{\mathrm{th}} := 1.1 \times 10^{15}\,\mathrm{g}\ \mathrm{cm}^{-3}$. We note that when α and ρ_{max} approach the operative threshold values α_{th} and ρ_{th}, respectively, the dynamics at the centre speeds up very quickly. In a matter of a few time-steps α may sink to values below 10^{-8} and the central density rise to values $\sim 10^{16}\,\mathrm{g}\ \mathrm{cm}^{-3}$, where the equation of state employed (LS220 with a suitable extension to low densities below $\rho_{\mathrm{low}} = 6 \times 10^7\,\mathrm{g}\ \mathrm{cm}^{-3}$; Paper I, section 2.1) is no longer causal.

We focus on model 35OC, which was computed by Woosley & Heger (2006) as a model for a rapidly rotating star of zero-age main-sequence mass $M_{\mathrm{ZAMS}} = 35\,\mathrm{M}_\odot$ including the redistribution of angular momentum by magnetic fields according to the model of Spruit (2002). At collapse, the star retains a mass of $M_{\mathrm{preSN}} \simeq 28.07\,\mathrm{M}_\odot$ and possesses an iron core of mass $M_{\mathrm{Fe}} = 2.02\,\mathrm{M}_\odot$, radius $R_{\mathrm{Fe}} \approx 3000\,\mathrm{km}$, and central density of $\rho_c \approx 2.4 \times 10^9\,\mathrm{g}\ \mathrm{cm}^{-3}$. The core rotates differentially with angular velocities of $\Omega_{\mathrm{PC,c}} \approx 1.98\,\mathrm{s}^{-1}$ at the centre and $\Omega_{\mathrm{PC,Fe}} \approx 0.1\,\mathrm{s}^{-1}$ at the surface of the iron core. Another initial model with the same ZAMS mass as model 35OC has been employed, namely model 35OB (sections 3.1.4 and 3.1.5 in Woosley & Heger 2006, $M_{\mathrm{preSN}} \simeq 21.2\,\mathrm{M}_\odot$) The latter model is not supposed to produce a collapsar central engine (it does not rotate fast enough). However, we place it among the grid of computed models because it provides an initial profile, which differs *sufficiently* from 35OC so as to assess the influence of the stellar progenitor structure in the final outcome, especially, on the formation of BHs accompanied with successful SN explosions.

We map the pre-collapse structure of the core (computed in one spatial dimension), viz. the hydrodynamic variables such as density, electron fraction, temperature, and rotational velocity, on to our simulation grid. The magnetic field of the model is the result of MHD instabilities. Hence, it is not a global, e.g. dipole field encompassing the entire star, but rather confined to several shells. We simulate a series of models based on the field as given by the pre-collapse model and an additional series of models in which we replace the field by a global dipole field and a toroidal component.[1] The details on the exact initialization of the magnetic field can be found in Paper I as well as in Appendix A. Within each of the two series, we vary the normalization of the poloidal and toroidal components, and, in the first series, also their angular distribution. In order to assess the importance of rotation, we add a version of the same model with an artificially reduced angular velocity. Table 1 provides a summary of the most important properties of our models.

Modifying the stellar profiles of rotation or of magnetic field is an artificial manipulation intended to probe the impact of these two factors on the dynamics. In reality, a change of the rotational velocity would most likely entail changes of the density, thermodynamical, and composition profiles of the core. However, given the uncertainties in stellar evolution modelling regarding the treatment of mass-loss, angular momentum transport and other magnetic processes (see, e.g. Maeder & Meynet 2012; Keszthelyi et al. 2019), we assume that there is some room for (small) variations of the aforementioned rotational and magnetic profiles. A more consistent treatment would require computing a relatively dense grid of stellar evolution models *ab initio*, changing slightly the parameters that control the aforementioned effects of rotation, magnetic fields and mass-loss, but this is beyond the scope of this paper. We stress, however, that even without modifying the magnetic field in the stellar evolution models, the mapping from these 1D progenitors to our multidimensional computational grid is not unique and may introduce a significant variation in the post-bounce evolution (see Appendix A).

The numerical grids and initialization employed here are the same as in Paper I. All models have been simulated on spherical grids. In axially symmetric models, the mesh consisted of $n_\theta = 128$ zones in θ-direction and $n_r = 400$ radial zones with a width given in terms of a parameter $(\delta_r)_0 = 600\,\mathrm{m}$, $\delta r = \max\{(\delta r)_0, r\pi/n_\theta\}$. In energy space, we used $n_\epsilon = 10$ energy bins distributed logarithmically between $\epsilon_{\mathrm{min}} = 3\,\mathrm{MeV}$ and $\epsilon_{\mathrm{max}} = 240\,\mathrm{MeV}$. In 3D, we use a grid with $(n_r, n_\theta, n_\phi) = (300, 64, 128)$ zones, i.e. with a similar effective radial resolution in the PNS and its surroundings but with a coarser angular grid than in the axisymmetric models.

We display in Fig. 1 the distribution of specific angular momentum, j, for the different variants of the stellar progenitor models 35OC and 35OB. The original profile of angular momentum (Fig. 1a) is employed in, e.g. models 35OC-RO, 35OC-RO2, 35OC-Rp2, 35OC-Rp3, etc. (see Table 1), while slower and faster rotation is assumed in models 35OC-Sw (Fig. 1b) and 35OC-RRw (Fig. 1c), respectively. In each of the panels, we also display the angular momentum needed to support matter in the last stable (circular) orbit (LSO) for either a non-rotating (blue dashed lines) or maximally rotating Kerr BH (dashed yellow lines) with a mass equal to that enclosed by the mass coordinate annotated in the abscissa axis. Also, a red line marks the specific angular momentum at the LSO for a rotating Kerr BH with a mass and angular momentum equal to those enclosed by the mass coordinate in the progenitor star.[2] It is (roughly) expected that where the red line lies below the black line, matter in the star may have enough angular momentum to form an accretion disc (Woosley & Heger 2006). We denote the Lagrangian

---

[1] Large-scale dipolar fields have been inferred from spectropolarimetric observations of massive stars, e.g. in the O stars θ^1 Ori C (Donati et al. 2002) or HD 191612 (Donati et al. 2006).
[2] We employ the formulae of Bardeen, Press & Teukolsky (1972) to compute the corresponding angular momentum.

Table 1. List of our axisymmetric models. Each simulation is listed with its name and the progenitor star. The third column indicates the rotational frequency at $r = 0$ and the type of the rotation profile (in parenthesis): 'Or' stands for the original profile taken from the stellar evolution calculation, and $\times n$ means that we multiplied the original angular velocity by a uniform factor n. The fourth column similarly shows the magnetic field strength at $r = 0$ in units of 10^8 G, as well as the type of magnetic field: 'Or' indicates the magnetic field profile of the original stellar evolution model, xp, yt means that the original poloidal and toroidal fields have been multiplied by factors x and y, respectively, and a(x, y) stands for an artificial dipolar field with maximum poloidal and toroidal field components of 10^x and 10^y G, respectively. The fifth column, 'fate', gives a brief indication of the evolution of the model: ν means a standard neutrino-driven shock revival, ν-Ω one strongly affected by rotation, MR is a magnetorotational explosion, and $\times$ is a failed explosion. The sixth column shows the sign $\checkmark$ if a BH formed during the simulation, $+$ if it did not, but we consider its formation likely on time-scales of seconds after the end of the simulation, and $\times$ if no BH was formed and we estimate the final remnant to be an NS. The fate of model 350C-Rw is unclear, hence we annotate it with a question mark. The seventh to ninth columns provide the accretion disc formation time (equation 1), the corresponding Lagrangian mass coordinate for disc formation (M_{DF}), and the maximum mass available for the ejecta computed as $M_e^{max} := M_{preSN} - M_{DF}$, respectively. The tenth and eleventh columns list the pre-SN magnetic and rotational energy in units of 10^{47} and 10^{49} erg, respectively. The twelfth column corresponds to the binding energy of the pre-SN envelope (defined by the layers of the star at a distance larger than 2000 km from the centre). The last two columns provide proxy values for the explosion mass (M_{exp}) and of the explosion energy E^{exp} (in units of 10^{51} erg) two seconds after bounce or, alternatively, at the final time of the simulation if BH formation occurs before $t = 2$ s.

Name	Star	$\Omega(r)$ (Hz)	B-field (10^{11} G)	Fate	BH	t_{DF} (s)	M_{DF} ($M_\odot$)	M_e^{max} ($M_\odot$)	$\mathcal{B}_{47}$	$\mathcal{T}_{49}$	$\|E_{52}^{bd}\|$	M_{exp} ($M_\odot$)	E_{51}^{exp}
350C-RO	350C	1.98 (Or)	1.1, Or	MR	$\checkmark$	9.3	7.5	20.6	70.0	17.4	2.84	0.18^a	1.03^a
350C-RO2	350C	1.98 (Or)	2.2, p, 2t	MR	$\checkmark$	9.3	7.5	20.6	279	17.4	2.84	0.32^a	1.39^a
350C-Rp2	350C	1.98 (Or)	1.3, 2p, 1t	MR	$\times$	9.3	7.5	20.6	82.5	17.4	2.84	0.44	1.96
350C-Rp3	350C	1.98 (Or)	1.5, 3p, 1t	MR	$\times$	9.3	7.5	20.6	103	17.4	2.84	0.57	2.66
350C-Rp4	350C	1.98 (Or)	1.8, 4p, 1t	MR	$\times$	9.3	7.5	20.6	132	17.4	2.84	0.57	3.22
350C-Rw	350C	1.98 (Or)	0.10, a(10, 10)	ν-Ω	?	9.3	7.5	20.6	0.0134	17.4	2.84	0.21^a	0.67^a
350C-Rs	350C	1.98 (Or)	10, a(12, 12)	MR	$\times$	9.3	7.5	20.6	135	17.4	2.84	1.42	5.60
350C-Sw	350C	0.49 ($\times$1/4)	10^{-3}, a(8, 10)	ν	$\checkmark$	42.9	22.8	5.27	0.0134	1.1	2.89	0.26^a	1.67^a
350C-RRw	350C	2.97 ($\times$ 1.5)	1.1×10^{-6}, Or/10^6	ν-Ω	$\times$	2.9	3.14	24.9	3.5×10^{-12}	69.5	2.84	0.034	0.21
350B-RO	350B	1.54 (Or)	0.64, Or	ν-Ω	$\checkmark$	37.4	17.3	3.9	34.7	0.47	1.11	0.13^a	0.82^a
350B-RRw	350B	3.09 ($\times$ 2)	6.4×10^{-7}, Or/10^6	$\times$	$+$	15.3	10.0	11.2	1.2×10^{-12}	3.88	1.12	$\times$	$\times$

^{a}Values in these two columns are shown by the time of BH formation.
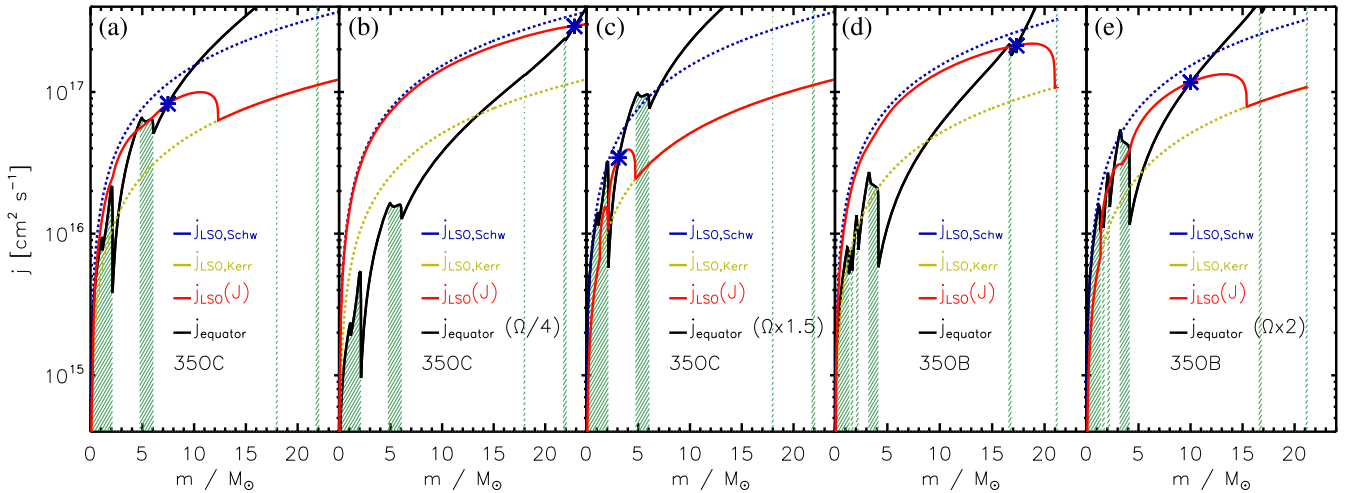

Figure 1. Equatorial profile of the initial specific angular momentum (black lines) of the models with the same rotational profile as the progenitor star 35OC (panel a), with one-fourth of the rotational frequency of the stellar progenitor (panel b; e.g. corresponding to model 350C-Sw), and with 1.5 times the rotational frequency of the stellar progenitor (panel c; e.g. corresponding to model 350C-RRw). Panels (d) and (e) correspond to the specific angular momentum of models 350B-RO and 350B-RRw, respectively. In each panel, the blue dashed lines denote the angular momentum needed to support matter at the LSO for a Schwarzschild BH, while the yellow dashed lines are for a Kerr BH with dimensionless spin $a = 1$. The red lines indicate the specific angular momentum at the LSO for a BH with the mass and angular momentum inside the displayed mass coordinate in the pre-SN star. The green-hatched parts of the plot denote the mass shells of the pre-SN star with the non-zero magnetic field.

mass coordinate of this point M_{DF}. This estimation of M_{DF} does not account for the post-bounce dynamics, which may transport angular momentum altering the pre-SN specific angular momentum profile.

If disc formation takes place after the central compact remnant collapses to a BH, a collapsar engine may result. In order to estimate the disc formation time, t_{DF}, we assume it equals twice the free-fall time of the innermost mass element that reaches a Keplerian velocity

(e.g. Dessart et al. 2012), thus

$$t_{DF} = 2\pi \sqrt{\frac{r_{preSN}^3(M_{DF})}{8GM_{DF}}}, \qquad (1)$$

where $r_{preSN}(M_{DF})$ is the radius of the disc-forming Lagrangian mass element in the pre-SN model. The value of t_{DF} for the outermost

Lagrangian mass coordinate that satisfies the criteria to form an accretion disc are listed in Table 1.

In model 35OC-RO, with the original specific angular momentum distribution, there are two mass shells where a disc may form, namely $4.4 \lesssim M_{DF}/M_\odot \lesssim 5.7$ or for $M_{DF} \gtrsim 7.5\,M_\odot$. We mark the outermost point where the standard disc formation criterion holds with a blue asterisk in Fig. 1. In the model with reduced angular frequency (Fig. 1b), $M_{DF} \sim 22.8\,M_\odot$, while the model with faster rotational speed than the pre-SN star the whole progenitor beyond $M_{DF} \sim 2.9\,M_\odot$ may produce an accretion disc. The mass of the star above $r_{preSN}(M_{DF})$ is available for the SN ejecta. We list the maximum available SN ejecta mass (corresponding to $M_{preSN} - M_{DF}$) in Table 1. Note that this is only a rough estimate since, (i) a fair fraction of the aforementioned mass may fall back on to the central compact object on sufficiently long time-scales (especially if the SN explosion is asymmetric and allows for simultaneous mass accretion and ejection), and (ii) not necessarily all the mass up to M_{DF} may necessarily end up in the central compact object; a fraction of it may be incorporated into the outflow ejecta by the action of Maxwell stresses or neutrino heating. This means that between ~ 20.6 and $\sim 23.6\,M_\odot$ may be ejected for the original rotational profile of model 35OC-RO. The *exact* amount depending on whether the accretion disc forms above 4.4 or $7.5\,M_\odot$. For the fast rotating version of the pre-SN star, a larger fraction of the star ($\sim 24.9\,M_\odot$) could be ejected. In the case of the slowly rotating model 35OC-Sw, only $\sim 5.3\,M_\odot$ could be unbound as SN ejecta. Considering that the ejecta mass in typical Type Ic SN may feature a broad range (say, $M_{ejecta} \sim 1-10\,M_\odot$; e.g. Taubenberger et al. 2006), and the fact that the mass remaining above the potential disc formation mass coordinate is only an upper bound for the SN ejecta mass (see above), even the models with modified rotational profiles may yield an ejecta mass *broadly* compatible with observational estimates. In Table 1, we show the proxy values computed for the mass ejected by the successful SN explosions. These values are still small compared to the rough estimates provided above. In part, this is because, with the exception of model 35OC-Rp2 and 35OC-Rp3, the rest of the models have been evolved only for $t_{pb} := t - t_{bounce} \lesssim 3\,s$ after bounce. The strong magnetorotational explosion of model 35OC-Rs stands out of the rest with an ejecta mass $\sim 1.4\,M_\odot$ after only $t_{pb} \approx 2.3\,s$.

We finally notice that the pre-SN models display an alternated pattern of magnetized (green hatched regions in Fig. 1) and un-magnetized mass shells. This is due to the presence of convective layers in the evolved stars, where the standard angular momentum transport by magnetic torques have not been applied. Indeed, in our stellar models, $\lesssim 15$ per cent of the total pre-SN mass contains non-zero magnetic field. Most of the magnetized mass shells are located within $M_B \lesssim 6\,M_\odot$ ($\lesssim 4\,M_\odot$) in model 35OC (35OB), which means that they could free-fall in times $\lesssim 7\,s$ ($\lesssim 3.9\,s$), as obtained from application of equation (1) to the corresponding mass shell (i.e. replacing M_{DF} by M_B).

3 RESULTS

In this section, we describe the dynamics of the 2D (axisymmetric) models grouping them into models that form or may form a BH and models which do not form BHs.

3.1 BH-forming models

First, we show the most salient properties of the dynamical evolution of models which either form a BH during the computed period of time or may likely form one if they were evolved long enough. We consider *collapsar candidates* or proto-collapsars (PCs) all models that collapse (or may shortly collapse) to a BH surrounded by matter with sufficient angular momentum to form an accretion disc, irrespective of the spin parameter of the BH itself.

3.1.1 Model 35OC-RO with the original magnetic field

We evolved model 35OC-RO, using the rotational profile and the magnetic field of the stellar evolution model, from the onset of collapse to a final time of $t_{pb} = 3.22\,s$ when the core forms a BH. The model launches an explosion relatively shortly after bounce with a shock runaway that sets in at $t_{pb} \approx 150\,ms$. Afterwards, the PNS continues to accrete mass until the end of the simulation (see Fig. 2a).

Overview of the post-bounce dynamics: The phase until $t_{pb} \approx 150\,ms$ is characterized by accretion through the shock at all latitudes and, hence, a growth of the PNS mass at an initially large, albeit decreasing rate of $\dot{M}_{PNS} > 1\,M_\odot\,s^{-1}$ (see Fig. 2b). After the onset of the explosion, the mass accretion rate remains positive, though it decreases considerably after the accretion of the surface of the inner core at a mass coordinate of $M_{Fe} \approx 2.1\,M_\odot$ (Fig. 2b). The PNS takes about 1.5 s to reach a mass in excess of the maximum cold, non-rotating PNS mass for our EOS $M_{PNS} > M_{bry}^{max} = 2.45\,M_\odot$ (Fig. 2a; see also below). As the PNS contracts and its density increases, most its mass resides in the interior shells of higher density. At $t_{pb} = 1.5\,s$, for instance, almost 80 per cent of the PNS mass has a density higher than $10^{14}\,g\,cm^{-3}$, and the mass contained in the surrounding shells decreases with their density, but remains significant for all shells throughout the evolution (Fig. 3b). The high rotational energy leads to a notable deformation after core bounce as we displayed by the time evolution of the values of several radii characterizing the PNS, viz. the electron-neutrino sphere and the radii of the iso-density surfaces corresponding to $\rho = 10^{11}$ and $10^{12}\,g\,cm^{-3}$ (Fig. 3a). The evolution of the electron–neutrino sphere radii parallels the evolution of the iso-density surfaces corresponding to $10^{11}\,g\,cm^{-3}$, indicating that both radii are excellent proxies of the actual PNS radius. We also display in Fig. 3(a) the time evolution of the radius of a spherical and homogeneous configuration with the same mass and moment of inertia than the PNS, defined as

$$R_{PNS,I} := \left(\frac{5 I_{PNS}}{2 M_{PNS}} \right)^{1/2}. \tag{2}$$

The time evolution of this radius shows a big similarity with the polar radius tracking the isodensity surface of $10^{12}\,g\,cm^{-3}$, especially after $t \sim 0.1\,s$. With relatively small variations, the behaviour of $R_{PNS,I}$ is quite similar in nearly all models considered in this paper.

Supported throughout the entire evolution partially by rotation, the PNS possesses an oblate shape with maximum and minimum radii located at the equator and at the poles, respectively, (Figs 4b and c). The maximum radius of the newly formed PNS exceeds its minimum radius by about 10 per cent. The asymmetry leaves an imprint in the neutrino burst, whose total luminosity of $L_\nu \approx 6.3 \times 10^{53}\,erg\,s^{-1}$ shows the same level of pole-to-equator asymmetry. In the phase leading up to the onset of the explosion, the deformation is moderate, and so is the pole-to-equator difference of the neutrino fluxes. Nevertheless, this moderate degree of asymmetry (at $t_{pb} = 150\,ms$, the neutrino flux along the poles exceeds that at the equator by about 30 per cent) is sufficient to focus enough of the neutrino flux into cones around the poles and heat the gas efficiently enough to revert the infall. From this moment on, the accretion on to the PNS proceeds predominantly through the equatorial region.
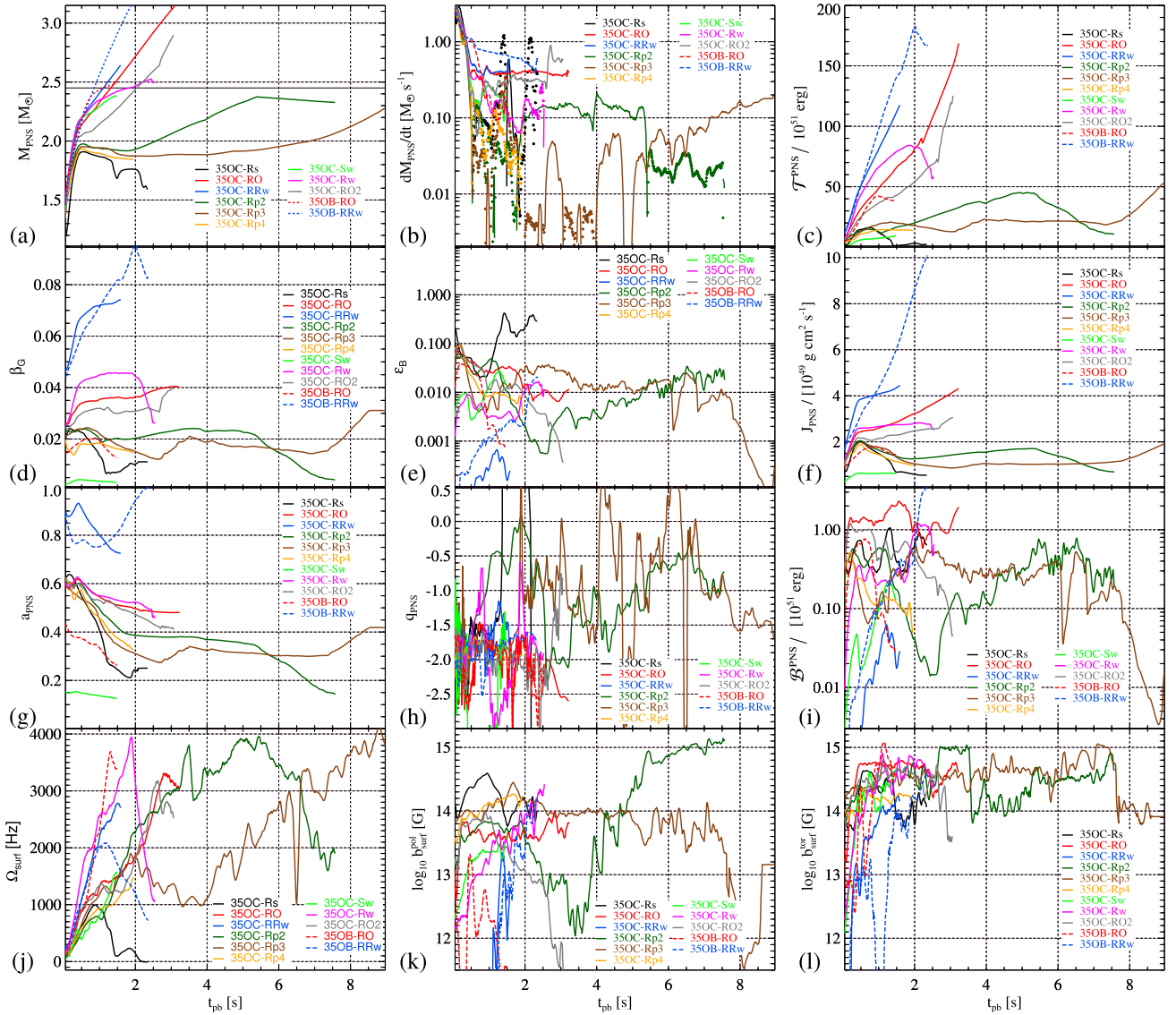
Figure 2. Selected global variables of our models. The variables shown are the time evolution of (panel a) the mass of the PNS (marked with a grey horizontal line is the value of M_{bry}^{max}), Panel b: its mass accretion rate (with solid lines $\dot{M}_{PNS} > 0$, denoting mass gain by the PNS, and with symbols $\dot{M}_{PNS} < 0$, implying mass-loss from the PNS), panel (c) its rotational energy, panel d: the ratio rotational to gravitational energy of the PNS (β_G; equation 3), panel (e): the ratio magnetic to rotational energy (ϵ_B; equation 4), Panel (f): the angular momentum of the PNS, Panel (g): the corresponding dimensionless spin parameter (equation 5), Panel (h): the power-law index q_{PNS} (equation 9), Panel (i): the magnetic energy of the PNS, Panel (j): the PNS surface-averaged rotational frequency, Panel (k): the PNS surface-averaged poloidal magnetic field component, and Panel (l): the PNS surface-averaged toroidal magnetic field component.

The kinetic energy is dominated by the rotational energy in our models. As the PNS accretes matter, its rotational energy ($\mathcal{T}^{PNS}$) grows (Fig. 2c), leading to an increase of the degree of asphericity. The ratio of rotational ($\mathcal{T}^{PNS}$) to gravitational potential binding energy ($\mathcal{W}^{PNS}$) in the PNS

$$\beta_G := \mathcal{T}^{PNS}/|\mathcal{W}^{PNS}|, \qquad (3)$$

tends to increase non-monotonically with time. The growth first levels off approximately when $\beta_G \sim 0.035$, but later ($t_{pb} \gtrsim 2$ s) continues to a final value of $\beta_G \sim 0.04$ (see panel d of Fig. 2). The magnetic energy ($\mathcal{B}$; Fig. 2i) increases at a rate smaller than that of $\mathcal{T}^{PNS}$, as can be observed from the decreasing trend of the ratio ϵ_B (Fig. 2e), defined as

$$\epsilon_B := \mathcal{B}^{PNS}/\mathcal{T}^{PNS}. \qquad (4)$$

Stability of the hypermassive PNS: The mass of the PNS at the time of BH formation by far exceeds, M_{bry}^{max}, value that our model 35OC-RO exceeds after $t_{pb} \sim 1.2$ s. After that time, the PNS is stabilized by a fast rotation. We cannot disregard that the produced PNS may be unstable to non-axisymmetric instabilities (Andersson 2003), resulting in an earlier collapse to form a BH in 3D (the evolution computed in 3D for this model is still insufficient to make any forecast of its final fate; see Section 5). Among the former instabilities, the existence of dynamical bar modes, which happen when the ratio β_G becomes large enough ($\beta_G > 0.24 - 0.25$ according to Shibata, Baumgarte & Shapiro 2000) has been thoroughly studied in the literature (see also, e.g. Watts, Andersson & Jones 2005; Saijo & Yoshida 2006). However, in magnetized, differentially rotating polytropes (with properties resembling cold neutron stars), Franci et al. (2013) find that the dynamical bar mode instability is largely suppressed if the magnetic field is able to grow to very
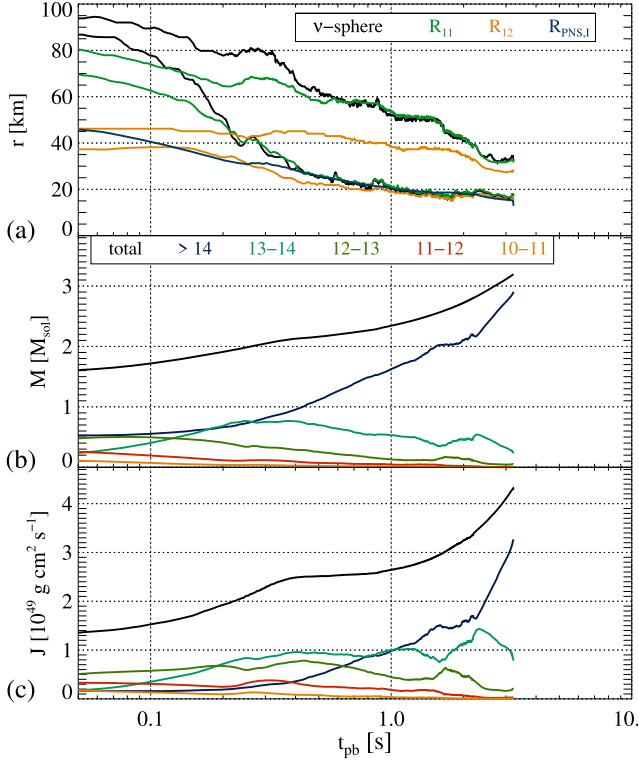
Figure 3. Further global quantities of model 35OC-RO. Panel (a) shows the evolution of three proxies for the PNS radii: the black, green, and orange pairs of lines display the maximum and minimum radii of the electron-neutrinosphere, and the iso-density surfaces of $\rho = 10^{11}$ and 10^{12} g cm^{-3}, respectively. We also include a (blue) line showing the evolution of $R_{PNS,I}$ (equation 2). Panel (b) mass of all matter with densities in different ranges as indicated in the legend. Panel (c) is same the as panel (b), but for angular momentum.

large values $\gtrsim 10^{16}$ G (a result also found by Camarda et al. 2009). Moreover, Fujisawa (2015) points out that if a magnetized polytrope possesses a high degree of differential rotation, the toroidal magnetic field wound up from the poloidal one becomes highly localized near the rotational axis. As a result, the 'low-β_{G}' instability, which happens for highly differentially rotating non-magnetized stars for $\beta_{G} \sim 0.14$ (e.g. Centrella et al. 2001), is more efficiently suppressed than that of stars without differential rotation and toroidal magnetic field. It must be noted that the toroidal magnetic field configurations considered in Fujisawa (2015) are strictly symmetric with respect to the equatorial plane, while we do not enforce equatorial symmetry in our models. This topological difference may impact the equilibrium states discussed by Fujisawa (2015). Furthermore, the initial poloidal magnetic field is ~50 times weaker than the toroidal one in model 35OC-RO. Thus, the suppression of the 'low-β_{G}' instability is not guaranteed by the mechanism suggested by Fujisawa (2015). Nevertheless, we observe a significant rise of the toroidal field around the rotational axis (where the poloidal and toroidal components reach typical values $\gtrsim 10^{15}$ G; see also Fig. 4). This enhancement of the toroidal field around the axis helps stabilizing the 3D versions of models 35OC-RO and 35OC-Rs (Section 5). The general relativistic MHD simulations of Muhlberger et al. (2014) pointed out that when the total magnetic to total kinetic energy ratio is as small as $\epsilon_{B} \simeq 5.6 \times 10^{-3}$ the 'low-β_{G}' instability is significantly suppressed. In model 35OC-RO, $\epsilon_{B} \simeq 9 \times 10^{-4}$ at the end of the computed evolution, with maximum values, $\epsilon_{B} \lesssim 0.1$ reached soon after the collapse (Fig. 2e). Hence, in this particular model, it is likely that the
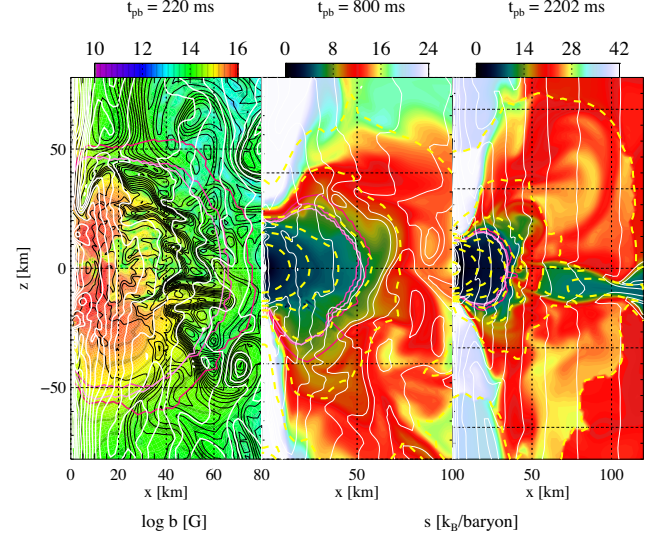
'low-β_{G}' instability is significantly damped. As a matter of fact, the 3D version of model 35OC-RO does not display signs of a strong instability during the first second of post-bounce evolution during which the values of β_{G} are even smaller than in 2D (see Section 5). Moreover, the values of ϵ_{B} in the 3D counterpart of model 35OC-RO show that the PNS of the former is as magnetized as that of the latter. Hence, our results (both in 2D and in 3D) support to the possibility that sufficiently magnetized collapsed cores tend to hinder large changes of the PNS structure due to the 'low-β_{G}' instability.

Muhlberger et al. (2014) further found that the *numerical* growth rate of the instability is quite sensitive to the formal order of the convergence of the numerical method: high-order methods (e.g. WENO5) render considerably slower growth rates than low-order ones. Since our models are computed also with a fifth-order accurate intercell reconstruction, we also expect the 'low-β_{G}' instability to be marginally growing in our models.

Properties of the remnant at the brink of BH collapse: The mass of the PNS at the time of BH formation,[3] $M_{PNS} \approx 3.19\,M_{\odot}$, can be taken as the initial BH mass, which may latter grow due to fall-back accretion. We note that the mass infall rate on to the PNS remains nearly constant during the last ≈ 2 s prior to BH collapse (Fig. 2b). At the same time the dimensionless spin parameter

$$a_{PNS} := c J_{PNS}/(G M_{PNS}^2), \qquad (5)$$

moderately decreases up to a final value $a_{PNS} \approx 0.48$ (Fig. 2g). This value is close to the expectations of Woosley & Heger (2006), who predict $a \simeq 0.53$ for model 35OC-RO. Thus, the BH is not extremely rapidly rotating. The specific angular momentum of the layers, still to be accreted by it, may nevertheless be sufficiently large for an accretion torus to form after $t_{DF} \simeq 9.3$ s (Table 1) and (likely)

Figure 4. Structure of model 35OC-RO at different times. The left-hand panel shows maps of the logarithm of the magnetic field strength, contours of the angular velocity (white lines), and magnetic field lines (black). The colour in the central and right-hand panels represents the specific entropy, while white and yellow lines show contours of the angular velocity and of the density (the innermost iso-density contour corresponds to $\rho = 10^{14}$ g cm^{-3} and the rest of the contours are spaced by factors of 10 in decreasing order). The pink lines in all panels display the three neutrinospheres and are a proxy for the location of the PNS surface.

---

[3]Model 35OC-RO has been run longer than in Paper I, until BH formation.

Table 2. Properties of the models we have built in this paper. From left to right the columns display the maximum computed post-bounce time (t_{max}), the time of BH formation after core collapse (if no BH is expected, we use a $\times$ sign), the angularly averaged rotational speed of the PNS surface, Ω_{surf}, the rotational frequency of the PNS, $\bar{\Omega} = J_{PNS}/I_{PNS}$, the associated period, $\bar{P} = 2\pi/\bar{\Omega}$, the toroidal and poloidal magnetic fields at the surface of the PNS in units of 10^{14} G, $b_{surf,14}^{tor}$, and $b_{surf,14}^{pol}$, respectively, the dimensionless specific angular momentum of the PNS, a_{PNS} (equation 5), the rotational energy of the PNS in units of 10^{52} erg, $\mathcal{T}_{52}^{PNS}$, the ratios β_G (equation 3) and ϵ_B (equation 4) in units of 10^{-2}, the moment of inertia of the PNS in units of 10^{45} g cm^2 and the PNS mass. All quantities have been measured at $t_{pb} = t_{max}$. In case a model finishes with the formation of a BH, the listed values of a_{PNS} and M_{PNS} correspond to the initial values of these quantities for the just born BH.

Name	t_{max} (s)	t_{BH} (s)	Ω_{surf} (Hz)	$\bar{\Omega}$(Hz)	$\bar{P}$ (ms)	$b_{surf,14}^{tor}$	$b_{surf,14}^{pol}$	$\mathcal{T}_{52}^{PNS}$	J_{49}^{PNS}	a_{PNS}	$\beta_{G,-2}$	$\epsilon_{B,-2}$	I_{45}^{PNS}	$M_{PNS}/M_\odot$
35OC-RO	3.23	3.23	3003	7529	0.83	4.28	0.71	16.85	4.31	0.48	3.99	1.16	5.72	3.19
35OC-RO2	3.07	3.07	2828	6023	1.04	0.43	0.00	12.68	3.04	0.41	3.88	0.04	5.04	2.90
35OC-Rp2	7.57	$\times$	2087	2962	2.12	1.76	0.15	9.51	1.09	0.70	0.42	0.60	2.35	2.33
35OC-Rp3	8.96	$\times$	3712	5530	1.14	1.33	0.15	5.31	1.91	0.42	3.12	0.04	3.46	2.28
35OC-Rp4	1.95	$\times$	1539	2561	2.45	1.55	1.87	1.39	0.98	0.33	1.46	0.32	3.84	1.85
35OC-Rw	2.54	> 2.54	1212	3185	1.97	3.03	4.09	5.74	2.51	0.46	2.61	1.20	7.86	2.49
35OC-Rs	2.34	$\times$	−5	180	34.8	1.38	1.30	0.22	0.55	0.25	1.13	28.74	30.60	1.58
35OC-Sw	1.48	1.48	1384	2516	2.50	3.66	0.43	0.93	0.63	0.13	0.31	1.35	2.50	2.38
35OC-RRw	1.59	$\times$	2685	5051	1.24	0.92	0.05	11.78	4.46	0.72	7.43	0.03	8.83	2.64
35OB-RO	1.48	1.48	2891	5344	1.18	3.11	0.00	3.96	1.44	0.26	1.27	0.08	2.70	2.49
35OB-RRw	2.36	>2.36	691	1649	3.81	3.06	1.31	16.83	10.22	1.01	8.36	1.92	61.94	3.39

increase the BH spin to significantly larger values. Hence, a collapsar engine may eventually result from this model.

3.1.2 Model 35OC-RO2 with twice stronger magnetic field

Model 35OC-RO2 begins its time evolution with the same rotational profile as the progenitor star 35OC, but with poloidal and toroidal magnetic fields artificially increased by a factor of 2 with respect to the stellar progenitor (Table 1). This model forms a BH after $t_{BH} \simeq 3.07$ s. By that time, the PNS mass has grown well beyond M_{bry}^{max} (Fig. 2a and Table 2), and the mass accretion rate on the PNS does not show signatures of saturation or decrease, maintaining a level of $\gtrsim 0.3\,M_\odot\,s^{-1}$ during the whole evolution, and even increasing above $\gtrsim 0.5\,M_\odot\,s^{-1}$ after $t_{pb} \sim 2.5$ s (Fig. 2b).

The time-evolution of this model shares many similarities with model 35OC-RO, among them the fact that the explosion is magnetorotationally driven. However, the growth of the PNS mass after the accretion of the Sillicon core happens at a smaller rate than in the former model (Fig. 2a). Compared to model 35OC-Rp2, with the same poloidal initial field, the post-collapse dynamics of both models is significantly different (indeed, model 35OC-Rp2 does not form a BH during the computed evolution; see Section 3.2.1). Since the main difference between models 35OC-RO and 35OC-RO2 is the twice larger toroidal magnetic field in the latter, we may preliminary conclude that a moderate increase of the toroidal magnetic field in the progenitor star does not alter the prospects for BH formation.

A detailed look at the evolution of the structure of the core further emphasizes the parallelism to model 35OC-RO (see Fig. 5): we find an early development of magnetic channels ($t_{pb} = 215$ ms, left-hand panel) as well as a PNS that intermittently has a very large equatorial extent ($t_{pb} = 1.4$ s, middle panel) and later contracts to a much smaller size, while maintaining an oblate shape ($t_{pb} = 3$ s, right-hand panel).

3.1.3 Model 35OC-Sw: slower rotation and weak field

Model 35OC-Sw combines a relatively weak field consisting of a global dipole ($b_{max}^{pol} = 10^8$ G) and a toroidal component ($b_{max}^{tor} = 10^{10}$ G) with a comparably slow rotational profile obtained by globally reducing the angular velocity of the original stellar-evolution
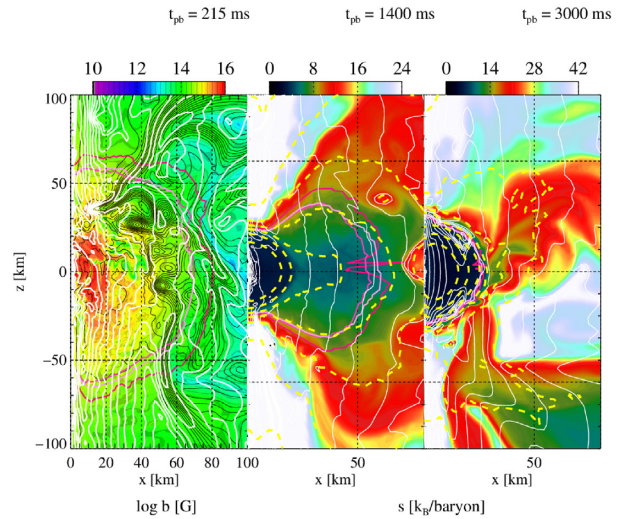

Figure 5. Same as in Fig. 4, but for model 35OC-RO2.

model by a factor of 4. Admittedly, this combination of slow rotation and weak magnetic field, departs significantly from the original properties of the 35OC stellar core. However, this model aims to *complete* a region of the parameter space uncovered with the rest of the models in this paper. While this reduction does not make rotation irrelevant ($\mathcal{T}^{PNS} \approx 9 \times 10^{51}$ erg at the end of the simulation; see Table 2), its influence is far less notable, and the explosion mechanism differs considerably from the models discussed above. Furthermore, the magnetic field remains mostly toroidal throughout the computed evolution, with only a very weak addition of a poloidal field (panels k and l of Fig. 2). The reduced magnetic and rotational energy of this model with respect to the original stellar progenitor values induce a standard neutrino-driven supernova explosion aided by hydrodynamic instabilities (mostly SASI), though with significantly North–South asymmetric and collimated ejecta (see Paper I). The dynamics within the gain region where the ejecta are accelerated are highly variable, much more so than in the other models, translating into fluctuating fluxes of mass and energy in each of the hemispheres and also fluctuating locations of the accretion streams feeding the PNS.

The ongoing presence of strong accretion streams causes the PNS to steadily grow in mass until it finally collapses to a BH at $t_{BH} \simeq 1.48$ s. At the time of BH formation, the compact remnant has a mass $M \simeq 2.4\,M_\odot$ (Table 2). This value is slightly smaller than M_{bry}^{max}, and results as a consequence of the approximated treatment of the general relativistic effects in our method. The minor influence of rotation prevents any of the effects that in other models (models 35OC-RO and 35OC-Rs) lead to a rather extended PNS envelope. Instead, the PNS is comparably compact with a radius at BH collapse of $R_{PNS} \approx 18$ km and only a small degree of asphericity (Fig. 6). The total angular momentum, strongly concentrated at the very centre, corresponds to a spin parameter $a_{PNS} \approx 0.13$. This is fairly small and we anticipate that it is probably insufficient to yield a GRB progenitor. In this model, the specific angular momentum of the star (see Fig. 1b) is insufficient to produce an accretion disc within the first $t_{pb} \sim 40$ s ($t_{DF} \approx 43$ s; Table 1). Hence, it is unlikely that model 35OC-Sw may produce a *standard* collapsar engine.

3.1.4 Model 35OB-RO

Model 35OB, based on a relatively high mass-loss rate, differs from model 35OC in the structure of the core. The former one possesses a fairly weak density and entropy jump located at a slightly higher mass coordinate than the surface of the iron core of model 35OC-RO. In contrast to core 35OC, the rotational profile is continuous there, leading to rapid rotation outside the density jump.

In model 35OB-RO, we also used the magnetic field from the pre-SN progenitor. This implies that the maximum poloidal and toroidal magnetic field strengths in the initial model are $b_{max}^r = 7 \times 10^{10}$ G and $b_{max}^\phi = 9 \times 10^{11}$ G, respectively. The high mass-loss due to stellar winds translates into a comparably low rotational energy. Hence, the influence of rotation on the evolution is subdominant, leading to small degrees of anisotropy of the PNS and of the neutrino emission; magnetic fields do not play any notable role.

The PNS accretes matter until it collapses to a BH at $t_{BH} \approx 1.48$ s (Table 2). With only a minor degree of rotational support, its final mass before BH collapse is $M_{PNS} \simeq 2.49\,M_\odot \gtrsim M_{bry}^{max}$. The angular momentum ceases to grow in the inner core at densities $\rho > 10^{14}$ g cm^{-3} at $t_{pb} \approx 0.8$ s. Afterwards, we observe a decrease of the total angular momentum of the PNS (Fig. 2f), leading to a spin parameter $a_{PNS} \approx 0.26$ at BH collapse (Table 2).

3.1.5 Models 35OB-RRw and 35OC-RRw with supra-stellar rotation

We allow for another relatively small variation of the progenitor stars 35OB and 35OC by considering a factor of 2 and 1.5 increase of its rotational speed in models 35OB-RRw and 35OC-RRw, respectively. In order to allow for such an increase in the rotational speed, we decrease drastically the magnetic field strength, somehow mimicking the effect reduced magnetic torques could operate in the stellar progenitor (Table 1). The reduction of the magnetic field strength also serves to prevent a prompt magnetorotational explosion (indeed, 35OB-RRw results in a failed SN explosion). Alternatively, one may explain the increase of the rotational frequency of the progenitor core as the result of, e.g. a reduction of the mass-loss rate during the stellar evolution (Woosley & Heger 2006, built model 35OA with an iron core period that is half the value of model 35OC by setting to zero the mass-loss rate), or the incorporation of the effects of wind anisotropies up to the He-burning stage, since in this case Meynet & Maeder (2007) predict faster-rotating cores than
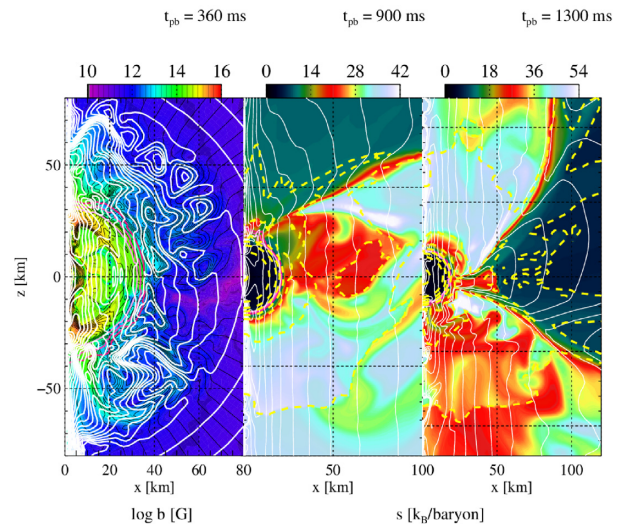

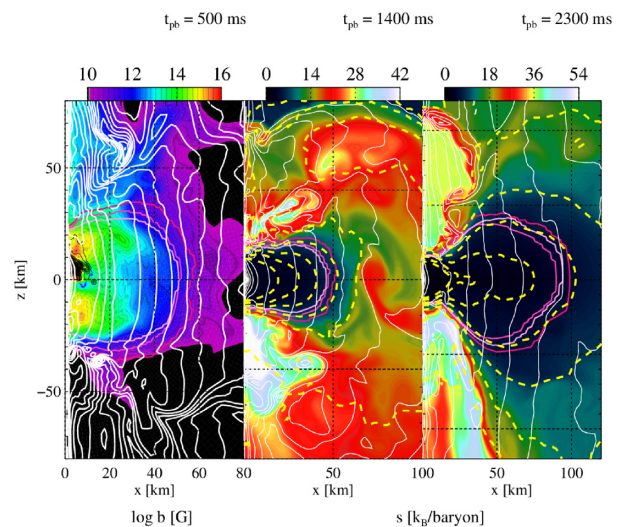**Figure 6.** Same as Fig. 4, but for model 35OC-Sw.

Figure 7. Same as in Fig. 4, but for model 35OB-RRw.

Woosley & Heger (2006). Interestingly, there is an active debate on whether the evolution after the He-burning phase may or may not significantly reduce the angular momentum of the core (see section 2 of Meynet & Maeder 2007, and references therein). Hence, the artificial modification that we have included in the rotational speed of the iron core, which may evolve somewhat *detached* from the outer stellar envelope is not totally inconceivable. This manipulation intends to probe the impact of rotation on the dynamics.

The consequence of the faster rotation and hence enhanced rotational support against gravity is that matter does not fall as deeply into the gravitational well of the core as when using the original rotational profile. This effect, most pronounced in the equatorial plane, leads to an oblate PNS with a particularly high axial ratio and to a reduction of the neutrino luminosity induced by the accretion on to the PNS, in comparison to model 35OB-RO. Rotation focuses the neutrino emission strongly along the symmetry axis, creating favourable explosion conditions there. Nevertheless, even taking into account the focusing effect, neutrino heating fails to meet the conditions for shock revival. The failure is in part owing to the high mass accretion rate (larger for model 35OB-RRw and for model

35OC-RRw throughout most of the evolution Fig. 2b) and in part to the redistribution of the energy deposited at the poles by lateral convective flows acting on time-scales below that of neutrino heating. As a result, no explosion takes place for more than ~ 2.3 s (1 s) in the case of model 35OB-RRw (35OC-RRw) and the model exhibits a steady increase of the PNS mass (Fig. 2a). The very high mass reached by model 35OB-RRw, $M(\rho \geq 10^{12}$ g cm$^{-3}) \approx 3\,M_\odot$, by the end of the simulation does not translate into an immediate collapse to a BH, since the core is supported by centrifugal forces. The development of its structure can be followed in Fig. 7. The PNS has a large axial ratio early on ($t_{pb} = 0.5$ s) that is maintained as it contracts ($t_{pb} = 1.4$ s). Later ($t_{pb} = 2.3$ s), the polar radius of the PNS is virtually unchanged, but the equatorial region is characterised by an extended dense torus-like configuration with an approximately cylindrical rotational profile (thin white lines) surrounding the PNS. In terms of the thermodynamical state, the torus is a continuous extension of the PNS, as we can see in the low entropies (colour scale). This structure corresponds to distributions in which the outer layers of the PNS/torus system carry a relatively large and even increasing amount of mass and angular momentum and to the largest spin parameters ($a_{PNS} \geq 0.72$).

Based on the late stages of the simulation, we expect that the ongoing accretion on to the PNS will eventually lead to the formation of a BH in both models. We cannot, however, provide the collapse time without running the simulations (much) longer. It is, nevertheless, clear that the moderate increase of the rotational rate of these two models has not changed the type of compact remnant expected within seconds after bounce.

3.1.6 Model 35OC-Rw with weak magnetic field

Model 35OC-Rw uses the same pre-collapse state as model 35OC-RO, but has a weaker magnetic field of dipolar geometry. The core evolves qualitatively similarly to model 35OC-RO, reflecting the magnetic field is amplified to levels similar to the latter at the expense of the rotational energy of the system (Figs 2c and i). Although a BH has not formed after $t_{pb} = 2.54$ s, by this time $M_{PNS} \simeq 2.5\,M_\odot \gtrsim M_{bry}^{max}$, and the core is loosing rotational support (see below), enhancing the prospects for BH collapse. However, this model enters into a phase of intermittent mass shedding, which makes it difficult to predict the final outcome. Hence, even if we have considered among the subset of our models which may produce a BH long after the PNS formation, model 35OC-Rw is a borderline case between collapsar and PM-forming cases. Model 35OC-Rw exhibits clear sloshing modes of the SASI with large and small shock radii oscillating between the north and south poles. Indeed, this model explodes by the combined action of neutrino heating, the SASI, and rotation (see Paper I), resulting in very asymmetric (north/south) ejecta.

The profile of density and angular momentum of the two models are equal, and thus the growth of the PNS is similar, though slightly slower in model 35OC-Rw after $t_{pb} \sim 1.3$ s (Fig. 2f). Compared to model 35OC-RO, there is virtually no redistribution of angular momentum from the centre to the PNS envelope throughout most the evolution ($0.5 \lesssim t_{pb} \lesssim 1.5$ s) as we can see in Fig. 8(c). The layers with $10^{12} < \rho < 10^{13}$ g cm^{-3} transiently possess a notable fraction of the total angular momentum of the PNS and quickly lose most of it towards the inner regions. As a consequence, they are supported against gravity to a lower degree by centrifugal sources and contract more than in model 35OC-RO. The resulting more compact structure of the PNS is evident in the distribution of mass across shells with the innermost layers (Fig. 8b; blue line) containing almost all of
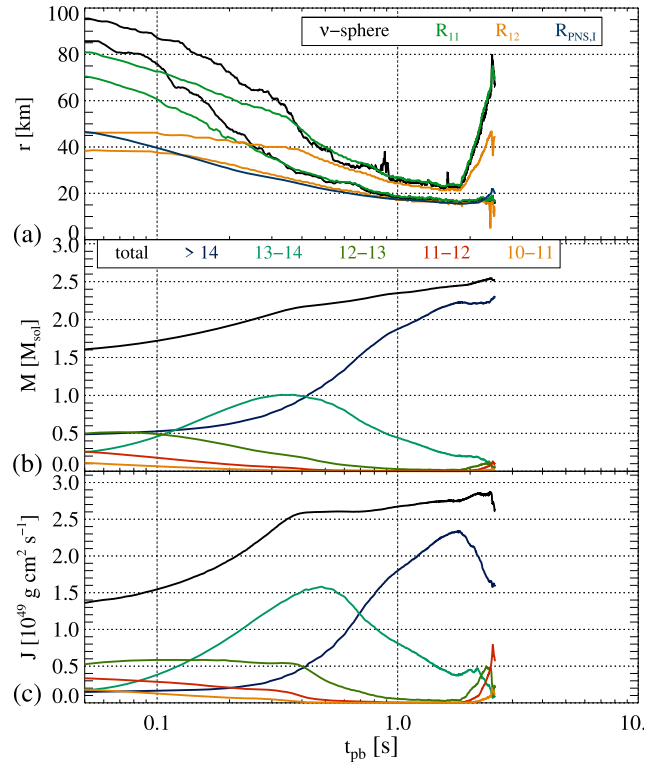

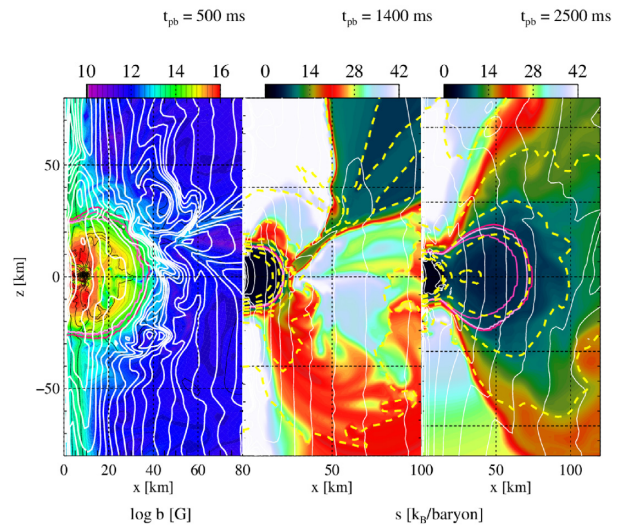**Figure 8.** Same as Fig. 3, but for model 35OC-Rw.

Figure 9. As to Fig. 4, but for model 35OC-Rw. The gain layer is roughly enclosed by the outermost iso-density surface (dashed yellow line) corresponding to $\rho = 10^9$g cm^{-3}.

the mass. Furthermore, the PNS has a less oblate shape than that of model 35OC-RO (Fig. 9). While the polar/minimum radii of both models are similar, the equatorial/maximum radii of model 35OC-Rw decrease faster, leading to an axial ratio approaching roughly 3:2 after $t_{pb} \sim 1.5$ s (Fig. 8a).

The tendency of the outer layers to lose angular momentum is, however, reversed at late times, $t_{pb} \gtrsim 1.5$ s (red, orange and olive green lines in the bottom panel of Fig. 8). The magnetic field is then strong enough to redistribute angular momentum from the interior

to the PNS surface. This effect leads to a factor of ~ 3 increase of the equatorial radius and a very oblate shape of the PNS. This transition, extending the PNS surface into regions of low Y_e allows for very neutron-rich matter to be ejected and, hence, sets favourable conditions for the generation of heavy elements (see Reichert et al. 2020). Furthermore, it may allow for the formation of an extended, toroidally shaped layer of nearly centrifugally supported matter that may accrete on to the PNS on relatively long time-scales (Fig. 9, right-hand panel).

3.2 NS-forming models

In the following subsections, we describe the most salient properties of the dynamical evolution of models which may not form a BH during a significantly long time after collapse. These models are potential hosts of PM central engines, and we may refer to them as protomagnetar candidates (PMCs). We take as criterion to include models in this section that the final computed mass is below the maximum mass allowed by the EoS (in the non-rotating and zero-temperature limit), $M_{\rm bry}^{\rm max} \simeq 2.45\,{\rm M_\odot}$. Certainly, the smaller the value of $M_{\rm PNS}$, the better the prospects to produce a *long-lived*, PM. We cannot dismiss the possibility that fall back accretion from the stellar material not fully unbound by the SN explosion may induce a subsequent BH collapse in a (much) longer term. Aiming to understand transient activity during the first tens of seconds post-bounce, it is relevant to understand whether the formed PNS may survive and what are its properties.

3.2.1 Models 35OC-Rp2, 35OC-Rp3 and 35OC-Rp4 with supra-stellar magnetic field

The series of models formed by 35OC-Rp2, 35OC-Rp3 and 35OC-Rp4 differ only in the strength of the poloidal magnetic field with respect to the original pre-SN model 35OC-RO. Considering these variations is suggested by the diversity of post-bounce evolutions that differences in the mapping of the poloidal magnetic field from the stellar evolution model to our computational grid yield (see Appendix A). In spite of the moderate increase of the poloidal magnetic field strength in these model series, the fate of their cores significantly departs from that of model 35OC-RO. They all form magnetized and significantly massive PNSs and not BHs, as can be seen from the evolution of $M_{\rm PNS}$ in Fig. 2(a), as well as the corresponding column of Table 2. In all the cases the PNS mass evolution is not monotonic and develops (one or two) local maxima. The first of such local extrema happens at $t_{\rm pb} \sim 0.5\,{\rm s}$ (Fig. 2a), approximately when the whole iron core has been accreted. Dessart et al. (2008) found a similar qualitative behaviour. The fact that the compact remnant does not increase further its mass (but indeed, tends to reduce it), has been interpreted as an indication that the PNS will not collapse further to a BH in a foreseeable time (Dessart et al. 2008; Obergaulinger & Aloy 2017).[4] However, in previous works the post-bounce evolution was computed up to $t_{\rm pb} \lesssim 2\,{\rm s}$. Here, we have gone

---

[4]Fall-back accretion from the reverse shock of magnetized SN ejecta may bring less mass to the PNS than in an SN explosion. In magnetized ejecta, forming a strong reverse shock is more difficult, as it has been shown, e.g. in the context of the dynamics of GRB ejecta (Zhang & Kobayashi 2005; Giannios, Mimica & Aloy 2008; Mimica, Giannios & Aloy 2009). Furthermore, inasmuch as the magnetic structure of the PNS and surrounding is maintained, most of the mass falling at low latitudes will be shuffled towards the polar regions and contributing to the channelled outflow, not to the growth of the PNS mass.

(much) further, computing until almost $t_{\rm pb} \sim 10\,{\rm s}$ in some models. As a result, we observe that after the first local maximum, the mass may grow and reach a second global maximum as, e.g. in the case of model 35OC-Rp2 at $t_{\rm pb} \simeq 5.4\,{\rm s}$. Model 35OC-Rp3 displays a second phase of mass increase starting at $\sim 2\,{\rm s}$ and continuing until the end of the computed time (Fig. 2a). Model 35OC-Rp4 has not been evolved for so long as model 35OC-Rp3, but one can guess that a similar, long-lasting PNS mass evolution may happen. We note that the mass accretion rate becomes negative (i.e. mass is extracted from the PNS) episodically in these models, and when it is positive, $\dot{M}_{\rm PNS} \lesssim 0.2\,{\rm M_\odot}\,{\rm s}^{-1}$ (Fig. 2b). Since in all these models $M_{\rm PNS} < M_{\rm bry}^{\rm max}$ (at the end of the computed time) and a further collapse to a BH does not seem imminent, we find it justified to refer to these models as PMCs.

The root of the different fate of PMCs and other BH-forming cases, singularly with respect to the potential collapsar forming model 35OC-RO, is the (slightly) larger poloidal magnetic field of the former models. This larger poloidal field drastically changes the post-bounce accretion dynamics, significantly reducing the mass accretion rate on to the PNS. Tightly linked to the reduced mass gain of the PNS is the smaller rotational energy and angular momentum attained in the long-term evolution of PMCs. In Fig. 2(c), we observe that PMCs may develop $\mathcal{T}^{\rm PNS} \lesssim 5 \times 10^{52}\,{\rm erg}$, whereas values $\mathcal{T}^{\rm PNS} > 6 \times 10^{52}\,{\rm erg}$ are reached by BH-forming models developing either from the original 35OC core or variants thereof with enhanced stellar rotational speed or reduced magnetic fields. Associated to the smaller PNS rotational energy are the smaller values of the rotational to gravitational binding potential energy of PMCs, for which $\beta_{\rm G} \lesssim 0.03$ (Fig. 2d). Considering its larger magnetization and the reduced value of $\beta_{\rm G}$, PMCs may potentially be less perturbed by the 'low-$\beta_{\rm G}$' instability (see section 3.1.1.2). PMCs also posses a PNS angular momentum significantly smaller ($J_{\rm PNS} \lesssim 2 \times 10^{49}\,{\rm g\,cm^2\,s^{-1}}$) than BH-forming models (Fig. 2f).

Another consequence of the increased poloidal field in PMCs is that the shape of the PNS is less oblate than that of typical BH-forming cases. The PNS of PMCs posses both larger equatorial and polar radii initially ($t_{\rm pb} \lesssim 1.5\,{\rm s}$), which tend to become similar (i.e. the shape becomes less oblate) on longer time-scales (compare Figs 10 and 11 with 3). The angular momentum in the PNS of PMCs concentrates in the denser parts of the remnant ($\rho > 10^{14}\,{\rm g\,cm^{-3}}$) more effectively after $t_{\rm pb} \gtrsim 1.1\,{\rm s}$ (see lower panels of Figs 10–11). Once the inner core angular momentum dominates the overall PNS angular momentum the fraction of the latter retained by layers with $10^{11} < \rho < 10^{14}\,{\rm g\,cm^{-3}}$ is smaller in PMCs than in BH-forming models. However, we note that PMCs concentrate a larger fraction of the PNS mass in the inner core ($\rho > 10^{14}\,{\rm g\,cm^{-3}}$) than PCs (compare Figs 3b with 10b). Interestingly, the radius $R_{\rm PNS,I}$ is $\sim 20-40$ per cent smaller than the polar radius of the PNS tracked with any other criteria (density isosurfaces or neutrinospheric radius; compare, e.g. Fig. 3a with Fig. 10a), implying that the moment of inertia is more concentrated in PMCs than in PCs.

Model 35OC-Rp3 displays a fairly abrupt transition from a very oblate shape (Fig. 12b, $t_{\rm pb} \approx 1.45\,{\rm s}$) to a more spherical one at $t_{\rm pb} \approx 2\,{\rm s}$, and remains so for a long time (see the panel corresponding to $t_{\rm pb} \approx 3\,{\rm s}$). Slightly less than $0.1\,{\rm M_\odot}$ of rapidly rotating matter is released from the PNS surface and the axial ratio drops from about 3:1 to almost unity (Figs 11a and b) and then remains at a similar value for the following 7 s of evolution. The transition of the shape and structure is accompanied by a decrease of the angular momentum in the outer layers and $\Omega_{\rm surf}$. The loss of mass and rotational energy of the PNS partially contributes to the outflow and enhances its energy
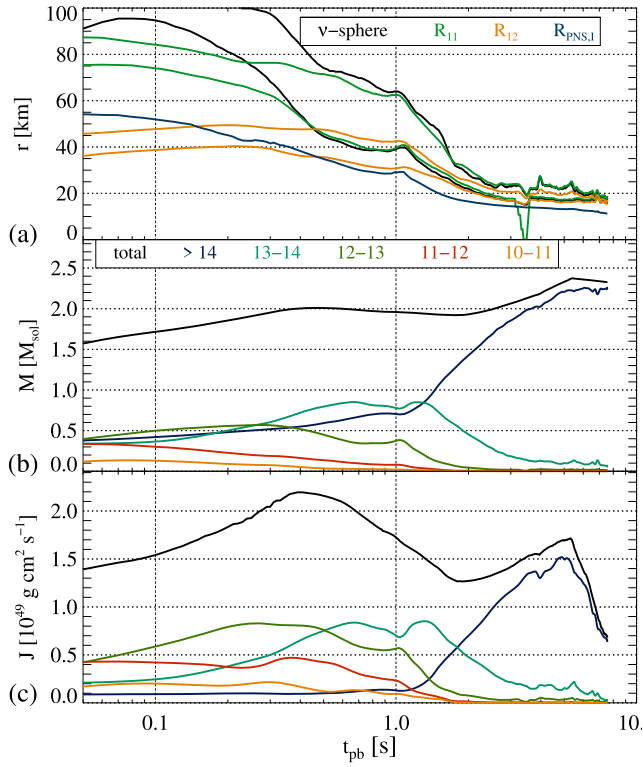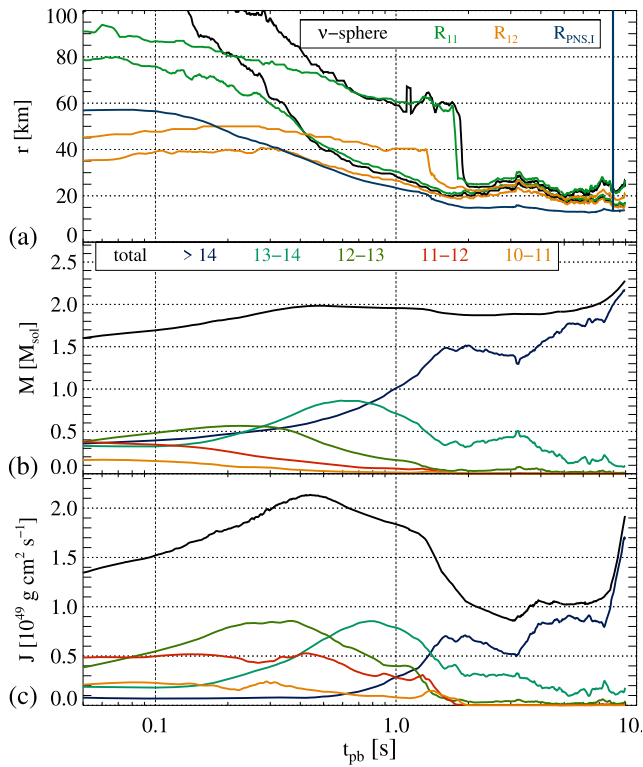
Figure 10. Same as Fig. 3, but for model 35OC-Rp2.

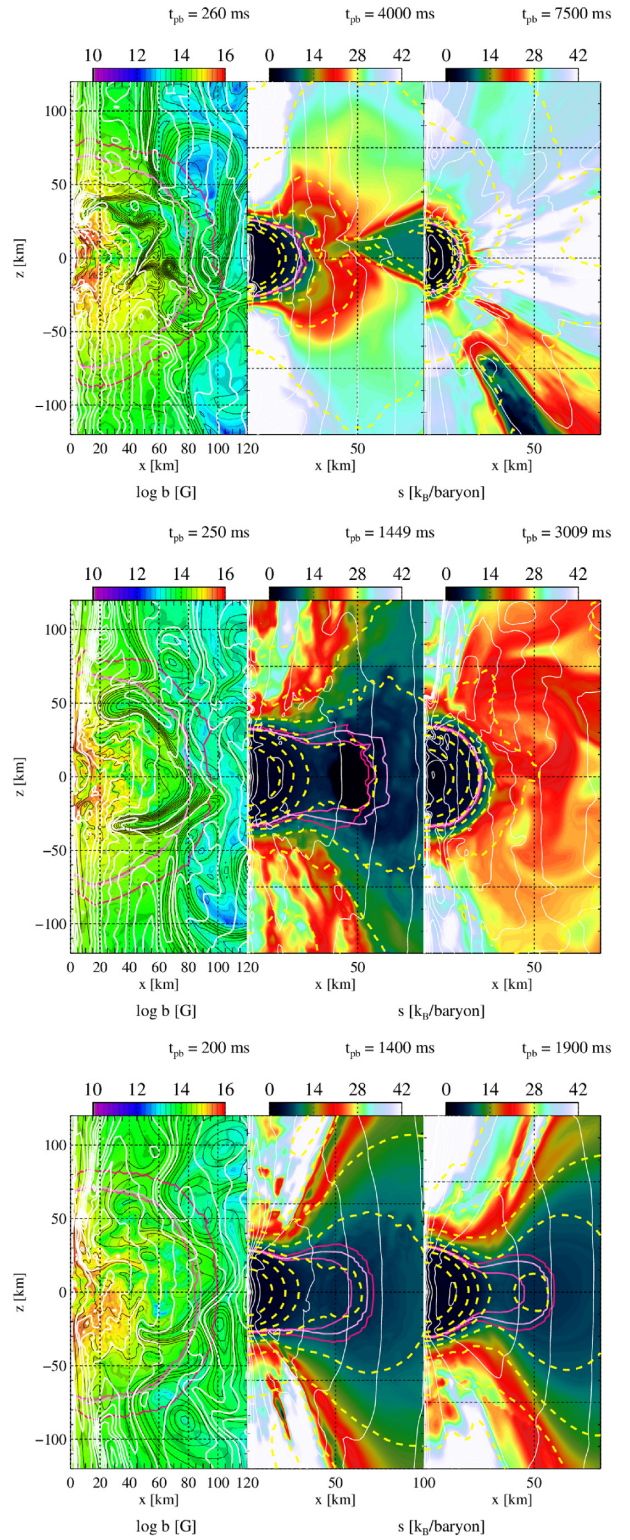

Figure 11. Same as Fig. 3, but for model 35OC-Rp3.

Figure 12. Same as Fig. 4, but for models 35OC-Rp2 (top panel), 35OC-Rp3 (mid panel), and 35OC-Rp4 (bottom panel).

flux with respect to, e.g. model 350C-RO which does not show the same intermediate, transitory spin-down. Apart from this effect, the stronger magnetic fields lead to higher explosion energies and larger explosion masses (see Paper I and Table 1) compared to the original field taken from the stellar evolution progenitor by virtue of a greater Maxwell stress accelerating the gas.

3.2.2 Model 350C-Rs with strong magnetic field

Model 350C-Rs contains a magnetic field consisting of a dipole and a toroidal component in equipartition and with maximum values $b^\phi = b^r = 10^{12} \, G$. Compared to the maximum magnetic fields of model 350C-RO, $b_{max}^r = 5 \times 10^{10}$ G and $b_{max}^\phi = 10^{12}$ G, the toroidal magnetic field is roughly the same in both models, but the poloidal one is 50 times larger in model 350C-Rs. This means that whereas it represents an energetically almost negligible component in model 350C-RO, the poloidal field constitutes about half of the total magnetic energy in model 350C-Rs (Table 1). We may justify the increase of the magnetic field strength with respect to the stellar progenitor resorting to the limited ability of numerical models to resolve the magnitude of MRI-amplified magnetic fields. If the fastest growing MRI modes were resolved, a rough equipartition between the toroidal and poloidal magnetic field components may develop after core collapse (e.g. Obergaulinger et al. 2006b, 2009; Dessart et al. 2008). Under the conservative assumption that our numerical resolution may limit the poloidal magnetic field amplification (but see Section 3.3, and note the growth by several orders of magnitude of the surface-averaged poloidal magnetic field in Fig. 2k), we adopt larger values of the initial magnetic field component in this model.

The initial magnetic energy of model 350C-Rs is basically the same as that of model 350C-Rp4 (Table 1), from which it mostly differs in the magnetic topology. The poloidal component of the magnetic field in model 350C-Rs is smoother on larger length scales than in model 350C-Rp4 (see Appendix A). Indeed, there exists a significant difference between the magnetic topology of model 350C-Rs and other models inheriting directly the magnetic structure of the 350C core. In model 350C-RO there are unmagnetized layers, corresponding to convective regions of the progenitor star, where there are no recipes to incorporate the action of magnetic torques in the stellar evolution. Contrarily, magnetic field lines thread the whole stellar progenitor in model 350C-Rs, some of which connect the stellar core with the stellar surface and, hence, have a larger potential impact on the post-bounce dynamics (Bugli et al. 2020). The large-scale dipolar field explains why this model produces an almost immediate magnetorotational explosion characterized by a pair of polar, well collimated outflows, where neutrinos do not play a significant role (see Paper I).

The post-shock gas is almost at rest and therefore the growth of the PNS ceases at a maximum mass of $M_{PNS} \approx 1.9 \, M_\odot$ (a bit smaller than the iron core mass) after a time of $t_{pb} \approx 450$ ms. Afterwards, the mass of the PNS starts to decrease slowly as parts of its matter end up in the polar jets. This behaviour reproduces what we have found for models 350C-Rp2, 350C-Rp3, and 350C-Rp4, but the PNS mass reaches a smaller maximum and the reduction in the subsequent evolution is stronger (see below). Given the differences in the magnetic field topology and between model 350C-Rs (equipped with a large-scale magnetic dipole) and the former models, we directly attribute the significant change in the PNS mass evolution to the enhancement of the poloidal magnetic field in the iron core of PMCs compared to BH-forming models.
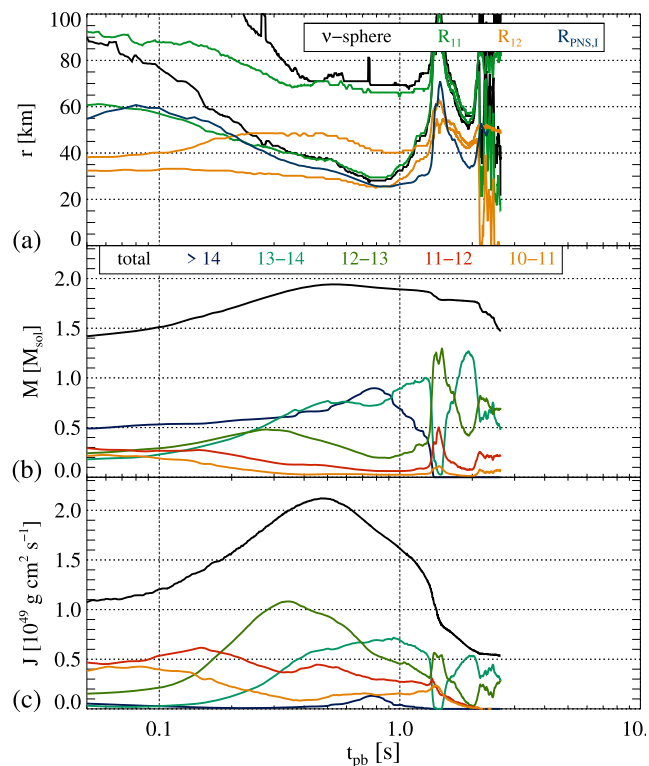

Figure 13. Same as Fig. 3, but for model 350C-Rs.

Thus, model 350C-Rs also shows optimal properties to produce a PM in the mid-term (namely, after a few seconds, once the PNS contraction approximately ceases).

The PNS geometry transitions from toroidal initially to very oblate around the time by which the maximum PNS mass is reached, since, as in model 350C-RO, the equatorial surface ceases to contract at quite large radii (Fig. 13a). In that respect, both models evolve very similarly during the early phases of the evolution ($t_{pb} \lesssim 1$ s), though model 350C-Rs has a slightly larger radius at the equator. The surface-averaged angular velocity is similar as well until $t_{pb} \simeq 0.9$ s, but later on, the PNS of model 350C-Rs undergoes a rapid magnetic braking, which effectively stops the rotation of the surface layers (Figs 2j and 13c). This behaviour comes as a consequence of a structural change that happens at $t_{pb} \gtrsim 2.1$ s in the PNS, whose shape changes from an oblate ellipsoid (with maximum density at $r = 0$) to a toroidal structure (with maximum density off centre; see the dashed yellow iso-density contours in Fig. 14 at $t_{pb} = 2.6$ s). In this morphological transition matter close to the rotational axis (whose density decreases significantly to values $< 10^{13}$ gr cm^{-3}) is pulled away by the magnetic field, which dominates (by far) the total pressure in this region. As a result, mass is ejected from the axial regions at rates that, intermittently, can be $\gtrsim 1 \, M_\odot$ s^{-1} (Fig. 2b). The action of this sort of *interchange* instability, where the pressure support is provided by the magnetic fields to a larger degree than by the baryons, produces a flux tube along the rotational axis where matter counter-rotates. Part of this counter-rotating matter enters the polar outflows, and the rest falls towards lower latitudes, slipping around the PNS surface. Since in our procedure to compute surface-averaged values, we shall consider regions with a finite radial extension around the neutrinospheres, positive and negative values of Ω add up and yield as a net result that $\Omega_{surf} \rightarrow 0$ (and even $\Omega_{surf} < 0$; Table 2). In coincidence with the morphological transition, the neutrino luminosity raises and displays
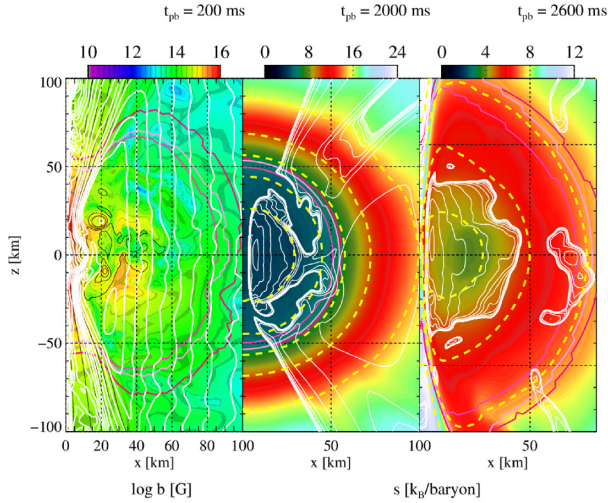
Figure 14. Same as Fig. 4, but for model 35OC-Rs.

a local maximum, where it reaches a value $\lesssim 40$ per cent of the peak luminosity in the post-bounce neutrino burst. The morphology shift leaves, therefore, a signal in the neutrino luminosity (dominated by the combined contributions of μ and τ neutrinos and antineutrinos) and, presumably, in the gravitational wave emission.

3.3 Magnetic field amplification

The magnetic field in the PNS is amplified by the advection of magnetic flux from the surrounding regions on to its surface, by compression as the PNS contracts, and by differential rotation. Compression yields a growth of the magnetic energy as a result of magnetic flux conservation, but it also produces a comparatively larger growth of the rotational energy resulting from the angular momentum conservation, hence, reducing the ratio ϵ_B. The growth of rotational energy resulting from compression may also induce the growth of the magnetic energy, but in any case, the magnetic energy growth is limited to a fraction of equipartition with the available kinetic energy in the system. The PNS dynamics in all our models yields a (non-monotonic) growth of ϵ_B, whose maximum values are $\epsilon_B < 1$ in the case of model 35OC-Rs (Fig. 2e). In order to quantify more precisely the origin of the magnetic field growth, we compute the available free energy of differential rotation as the difference in rotational energy of the PNS and the rotational energy of a uniformly spinning PNS of the same angular momentum, J, and moment of inertia, I,

$$\mathcal{F} := \mathcal{T} - \frac{J^2}{2I}, \tag{6}$$

and we further define the fraction

$$\epsilon_{BF} := \mathcal{B}^{PNS}/\mathcal{F}^{PNS}, \tag{7}$$

in analogy to ϵ_B (equation 4). The definition of $\mathcal{F}$ is adapted from Dessart et al. (2012) (cf. their equation 4), which is inspired, in its turn, by the fact that solid-body rotation corresponds to the lowest energy state for fixed total angular momentum, and this is the state any rotating fluid will reach on a *secular* time-scale, if it may redistribute its angular momentum. In our models, the inner parts of the PNS (with $\rho \gtrsim 10^{14}$ gr cm^{-3}) are rotating nearly rigidly (though, differently from Dessart et al. (2012), the innermost $\sim 5-10$ km may develop a positive Ω-gradient), while the outer parts, with about one-fifth of

the PNS mass, concentrate the differentially rotating shells and thus, most of the free available rotational energy.

We have already pointed out (Section 3.2.1) that PMCs typically show smaller values of $\mathcal{T}^{PNS}$ than PCs. This is also the case for $\mathcal{F}^{PNS}$ in models which begin from the same rotational profile (Fig. 15b; solid lines). The difference in $\mathcal{F}^{PNS}$ grows with time among PMCs and PCs, and at, e.g. $t_{pb} \simeq 2$ s, PMCs display values of $\mathcal{F}^{PNS}$ about 2–8 times smaller than the corresponding to PCs. It is important noticing that the free available rotational energy is significantly smaller than the rotational energy (observe that the ratio $\mathcal{T}^{PNS}/\mathcal{F}^{PNS} \sim 20$ for $t_{pb} \gtrsim 4$ s in Fig. 15b), which limits the prospects for magnetic field amplification to values $b_{surf}^{pol} \approx 10^{15}$ G ($b_{surf}^{pol} \lesssim 10^{14}$ G) in the case of model 35OC-Rp2 (model 35OC-Rp3); see Fig. 2(k).

We observe (Fig. 15a) that the PMCs possess ratios of magnetic to rotational energies well in excess of the estimates of M11 (in the following), who assume that the previous fraction is $\sim 10^{-3}$ (cf. their equation 4). In our PMCs, the magnetic field typically accounts for a fraction $\epsilon_{BF} > 0.01$ of the free rotational energy during the computed time evolution. The previous fraction reduces to $0.001 < \epsilon_B \lesssim 0.01$ if we compare the magnetic and rotational energies of the PNS. We note that also PCs, though weaker magnetized in relative terms, also exceed the aforementioned estimate. The fact that ϵ_{BF} reaches values ~ 1 for models 35OC-Rp2 and 35OC-Rp3 suggests that the magnetic field growth happens at the expense of the free rotational energy and not at the expense of the (significantly larger) rotational energy of the PNS (in agreement with, e.g. Duncan & Thompson 1992). As can be seen in Fig. 15(a) (solid lines), ϵ_{BF} is significantly larger than 1 in the interval 5.2 s $\lesssim t_{pb} \lesssim 7$ s for model 35OC-Rp2, which seems to contradict that $\mathcal{B}$ feeds off $\mathcal{F}$. However, this is a consequence of various factors. First, the definition equation (6) is not perfect in an accreting PNS whose surface is only approximately defined by the location of the ν_e-sphere. As illustrated by Fig. 2(a), after $t_{pb} \simeq 5.2$ s the PNS mass of model 35OC-Rp2 decreases slightly. This is due to the fact that the large specific angular momentum of the stellar layers being accreted makes them only loosely bound to the PNS. Hence, a fraction of them can be unbound and incorporated to the explosion ejecta, explaining the reduction of the PNS mass and rotational energy. Secondly, the slow down of the PNS is not uniform, it is more important in the outer layers, which decreases the degree of differential rotation and, thereby, explains the increase of ϵ_{BF} also after $t_{pb} \sim 2.5$ s (Fig. 15b).

In the stellar model 35OC there is a gap of $\sim 3 M_{\odot}$ between the inner magnetized core and the ensuing stellar shell containing magnetized matter (Fig. 1). Qualitatively, the same comment applies to models resulting from the stellar core 35OB. Hence, in the simulations that include either the original magnetic field of the progenitor star or small variations there off, the layers accreted by the PNS after $t_{pb} \sim 2-3$ s evolution are not magnetized. As a result, the magnetic field amplification observed in models like 35OC-Rp2 and 35OC-Rp3 ~ 2 s after bounce does not result from the (practically unmagnetized) accretion flow on to the PNS. Instead, the magnetic field amplification results from local amplification processes (e.g. compression and MRI). The amplification of the magnetic field in model 35OC-Rs, especially regarding the surface-averaged poloidal component, is less intense than in other PMCs and also than in model 35OC-RO (Figs 2k and l). Indeed, model 35OC-Rs shows a poloidal field similarly strong (several 10^{14} G) as the toroidal one (Table 2), due to the fact that its initial values are large, reducing the prospects for further amplification in the post-bounce phase.

Considering first the case of model 35OC-RO, we find typical convective speeds in the PNS around $v_{conv} \leq 10^8$ cm s^{-1}, and the
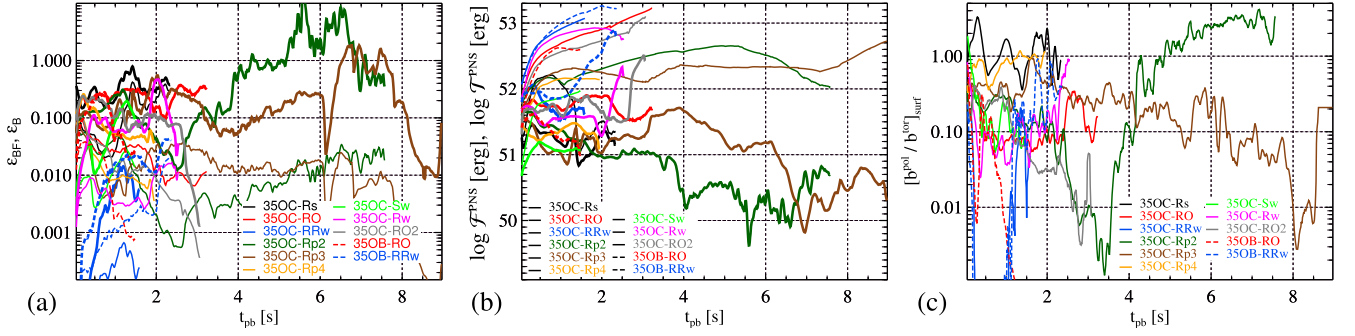
Figure 15. Time evolution of variables characterizing the magnetic field, rotational velocity, and structure of the PNS of the models indicated in the legends. The panels display: (a) the ratios of magnetic to rotational energy (ϵ_B; thin solid lines) and magnetic to free energy in differential rotation (ϵ_{BF}; thick solid lines) contained in the PNS; (b) the available free energy of differential rotation ($\mathcal{F}^{PNS}$; thick solid lines) and the rotational energy ($\mathcal{T}^{PNS}$; thin solid lines) of the PNS; (c) the ratio of poloidal to toroidal field on its surface.

pattern of convection is considerably modified by rotation. We observe convective cells aligned parallel to the rotational axis with a small extent in ϖ-direction. Differently from non-rotating magnetized collapsing cores (e.g. Obergaulinger et al. 2014), convection is not the main agent driving magnetic field growth. Instead, the PNS is unstable against the MRI, which is the main catalyst for magnetic field amplification. Since the initial poloidal field is sufficiently strong, we are able to numerically resolve the growth of the MRI in the form of channel modes (Fig. 4, left-hand panel; see also Rembiasz et al. 2016a, 2017), which develop between $t_{pb} \approx 150$ ms and $t_{pb} \approx 240$ ms at cylindrical radii around $\varpi \approx 50$ km and lead to an exponential growth of the energy of the poloidal field component (Fig. 2k).

The MRI activity is transient only. After the end of the exponential growth, the channels gradually fade away into fields dominated by small-scale structures. The energy of the poloidal field decays over half a second, though the differential rotation is maintained throughout the evolution and the angular velocity even increases due to the accretion of rapidly rotating matter (Fig. 2j). Large regions of the interior inside the neutrinospheres show a cylindrical rotational profile (see the white contours in the left-hand panel of Fig. 4). Assuming that the rotational frequency can be locally parametrized by a power law of the form $\Omega(r) \propto r^q$, a measurement of the rotational profile is the power-law index, q, precisely defined as

$$q(r) = d \ln \Omega(r)/d \ln r. \qquad (8)$$

We show in Fig. 2(h) the time evolution of q_{PNS} computed in the outer layers of the PNS, precisely,

$$q_{PNS} := \frac{3}{R_\nu} \int_{2R_\nu/3}^{R_\nu} dr \, q(r), \qquad (9)$$

i.e. q_{PNS} is a radial average value over the outermost one-third of the PNS radius on the equatorial plane. Since the inner part of the PNS is rigidly rotating, the MRI will not develop there. However, the outer (differentially rotating) layer of the PNS is much better suited for the magnetic field growth due to the MRI (e.g. Guilet, Müller & Janka 2015; Rembiasz et al. 2016a). Differentially rotating profiles with $-2 < q_{PNS} < 0$ permit the development of the MRI. Model 35OC-RO displays values $-2.5 < q_{PNS} < -1.6$ during most of its evolution, with typical values $q_{PNS} \simeq -2$, which precisely may render the fastest growth rates for MRI, $\gamma_{MRI} \simeq \Omega$ (in general, the growth rate of the fastest growing MRI mode is $\gamma_{MRI} \simeq |q_{PNS}|\Omega/2$; Pessah & Chan 2008). Anyway, in model 35OC-RO it is clear that the action of the magnetic fields is insufficient to significantly

flatten the rotational profile of the outer regions of the PNS, since q_{PNS} is significantly smaller than zero (indeed, $q_{PNS} < q_K = -1.5$, corresponding to a Keplerian profile). Besides, accretion keeps adding angular momentum at high rates to the outer PNS layers, acting against the development of a rigid rotational profile.

In other BH-forming models, we also observe episodes of exponential magnetic growth driven by the MRI. For instance, one of them starts at $t_{pb} \approx 100...200$ ms in model 35OC-RO2 (Fig. 2k) and, somewhat later ($t_{pb} \approx 400$ ms) and showing a longer lasting episode of growth for model 35OC-Rw. Both variants of the 35OC stellar core share the same initial rotational profile, which should make both models equally susceptible to the MRI. The fact that we do not observe it growing at the same magnitude can be attributed to the weaker initial field of model 35OC-Rw, which may shift the typical MRI modes to wavelengths below the grid resolution. We do not find indications of the MRI in the relatively weakly magnetized models of progenitor 35OB, and neither in the model 35OC-Rw. In model 35OB-RO, which develops fairly strong total magnetic fields, the MRI is numerically damped due to the weak poloidal field, which is far less intense than that of model 35OC-RO. The same holds for model 35OC-Rw. In this case, however, we find a late phase of amplification of the poloidal component sustained for half a second after $t_{pb} \approx 1.8$ s. The amplification occurs in the equatorial region near the PNS surface where a convective layer develops, at the top of which the field grows most rapidly.

The magnetic field growth in supra-stellar rotation models 35OC-RRw and 35OB-RRw represents an amazing example of exponential amplification without the concourse of MRI (though favoured by the imposed axial symmetry). It is due to the development of axisymmetric convective cells around the rotational axis, where the field is essentially vertical and initially very weak. Spruit (2013) shows that in planar symmetry a passive magnetic field can be exponentially amplified under the action of a converging-diverging, incompressible flow. This concept can be extended to axial symmetry. Near the axis and close to the PNS surface of models 35OC-RRw and 35OB-RRw, vertically stacked convective zones have an equivalent configuration to that of Spruit (2013). There, the magnetic and velocity fields can be roughly approximated by $\boldsymbol{b} \approx b_z(t)\hat{z}$, $\boldsymbol{v} \approx -a\varpi/2\hat{\varpi} + v_\phi(t)\hat{\phi} + az\hat{z}$, where $\hat{\varpi}, \hat{\phi}$, and $\hat{z}$ are the unit vectors in the cylindrical coordinate directions ϖ, ϕ, and z, while a is a constant. Under this configuration, one expects that the (initially passive) vertical magnetic field is exponentially amplified (for the approximate conditions stated above as $\boldsymbol{b}(t) \approx b_z(0)e^{at}\hat{z}$) until the vertical magnetic field becomes dynamically relevant and there is a back reaction on the fluid flow. The amplification shows signs

of saturation in model 35OC-RRw after $t_{pb} \approx 1$ s , but seems still ongoing for model 35OB-RRw after $t_{pb} \approx 2.4$ s (Fig. 2i).

PMCs with a supra-stellar magnetic field (models 35OC-Rp2, 35OC-Rp3, and 35OC-Rp4; Section 3.2.1) also develop a rotational gradient that could (potentially) allow for the growth of MRI (but see below). Nevertheless, the values of q_{PNS} are larger (smaller in absolute value) than in PCs (see next section), which allows for different evolutions. While the poloidal magnetic field in model 35OC-Rp2 initiates a sustained growth after $t_{pb} \sim 3.5$ s, which levels off after ~ 6 s at values $b_{surf}^{pol} \approx 10^{15}$ G (Fig. 2k), in model 35OC-Rp3 it raises very early to values $b_{surf}^{pol} \lesssim 10^{14}$ G, and maintains this level until $t_{pb} \sim 7$ s, after which it sinks steeply. In parallel to the magnetic field decline, the mass accretion rate grows, highlighting the correlation between the poloidal magnetic field strength and the ability to maintain the PNS mass below M_{bry}^{max}. We find during the ~ 2 s starting at $t_{pb} \sim 3.5$ s that the PNS of model 35OC-Rp2 develops vigorous convection, with convective overturn times $\tau_{conv} \sim 0.02$ s. The convective cells are forced into vertical cylinders by the rapid rotation. They end abruptly at the PNS surface, where the magnetic field accumulates first at the top, and then expands towards the centre. Since the up- and down-flows within the PNS are aligned with the rotational profile (instead of being perpendicular to it), we attribute the large amplification of the poloidal field in the PNS of model 35OC-Rp2 to the convection rather than to the MRI. An efficient dynamo may result if the Rossby number R_O, defined as the ratio of the convective overturn time to the rotational period, P, is of order unity or less (Duncan & Thompson 1992). The PNS is differentially rotating and, therefore, the rotational period depends (non-monotonically) on the distance to the rotational axis. In the case of model 35OC-Rp2, P ranges from ≈ 40 ms (close to the rotational axis) to ≈ 1 ms (at about 10 km off centre). This yields a broad range of Rossby numbers inside the PNS, $R_O \in [0.05, 2]$, such that $R_O \lesssim 1$ between $r \sim 5$ km and the PNS surface. The large amplification factor (~ 1000; even larger than the predictions of Duncan & Thompson 1992), by which the poloidal field grows from $\sim 10^{12}$ to $\sim 10^{15}$ G, contrasts with the very moderate growth that convection produces in the hot bubble surrounding the PNS in non-rotating, magnetized models (Obergaulinger et al. 2014). An approximate equipartition between b_{surf}^{pol} and b_{surf}^{tor} in model 35OC-Rp2 is reached after $t_{pb} \sim 4.2$ s (Fig. 15c). The late fall-down of the poloidal magnetic field of model 35OC-Rp3 is triggered by the accretion of unmagnetized stellar matter (see the positive and increasing mass accretion rate of this model after ~ 5 s in Fig. 2b), which partly buries the magnetic field of the PNS surface. It is accompanied by the (one order of magnitude) decrease of the toroidal magnetic field component at $t_{pb} \sim 7.5$ s (Fig. 2l). The different dynamics of the accretion flow on to the PNS of the previous models is connected to the feedback between the SN ejecta and the stellar progenitor layers. In model 35OC-Rp4 we do not observe the action of MRI, except, perhaps very early after its core collapses. As we have commented for model 35OC-Rs, the initial (relatively large) strength of the poloidal magnetic field of model 35OC-Rp4 may hamper the development of the MRI due to the dynamical back-reaction of the magnetic field on to the background flow.

3.4 Angular momentum redistribution and stability of the hypermassive PNS

We first discuss the redistribution of angular momentum in model 35OC-RO. In parallel with the mass growth, the angular momentum of the PNS increases due to accretion. The angular momentum is

fairly evenly distributed among the different shells of the PNS (see bottom panel of Fig. 3). The angular momentum of the innermost layers of the PNS rises alongside their increase in mass. The outer three shells between $\rho = 10^{10}$ and 10^{12} g cm^{-3} possess rather high specific angular momentum around $j \gtrsim 1.5 \times 10^{16}$ cm^2 s^{-1}. This distribution is caused by magnetic stresses removing angular momentum from the interior of the PNS to its envelope, thereby countering the inward transport by purely hydrodynamic flows. The resulting rotational support of the envelope of the PNS limits the degree to which its concentration towards the centre can go on and contributes to maintain the PNS stability against BH collapse once $M_{PNS} > M_{bry}^{max}$. This effect explains why lower density shells retain a comparably low, but non-negligible fraction of the mass. It also accounts for the strongly prolate shape of the PNS and the large equatorial radii, with a pole-to-equator axial ratio of about 10:18 by the end of the simulation.

We found that magnetic redistribution of angular momentum from the centre tends to increase the radius of the core. At first, it might be natural to expect the exact opposite outcome, viz. a contraction triggered by the loss of rotational support at the centre, analogously to the case of an accretion disc where outward angular-momentum transport enables accretion. To understand our result, we have to take into account that the angular momentum that is removed from the inner regions of the core does not immediately leave the PNS. Its efficient transport is limited by two effects: firstly, transport is restricted to a region where the magnetic fields are sufficiently strong, and, secondly, it has to act against the infall of matter from the post-shock region. As a consequence of these effects, angular momentum removed from the centre does not go beyond the outer layers of the PNS, where it increases the centrifugal support and hence causes an expansion. The effect that we have discussed for model 35OC-RO applies to nearly all the models in this paper. As a general trend, we observe that a stronger field reduces the total rotational energy (Fig. 2c), as could be expected. It does, however, deform the PNS to a more, rather than less, oblate geometry, a shape typical for higher, rather than lower, rotational energy.

We may compare the enhancement of the angular momentum of the shells at $\rho < 10^{13}$ g cm^{-3}, first, in models with different initial toroidal fields (models 35OC-Rw, 35OC-RO, 35OC-RO2). We find that the increase of J, especially in the layer 10^{12} g cm^{-3} < $\rho < 10^{13}$ g cm^{-3}, is more pronounced for models with initially smaller toroidal field, being model 35OC-Rw the one with the largest increase (Fig. 8c) and model 35OC-RO2 the one with the smaller increase (below the values reached by model 35OC-RO; Fig. 3).

We now turn to the effects of poloidal fields of increased strengths on the angular momentum redistribution inside the PNS. The angular momentum redistribution in models 35OC-Rp2, and 35OC-Rp3 is imprinted in the rotational profile of the outer PNS layers. In Fig. 2(h), we see values of q_{PNS} above ~ -1 episodically for both of these models. Indeed, during short time intervals $q_{PNS} \sim 0$, signalling epochs in which the outer third of the PNS rotates nearly rigidly. These values contrast with $q_{PNS} \lesssim -1.5$ for the rest of the models, most of the time. The previous comment also applies to 35OC-Rp4. The time at which the raise of q_{PNS} above -1.5 happens is inversely correlated with the initial poloidal magnetic field strength. While for models 35OC-Rp2 and 35OC-Rp3 these times are ~ 0.5 s and ~ 1.9 s, respectively, for model 35OC-Rp4, the increase of q_{PNS} above -1.5 does not happen during the computed evolution time ($t_{max} = 1.95$ s). Model 35OC-RO only displays a short episode (0.5 s $\lesssim t_{pb} \lesssim 0.7$ s) when $q_{PNS} \gtrsim -1.5$ (Fig. 2h).

The PNS of model 35OC-Rs is strongly affected by the redistribution of angular momentum. Its outer shells contain a significant

fraction of the total angular momentum on roughly the same level as the central layers (Fig. 13c). While the contraction leads to an increase of the fraction of the total mass that resides at the highest densities (until $t_{pb} \sim 0.8$ s), the low-density envelope continues to hold a constant mass (panel b). The specific angular momentum of these layers is so large ($j \geq 2.5 \times 10^{16}$ cm^2 s^{-1}) that they can be self-sustained against the gravitational pull of the PNS. The morphological evolution of this model, whose PNS develops a toroidal shape with a maximum density off-centre (Section 3.2.2) is instigated by the large amount of angular momentum transported outwards. We note that nearly all the angular momentum of the PNS in model 35OC-Rs is concentrated at densities below the nuclear saturation density (Fig. 13c). Differently from models with an initially weak field (e.g. model 35OC-Rw), in this case, the initial field is so strong that no additional, MRI-driven amplification is required to cause the effects described above.

4 EVOLUTION OF THE REMNANT

In the following, we will discuss several aspects of our models relevant to the formation of the central engines of GRBs within either the collapsar or the PM model. The two models rely on the formation of either a BH or a PNS at the centre of the star, respectively, and, in either case, the presence of high angular momentum and strong magnetic fields. Despite a number of important studies on the subject such as the theoretical work by, e.g. Thompson et al. (2004), M11, Metzger et al. (2015), Metzger, Beniamini & Giannios (2018), and simulations (e.g. Bucciantini et al. 2007, 2012; Burrows et al. 2007), the specific requirements for both models are not known to the level of detail that would allow for reliable predictions about the evolutionary path of a given stellar progenitor.

Formally, the subset of models that collapse to a BH might form a GRB central engine, if they may also surround the central compact object with a suitable accretion disc. Our simulations make it abundantly clear that at most moderately relativistic outflows are generated during the fairly long phase of up to more than 2 s in which a PNS exists (before collapsing to a BH), in some cases even strongly magnetized and rapidly rotating. The same is true for the models without a final BH collapse within the time-scales of our runs (in one model ~ 9 s have been computed), which we consider potential PM cases. Among these cases, the final fate of the compact remnant will depend upon the amount of mass accreted on to the PNS on time-scales significantly longer than we have been able to compute so far. It is, however, clear that models in which the PNS mass has stopped growing (or the mass growth is small after the whole iron core has collapsed, namely, $\langle \dot{M} \rangle < 0.05$ M$_\odot$ s^{-1}; where $\langle \dot{M} \rangle$ denotes a time averaged value) before reaching the instability threshold set by the EoS are potential candidates to host a PM central engine. Hence, for all cases, we must extrapolate our simulation results to later times in order to infer the possibilities of a subsequent GRB engine.

4.1 Collapsar candidates

For initial models with stellar or sub-stellar magnetic field, centrifugal forces cause several of the cores to develop a strongly oblate shape. Although the processes accompanying the formation of a BH at the centre of the core will certainly induce perturbations of this structure, the long-term survival of the outer PNS layers beyond BH formation seems likely. This is because its stability against gravity is provided by centrifugal forces to a much higher degree than by the gas and neutrino pressure gradients. Consequently, even a sudden reduction of the thermal support would not lead to a prompt accretion

of these layers. Consisting of matter with specific angular momentum in excess of $j > 1.5 \times 10^{16}$ cm^2 s^{-1} and undergoing infall of gas exceeding this value, they are very likely to orbit the newly formed BH for many dynamical time-scales, only to be accreted gradually as a result of the slower processes governing the redistribution of angular momentum. Besides the fate of the high specific angular momentum of the aforementioned outer layers of the PNS, there are stellar layers (located at mass coordinates >7.5 M$_\odot$; Fig. 1) whose specific angular momentum is large enough to be able to form an accretion disc. We note that models with a successful SN explosion do not halt completely the accretion process (see below). Therefore, we deem most of our BH-forming models promising collapsar candidates. The only likely exception to this estimation is model 35OC-Sw, which due to its low specific angular momentum may hardly form an accretion disc around the formed BH (Fig. 1b).

4.1.1 Outflows

In 35OC-RO polar outflows on to the PNS coexist with equatorial downflows. As discussed in Paper I, the success of polar, as opposed to equatorial, shock revival in many of our models (and singularly in model 35OC-RO) is rooted in strong magnetic fields concentrated along the rotational axis. In addition, the pronounced anisotropy of the neutrino emission caused by the rotational flattening of the PNS and, in particular, the neutrinospheres contribute to launching the explosion.

The successful supernova explosion occurs in the form of collimated jets of a fairly high energy. The outflow velocities ($<0.5c$) as well as the propagation speed of the jet head are sub-relativistic ($\lesssim 0.15c$). For stellar progenitors as compact as 35OC (whose radius is $R_* \approx 5.3 \times 10^{10}$ cm), this means the extremely well-collimated outflow that we have identified with the SN ejecta in Paper I, may break out of the surface of the star within less than $t_{BO} \sim 12$ s. Towards the end of the simulation, the mass density at the polar region just outside the neutrinosphere, where the outflows are generated, remains roughly constant. Hence, the mass loading of the jets does not drop significantly for the velocities to increase drastically. At that point, this region contains magnetic fields close to equipartition with the internal energy of the gas. The associated Lorentz forces could continue jet launching independently of neutrino heating. Hence, in case of a strong decrease of the mass density, the energy injection could continue, potentially increasing the outflow velocity to relativistic speeds.

4.1.2 Accretion disc formation

The (baryon-rich, moderately magnetized, and sub-relativistic) SN ejecta must eventually be caught up by the baryon-free, ultrarelativistic ejecta, which is responsible for the GRB itself. The alluded ultrarelativistic outflow is the sought for byproduct of the collapsar central engine. However, the formation of the collapsar requires that the accretion disc forms. According to the estimate of equation (1), $t_{DF} \sim 9.3$ s in models bearing the original stellar rotation profile (Table 1). Hence, in our models, $t_{BO} - t_{DF} \approx 2$–3 s. It is, nevertheless, not unlikely that the disc formation time be longer than twice the free-fall time from a given mass shell in the star if strong magnetorotational explosions take place. In Fig. 16(a), we show the space-time trajectories of mass-shells along the equator that would fall to $r \approx 0$ from its initial location $r = r(M)$ on a time, $t_{FF}(M)$, equal to the expression of the disc formation time equation (1) but replacing M_{DF} by M, in the progenitor 35OC-RO (coloured, thick lines), as well as the actual trajectories computed from the same
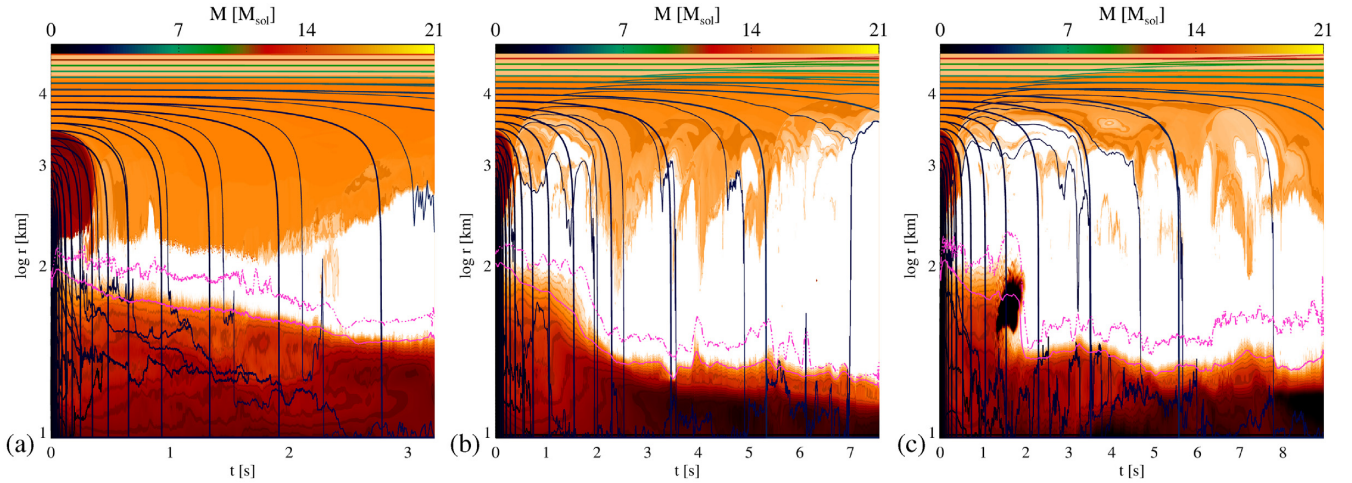
Figure 16. The background (orange shades) represents the entropy per baryon (lighter shades correspond to higher entropy) as a function of radius and time along the equator. Overlaid, we represent with thick solid lines the space-time trajectories corresponding to mass shells falling from a certain mass coordinate, M, according to an effective gravitational potential $-GM/(4r)$ (without accounting for any centrifugal effect), such that the fall time from $r(M)$ to $r = 0$ corresponds to a time $t_{FF}(M)$ as given by equation (1) replacing M_{DF} by M. The colours of the lines correspond to the mass from which each mass-shell falls (see upper colour bar). The thin solid lines represent the actual space-time trajectories followed by the mass-shells along the equator. The solid and dashed–triple-dotted pink lines in each panel correspond to the equatorial PNS radius and to the equatorial gain radius, respectively. The panels (a), (b), and (c) correspond to models `35OC-RO`, `35OC-Rp2`, and `35OC-Rp3`, respectively.

selected subset of mass-coordinates (black, thin lines). We note that for model `35OC-RO`, the estimated value of $t_{FF}(M)$ (roughly equal to the point where the coloured, thick lines intersect the horizontal axis) overestimates the actual fall time. However, for models `35OC-Rp2` and `35OC-Rp3` the opposite is true: $t_{FF}(M)$ underestimates the actual falling time (Figs 16b and c). This is because the ram pressure of the explosion ejecta partly counterbalances the free-fall of the outer stellar layers, very specially, in a broad wedge around the rotational axis, but also along the equator. The deviation between $t_{FF}(M)$ and, hence of $t_{DF} \equiv t_{FF}(M_{DF})$ and the true fall time increases as the SN shock progresses along the equator (the location of this shock roughly corresponds to the transition between white and orange shades). As a result, we estimate that $t_{BO} < t_{DF}$, i.e. we find it very plausible that the SN ejecta breaks out of the stellar surface before the accretion disc forms and, hence, before the GRB jet is launched. If this happens the minimum luminosity that may yield a GRB jet able to break through the star and the SN ejecta may be (significantly) lowered, since the SN ejecta partly clears out the way to the GRB jet (e.g. Aloy et al. 2018). The observational consequences of the GRB jet breaking through the SN outside of the original stellar progenitor are beyond the scope of this paper. Nevertheless, we anticipate that they will strongly depend on the optical thickness of the medium outside of the progenitor star.

4.2 NS-forming models

Next, we assess the viability of the PM mechanisms looking to some of the properties that are expected to be fulfilled by the PMCs considered in Section 3.2.

4.2.1 Rotational Period and shape evolution

The PM and collapsar candidates show a similarly parallel evolution in terms of the their spin period, $\bar{P} := 2\pi/(J_{PNS}/I_{PNS})$, during the first second of evolution (Fig. 17a). In most cases, the PNS contraction yields a decrease of the rotational period. The exception to this

behaviour is model `35OC-Rs`, whose surface rotational period begins to increase after an initial phase of decrease (note that this is also the case for the PCs `35OC-Rw` and `35OB-RRw`). PMCs tend to develop surface rotational periods $P := 2\pi/\Omega_{surf} < 5$ ms and smaller spin periods $\bar{P} \lesssim 2$ ms. Models evolved longer (`35OC-Rp2` and `35OC-Rp3`) display a non-monotonic evolution of the spin period, reaching long-term values $1 \lesssim P \lesssim 2$ ms. The PM model of M11 demands that the PNS develops a millisecond period after its contraction ceases. Thus, taking $\bar{P}$ and not P as an estimator of the spin period 'at birth', formally our models satisfy the period requisites of the PM model. We note that previously in the literature (e.g. Fryer & Heger 2000; Heger, Langer & Woosley 2000; Fryer & Warren 2004; Heger, Woosley & Spruit 2005), $\bar{P}$ has been used to estimate the final spin period. However, given the non-monotonic evolution of $\bar{P}$ in the most evolved models (e.g. $\bar{P}$ grows by a factor of 2 between ~ 5 and ~ 7 s for model `35OC-Rp2`), $\bar{P}$ seems only a predictor of the spin period 'at birth' of the NS with a factor of 2–5 for the models at hand. Alternative forms of estimating the spin period (e.g. Ott et al. 2006) are similarly inaccurate since (i) equatorial accretion is ongoing and (ii) magnetic stresses are exchanging angular momentum between the PNS and its surrounding medium. The volume of the PNS, traced by the effective radius $R_{vol} = (3V_{PNS}/4\pi)^{1/3}$ is still (slowly) decreasing after ~ 7.5 s, a behaviour that is modulated by some small-amplitude variations. Thus, formally, models with supra-stellar magnetic field and with a poloidal magnetic field below equipartition with the toroidal field strength satisfy the PM model requisites on the rotational period. The model with initial equipartition between the toroidal and poloidal magnetic field components does not yield a millisecond surface period.

Two of the PMCs (models `35OC-Rs` and `35OC-Rp2`) show some signs of period increase, but for different reasons. The surface rotation of model `35OC-Rs` seems to nearly cease after ~ 0.9 s. As explained in Section 3.2.2, this is, in part, due to the fact that counter-rotating matter ejected from the PNS poles slides down the PNS surface towards the equator. Besides, the average rotational rate over the
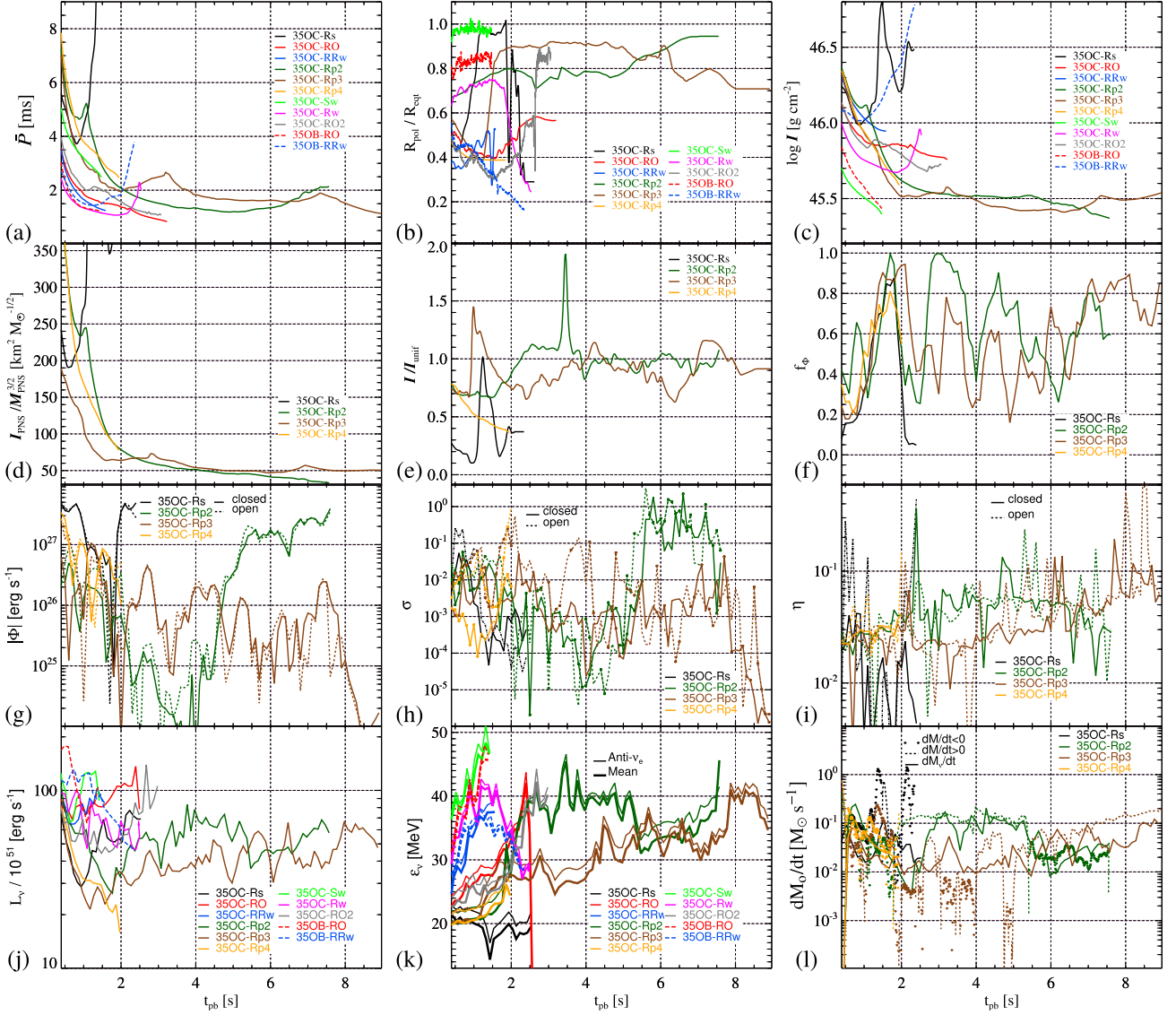
Figure 17. Time evolution of different variables of the models annotated in the legends. The panels display: (a) Period of the PNS. (b) Ratio of polar to equatorial radii of the PNS. (c) Moment of inertia of the PNS. (d) Ratio of the moment of inertia to $M_{PNS}^{3/2}$. (e) Ratio of the moment of inertia of the PNS to the moment of inertia that a uniform sphere with and effective radius $R_{PNS} = (R_{pol} R_{eqt}^2)^{1/3}$ and the same mass would have (equation 10). (f) Fraction, f_Φ, of the PNS surface threaded by open magnetic field lines. (g) Absolute value of the magnetic flux in the open and closed magnetospheric regions. (h) Magnetization, σ, in the open (equation 11) and closed (equation 12) magnetospheric regions. (i) Baryon loading, η, in the open (equation 13) and closed (equation 14) magnetospheric regions. (j) Neutrino mean luminosity (equation 15). (k) Neutrino mean energy (equation 16). (l) Evolution of the mass-loss ($\dot{M}_{PNS} < 0$), and mass gain ($\dot{M}_{PNS} > 0$) compared with the theoretical prediction of equation (23).

whole PNS (defined as $\bar{\Omega} := J_{PNS}/I_{PNS}$) is much smaller in this model than in any other (Table 2), due to including in the averaging counter-rotating regions close to the axis. Another reason for the large period of this model are the morphological changes that it experiences, leading to a toroidally shaped PNS by the end of the computed time (note the large variations in the aspect ratio R_{pol}/R_{eqt} in Fig. 17b). It is, anyway, the (very) strong poloidal field of model 35OC-Rs the responsible for these effects. The analysis of the spin-down of model 35OC-Rp2 after ~ 6 s is deferred to Section 4.3.

The evolution of the shape of a self-gravitating body under the action of dynamically relevant magnetic fields can be interpreted resorting to the virial theorem. According to it, sufficiently large average magnetic field tends to flatten a self-gravitating body in magnetohydrostatic equilibrium (Chandrasekhar & Fermi 1953,

section 4). In spite of the fact that our models are not in equilibrium, the magnetic fields that they develop tend to flatten the PNS (as mentioned in Section 3.4), thus formally obeying the results of the virial theorem. However, the oblateness of the PNS cannot be directly mapped to the magnetic field of the progenitor, since the amplification of the magnetic field is the result of the non-linear (and fairly complex) interplay of different dynamical effects (rotation, convection, MRI, etc.; Section 3.3). Taking aside model 35OC-Rs, Fig. 17(b) suggest that the pole-to-equator radius tends to grow in the PMCs that have been run longer, but the late morphological changes in model 35OC-Rp3, do not allow to give a clear prediction of its longer term value. Model 35OC-Rp2 hints towards an increase of the aspect ratio (developing $R_{pol}/R_{eqt} \lesssim 1$), after the model begins its spin-down ($t_{pb} \sim 5.5$ s; see Section 4.3).

Moment of inertia: The moment of inertia is a relevant quantity not only in the PM model, but also to constrain the equation of state of nuclear matter. The time evolution of the moment of inertia is not monotonic for our models, though it typically decreases in time (Fig. 17c). Changes in time of I_{PNS} reflect the variations in the shape and the mass distribution of the PNS, being the PMC model 35OC-Rs and the PC model 35OB-RRw the ones showing the most abrupt and larger amplitude modulations. Restricting the analysis to the PMCs with longer computed evolution, the moment of inertia remains roughly constant ($I_{PNS} \sim 3 \times 10^{45}$ cm^2 gr^{-1}) after ~ 3 s (Fig. 17c). For a spherically symmetric mass distribution, a relation of the form $I_{PNS} \propto M_{PNS} R_{PNS}^2$ must hold. For simplicity, M11 assume that the moment of inertia of the PNS corresponds to that of a uniform sphere, namely $I_{unif} = 2/5 M_{PNS} R_{PNS}^2$. However, the PNS in our PMCs is more a heterogeneous, oblate ellipsoid or a toroid than a uniform sphere. Hence, characterizing the distribution of the mass around the rotational axis with a single *effective* radius ('R_{PNS}') is neither too accurate, nor unanimously defined. After some experimentation, we find that the PNS moment of inertia can be approximated by

$$I_{unif} = \frac{1}{6} M_{PNS} R_{PNS}^2, \tag{10}$$

where we use as effective PNS radius, $R_{PNS} = (R_{pol} R_{eqt}^2)^{1/3}$, with R_{pol} and R_{eqt} being the polar and the equatorial radii of the PNS, respectively. After ~ 3 s, I_{unif} approximates I_{PNS} with deviations smaller than ~ 30 per cent (Fig. 17e).[5] Compared to the moment of inertia of a uniform sphere with the same effective radius, equation (10) is 2.4 times smaller.

Lattimer & Schutz (2005) show that the ratio $I/M^{3/2}$ remains approximately constant for typical neutron star masses. Different equations of estate yield different constant values though. Using this property, Metzger et al. (2015) infer that $I_{NS} \approx 1.3 \times 10^{45} (M_{NS}/1.4\,M_\odot)^{3/2}$ g cm^2, for a typical value $I/M^{3/2} \approx 50$ km$^2\,M_\odot^{-1/2}$ and PM of mass $M_{NS} \approx 1.4\,M_\odot$. Applied to the mass of the PNS of models 35OC-Rp2 and 35OC-Rp3, i.e. $M_{PNS} \simeq 2.3\,M_\odot$, we obtain $I_{PNS} \approx 2.3 \times 10^{45} (M_{PNS}/2.3\,M_\odot)^{3/2}$ gr cm^2, which approximates the actual value of the moment of inertia within less than 40 per cent error at the end of the computed time (see also Table 1). We note, however, that the ratio $I_{PNS}/M_{PNS}^{3/2}$ evolves non-monotonically in our PMCs (Fig. 17d). After sufficient time (~ 3 s), the relative change in $I_{PNS}/M_{PNS}^{3/2}$ significantly decreases. For model 35OC-Rp3, $I_{PNS}/M_{PNS}^{3/2}$ settles to a value of ~ 50 km$^2\,M_\odot^{-1/2}$, while in model 35OC-Rp2, it is moderately decreasing by the end of the computed time, when it reaches a value ≈ 30 km$^2\,M_\odot^{-1/2}$.

4.2.2 Surface magnetic fields

Based on stability arguments, M11 argued that the field of the PNS is dominated by a toroidal component about an order of magnitude stronger than the poloidal one. As the averages of the ratio between field components on the PNS surface (identified here with the ν_e-sphere; Fig. 15c) show, not all our PMCs exactly agree with this estimate. Model 35OC-Rs owes its extraordinarily strong poloidal field to the initially very strong magnetic field with equipartition in the poloidal and toroidal components (equipartition that is preserved during the computed evolution). Thus, model 35OC-Rs displays

$b^{pol}/b^{tor} \gtrsim 1$ throughout most of its evolution. Also in model 35OC-Rp4, the two components of the magnetic field reach equipartition very early on and stay at that level during the computed evolution. On the other extreme, for model 35OC-Rp2 (with the smallest initial poloidal field of all PMCs) the poloidal field decreases during the interval $0.4 \lesssim t_{pb} \lesssim 3.4$ s (Fig. 15c; green line), while the toroidal component attains a level $3 \times 10^{14} \lesssim b^{tor} \lesssim 10^{15}$ G (Fig. 2l). The dynamics radically changes after $t_{pb} \gtrsim 3.4$ s, highlighting the need of performing very long-term computations of the post-collapse remnant. After that time, model 35OC-Rp2 exhibits a nearly exponential growth of the surface poloidal field component (see Section 3.3). This behaviour is connected to the much longer accretion time of the iron core in PMCs than in PCs. For instance, in the case of model 35OC-Rp2 the magnetized iron core (see Fig. 1) is finally accreted after ≈ 2 s. This episode of accretion can be traced by the mass-shell that at $t_{pb} = 0$ is located at $r \approx 2700$ km. It falls down to ~ 700 km and then is lifted up and accreted again twice, until it begins falling down more precipitously at $t_{pb} \sim 2$ s (Fig. 16b). The change in the growth of the poloidal field of the PNS is, in part, reflecting the magnetic structure of the pre-SN star, with a weak poloidal component limited to the iron core and a couple of shells located much further away from the centre (Fig. 1). Consequently, during an extended interval of time after the accretion of the iron core, very little additional field is accreted on to the PNS. During this period, the vigorous convection in the PNS amplifies the poloidal field, while rotational winding into toroidal field continues and increases the latter component. This outcome might be modified in the presence of a genuinely 3D dynamo, as our preliminary 3D models show (there convection can be found, though no similar growth in the surface field). Model 35OC-Rp3 reaches a value $b^{pol}/b^{tor} \sim 0.1$ after about 4 s, though with significant variations after 7.5 s. This model would roughly fit within the parametrization of M11. However, since relatively small variations in the poloidal field strength of the progenitor result in significantly different values of the ratio b^{pol}/b^{tor} (compare, e.g. the evolution of models 35OC-Rp2 and 35OC-Rp3 in Fig. 15c), we cannot robustly confirm the assumptions in M11 on the poloidal to toroidal field strength ratio.

An important parameter regulating the rotational energy loss as well as the mass-loss rate in isolated, magnetized neutron stars is the fraction of the neutron star surface threaded by open magnetic flux, f_Φ (e.g. M11; Margalit et al. 2018; Metzger et al. 2018). The fraction of the PNS surface threaded by open field lines displays large changes during the evolution (Fig. 17f). For instance, in models 35OC-Rp2 and 35OC-Rp3 f_Φ fluctuates between ~ 0.2 and 1 for $t_{pb} \gtrsim 2$ s as a consequence of the variable accretion down flows that hit the PNS surface. That unsteady mass flow on to the PNS also limits the accuracy of our prescription to distinguish between open and closed magnetic field lines, namely, that the field line extends for more than 200 km in the radial direction or that it traverses unbound matter. Hence, the computed values of f_Φ should be taken with some care and using, e.g. $f_\Phi \sim 0.5$ (as in Metzger et al. 2018) is accurate within a factor of ~ 1.5.

M11 further assume that the contraction of the PNS happens at constant magnetic flux, Φ_c, through the region of the PNS surface threaded by closed magnetic field lines. They argue that this is a good approximation if the field growth occurs rapidly, via MRI or the action of convective dynamos. We find that the approximation of constant magnetic flux in either the closed or the open magnetospheric region is only roughly fulfilled, within an order of magnitude, by model 35OC-Rp3 for 2 s $\lesssim t_{pb} \lesssim 8$ s, but not so much by the rest of the PMCs (model 35OC-Rp4 may have not evolved enough to draw a strong conclusion; see Fig. 17g). The rough qualitative agreement

---

[5]The large peak at $t \approx 3.4$ s in model 35OC-Rp2 is due to an inaccurate determination of the polar radius for a short period of time; see the sudden fall-down of R_{11} in Fig. 10.

of the magnetic flux in the closed magnetosphere of model 350C-Rp3 with the M11 assumption happens because the magnetic field in this model is amplified very soon after core bounce. Later on, it shows neither significant variations of the magnetic energy in the whole PNS (Fig. 2i) nor in the surface magnetic field (Figs 2k and l). Hence, its magnetic flux in the closed magnetospheric region is roughly constant and relatively small, $\Phi_c \lesssim$ few $\times 10^{25}$ G cm^2. In the case of model 350C-Rp2 we have identified a period of significant (poloidal) magnetic field growth ($3.5 \lesssim t_{pb} \lesssim 6$ s) driven by vigorous convection (Section 3.3). During a significant fraction of the convective growth of this model ($2.2 \lesssim t_{pb} \lesssim 4.5$ s), the magnetic flux in closed field lines is quite small, $\Phi_c \lesssim 10^{25}$ G cm^2 and roughly constant (within one order of magnitude) too. However, later on, both Φ_c and the magnetic flux in the open magnetospheric region, Φ_o, grow towards values $\sim 3 \times 10^{27}$ G cm^2. We find significant that the magnetic flux for model 350C-Rp2 is reasonably constant for 5 s $\lesssim t_{pb} \lesssim 6.5$ s, since during that time interval this model shows an episode of electromagnetic spin-down accompanied by wind ejection (see Section 4.3).

We define the magnetization parameter, σ, as the ratio of Poynting ($\mathcal{P}$) to mass ($\dot{\mathcal{M}}c^2$) flux at the PNS surface. Its time evolution for PMCs is shown in Fig. 17(h). Due to the very complex interplay between accretion and ejection of mass on to/from the PNS surface, σ has large variations with latitude and time. We display with different line styles the value of σ in parts of the surface threaded by either open or closed field lines. Precisely, we define

$$\sigma_o := \left(\sum_{i_o j_o} \mathcal{P}_{i_o j_o} \right) \Big/ \left(\sum_{i_o j_o} \dot{\mathcal{M}}_{i_o j_o} c^2 \right), \tag{11}$$

$$\sigma_c := \left(\sum_{i_c, j_c} \mathcal{P}_{i_c j_c} \right) \Big/ \left(\sum_{i_c j_c} \dot{\mathcal{M}}_{i_c j_c} c^2 \right), \tag{12}$$

where the subscripts i_o (i_c) and j_o (j_c) annotate the radial, r_{i_o} (r_{i_c}), and polar, θ_{j_o} (θ_{j_c}) discrete locations on the $\rho = 10^{10}$ g cm^{-3} isodensity surface (slightly above the PNS surface) threaded by open (closed) magnetic field lines. The apparent trend is that smaller values of the initial poloidal magnetic field yield larger values of the magnetization at the PNS surface in the mid term. Typical values $10^{-4} \lesssim \sigma \lesssim 10^{-1}$ alternate with relatively short episodes in which σ rises very significantly in most PMCs. For instance, model 350C-Rp2 shows a prolonged episode of relatively large values $\sigma \gtrsim 10^{-3}$ after $t_{pb} \sim 5$ s. During the episodic rise of σ we find values $0.1 \lesssim \sigma \lesssim 10$, in qualitative agreement with M11 for a similar evolutionary time after bounce. Stated differently, we observe a qualitative agreement with the conditions of the PM model, namely that in coincidence with the episode of spin-down of model 350C-Rp2 (and also preceding it), σ soars quickly. Typically, the values of σ_o are, within the same order of magnitude as σ_c, although episodically σ_o may be 100 times larger than σ_c (e.g. in model 350C-Rp3 between $3 \lesssim t_{pb} \lesssim 4$ s).

We have also monitored the baryon loading, η, in our models. The baryon loading is defined as the ratio of kinetic ($\mathcal{K}$) to mass flux (e.g. Bugli et al. 2020):

$$\eta_o := \left(\sum_{i_o j_o} \mathcal{K}_{i_o j_o} \right) \Big/ \left(\sum_{i_o j_o} \dot{\mathcal{M}}_{i_o j_o} c^2 \right), \tag{13}$$

$$\eta_c := \left(\sum_{i_c, j_c} \mathcal{K}_{i_c j_c} \right) \Big/ \left(\sum_{i_c j_c} \dot{\mathcal{M}}_{i_c j_c} c^2 \right). \tag{14}$$

Values of $\eta \lesssim 1$ highlight the mildly relativistic character of the outflow in our models. Even more than in the case of σ, the values

of the baryon loading are similar for regions of the magnetosphere enclosing open and closed field lines (Fig. 17i). This is remarkable in view of the fact that the open field lines are associated to regions of outflow above the poles of the PNS, while the closed field lines more closely trace the regions of equatorial inflow.

4.2.3 Neutrino cooling evolution

An important quantity that determines the mass-loss rate and the temperature evolution of the PNS is the neutrino luminosity. Following M11, we define the average neutrino luminosity, L_ν, including the contributions of neutrinos and antineutrinos weighted by their own spectral energies averaged over the neutrino ($|\epsilon_{\nu_e}|$) and antineutrino ($|\epsilon_{\bar{\nu}_e}|$) absorption cross-section as

$$L_\nu \epsilon_\nu^2 := L_{\nu_e} |\epsilon_{\nu_e}|^2 + L_{\bar{\nu}_e} |\epsilon_{\bar{\nu}_e}|^2, \tag{15}$$

where ϵ_ν is the neutrino mean energy

$$\epsilon_\nu := \frac{\sum_j \left(|\epsilon_{\nu_e}|(\theta_j) L_{\nu_e}(\theta_j) + |\epsilon_{\bar{\nu}_e}|(\theta_j) L_{\bar{\nu}_e}(\theta_j) \right)}{\sum_j \left(L_{\nu_e}(\theta_j) + L_{\bar{\nu}_e}(\theta_j) \right)}. \tag{16}$$

The sum extends over all polar angles θ_j in our models, and the quantities in the last expression are computed for each angular cell corresponding to the iso-density surface $\rho = 10^{10}$ g cm^{-3}. Figs 17(j) and (k) show the evolution of the average neutrino luminosity and of the neutrino mean energy, respectively. We observe that the values of L_ν and of ϵ_ν in all our models are correspondingly larger than the ones shown in fig. A1 of M11, which includes the cooling curves from (non-rotating) models of Pons et al. (1999) and Hüdepohl et al. (2010). The comparison to the previous models of PNS cooling employed in the PM model is not straightforward, as usual calculations of the cooling evolution begin in the so-called Kelvin–Helmhotz (KH) phase, when accretion and convection have ceased. The KH phase of non-rotating PNS produced after the collapse of less massive progenitors typically begins within 0.5 s after bounce (Burrows 1988; Burrows & Goshy 1993). In our PMCs, the KH phase has not strictly begun since accretion and also convection are both still fully operational in our models (even after more than 8 s in the case of model 350C-Rp2). These large values of L_ν result from the competition between two opposite effects. On the one hand, the mass of the PNS of our models is larger than the largest PNS mass included in M11 (namely, 2 M$_\odot$), and larger PNS mass yields larger L_ν and ϵ_ν, but most importantly, accretion on to the PNS has not ceased. Indeed, the equatorial accretion feeds the emission of neutrinos significantly, compared with isolated neutron stars. On the other hand, our models are rotating very fast, which should yield a reduction in both the mean neutrino luminosity and its mean energy, accompanied by a correspondingly longer cooling time-scale (since rapid rotation lowers the inner temperature of the PNS; e.g. Thompson et al. 2005). We find that, in spite of the fast rotation of our models, the effect of the mass accretion on to the PNSs explains the larger values of L_ν of our models with respect to the most massive models of M11. Also, mean neutrino energies in excess of 30 MeV are observed for the more evolved PMC models (350C-Rp2 and 350C-Rp3). Comparatively, PCs display a faster growth of the mean neutrino energy and relatively larger values of L_ν than PMCs within the first ~ 1.5 s of evolution. This behaviour is connected to the typically smaller polar radii of PCs compared to PMCs (Fig. 17b), which makes that the neutrinospheres are located closer to the centre in the polar regions, and thus, the temperature at last scattering neutrino-matter surface is consistently larger.

The values of L_ν and ϵ_ν are important to set the mass-loss rate from the PNS in general, and particularly, in the model of M11. It is well known that neutrinos may carry away a sizeable fraction of the PNS rest-mass energy that, in our case, owed to the large PNS mass may be $\sim 0.43\,M_\odot c^2 (M_{\rm PNS}/2.3\,M_\odot)^2$ (Lattimer & Prakash 2001). We note that our PMCs run longer display typical mean luminosities $\sim 4 \times 10^{52}\,{\rm erg\,s^{-1}}$ after $t_{\rm pb} \sim 2\,$s and extending over more than $\sim 6\,$s, implying an emission of equivalent rest-mass energy $\sim 0.13 M_\odot c^2$ during the late post-bounce evolution. In order to obtain a theoretical estimate of the mass-loss rate induced by neutrinos, one may employ the results of Qian & Woosley (1996), valid for spherically symmetric, non-rotating PNSs:

$$\dot{M}_\nu = 2.5 \times 10^{-5} M_\odot {\rm s}^{-1} \left(\frac{L_\nu}{10^{52}\,{\rm erg\,s^{-1}}}\right)^{5/3} \left(\frac{\epsilon_\nu}{10\,{\rm MeV}}\right)^{10/3}$$
$$\times \left(\frac{M_{\rm PNS}}{2\,M_\odot}\right)^{-2} \left(\frac{R_{\rm PNS}}{10\,{\rm km}}\right)^{5/3} (1+\epsilon_{\rm es})^{5/3} \quad , \quad (17)$$

with $\epsilon_{\rm es} \simeq 1$ is a small correction that accounts for the extra heating due to inelastic electron scattering

$$\epsilon_{\rm es} = 0.29 \left(\frac{M_{\rm PNS}}{2\,M_\odot}\right) \left(\frac{R_{\rm PNS}}{10\,{\rm km}}\right)^{-1} \left(\frac{\epsilon_\nu}{10\,{\rm MeV}}\right)^{-1}. \quad (18)$$

Next, $\dot{M}_\nu$ is modified to account for the effects of rotation and the fact that mass-loss resulting into unbound matter is only possible along the fraction of the magnetosphere threaded by open field lines, f_Φ (open field lines approximately span the two polar caps in the range $0 \le \theta \le \theta_{\rm open}/2$). The centrifugal force enhances the mass-loss rate approximately by a factor (see M11)

$$f_{\rm cent} = \exp[(P_{\rm c}/P)^{1.5}](1-\exp(-\zeta)) + \exp(-\zeta), \quad (19)$$

where

$$P_{\rm c} \simeq 1.8 \sin\theta_{\rm open} \left(\frac{R_{\rm PNS}}{10\,{\rm km}}\right)^{3/2} \left(\frac{M_{\rm PNS}}{2\,M_\odot}\right)^{-1/2} {\rm ms}, \quad (20)$$

$$\zeta \simeq \left(\frac{\sigma_{\rm o} c^3}{GM_{\rm PNS}\Omega}\right)^{1/3}. \quad (21)$$

Hence, the overall mass-loss rate in the M11 model is

$$\dot{M}_{\rm M11} = \begin{cases} \dot{M}_\nu f_\Phi, & \theta_{\rm open}/2 \ll \pi/2 \\ \dot{M}_\nu f_\Phi f_{\rm cent}, & \theta_{\rm open}/2 \gtrsim \pi/2 \end{cases} \quad (22)$$

In equation (22), we have omitted the branch corresponding to mass accretion rates below the Goldreich–Julian rate, since it may only apply in the very long-term evolution, not reached by our models. In Fig. 17(l), we show (solid lines) the instantaneous values of

$$\dot{M}_{\rm o} = \dot{M}_\nu f_\Phi \quad (23)$$

compared with the actual time evolution of $\dot{M}_{\rm PNS}$, distinguishing between episodes of mass ejection (displayed with symbols) and accretion (using dashed lines). Including the factor $f_{\rm cent}$ as in expression (22) yields a mass-loss rate orders of magnitude above the values measured in our PMCs and, besides, it is not totally justified in our models, where most of the mass-loss happens along the polar caps of the PNS. Remarkably, the theoretical prediction for the mass-loss rate employing equation (22) agrees, within factors of $\lesssim 3$, with the computed mass-loss rate during the episodes of net mass ejection from the PNS for models 35OC-Rp2, 35OC-Rp3, and 35OC-Rp4. The agreement is surprisingly good during the epochs of net mass accretion on to the PNS. This is likely because the mass-loss rate analytically estimated for spherically symmetric neutrino-driven winds (equation 17) is derived from continuity arguments that apply identically to wind outflows and mass accretion.

We furthermore check another of the requirements of the M11 model. These authors state that the neutrino-driven mass-loss rate is unaffected by the magnetic field for dipole (poloidal) fields $B_{\rm dip} \lesssim 3 \times 10^{16}$ G. None of our models reaches values of the poloidal magnetic field larger than a few $\times 10^{15}$ G. However, the mass-loss rate does not fit with the theoretical estimates for model 35OC-Rs that is endowed with the largest initial dipolar field (still significantly below the aforementioned threshold value). This discrepancy can be seen comparing the black (solid) line to the dashed line and the black symbols in Fig. 17(l). Other PMCs whose PNSs reach poloidal magnetic fields smaller than that of model 35OC-Rs, seem to roughly fit (again, within one order of magnitude) with the assumption that the neutrino-driven mass-loss rate is not notably affected by the presence of the magnetic field.

4.3 PMC spin-down

The PNS may exchange angular momentum with the surroundings, either incorporating it by mass accretion, releasing it by mass ejection or by the action of Maxwell stresses. Likewise, the energy exchange between the PNS and the medium surrounding it is mediated by magnetic fields, mass exchange and neutrinos. Among the PMCs we have identified one case in which an incipient spin-down phase has begun, and we discuss it here in detail for its interest as the central engine of a long-duration GRB.

Starting around $t_{\rm pb} \sim 5.5\,$s, model 35OC-Rp2 launches an outflow powered by the spin-down of the PNS. During this period, angular momentum is extracted at high rates by the strong magnetic field. Consequently, the rotational energy decreases to about 25 per cent of its maximum value and the surface average of the angular velocity drops by half. We approximately quantify a rotational spin-down time-scale by computing the quantity $\tau_{\rm rot} := \mathcal{T}^{\rm PNS}/\dot{\mathcal{T}}^{\rm PNS}$. In order to avoid the noise associated to the numerical evaluation of $\dot{\mathcal{T}}^{\rm PNS}$ (Fig. 19b), we take averages of the ratio $\mathcal{T}^{\rm PNS}/\dot{\mathcal{T}}^{\rm PNS}$ over intervals of 25 ms. In Fig. 18(a), we show the time evolution of $\tau_{\rm rot}$ (solid lines) for models 35OC-Rp2 and 35OC-Rp3. Values of $|\tau_{\rm rot}| \sim 2-3\,$s are a typical during the spin-down phase $5.3 \lesssim t_{\rm pb} \lesssim 7.6\,$s of model 35OC-Rp2. More variable, but typically longer spin-down time-scales ($|\tau_{\rm rot}| \sim 10-40\,$s) are observed in model 35OC-Rp3 in the period $4 \lesssim t_{\rm pb} \lesssim 7.2\,$s. Thus, a 50 per cent increase in the initial poloidal field of model 35OC-Rp3 with respect to model 35OC-Rp2, yields an order of magnitude larger spin-down time-scales.

Also in Fig. 18(a), we show the theoretical prediction of Metzger et al. (2018) for the spin-down time-scale, $\tau_{\rm sd}$, for accreting PNSs (dotted lines). More precisely, we define

$$\tau_{\rm sd} := {\rm sign}(\tau_{\rm rot})\frac{\mathcal{T}^{\rm PNS}}{L_{\rm sd}}, \quad (24)$$

with

$$L_{\rm sd} = \begin{cases} L_{\rm em}(R_{\rm lc}/R_{\rm PNS})^2, & \dot{M} \gtrsim \dot{M}_{\rm ns} \\ L_{\rm em}(R_{\rm lc}/R_{\rm m})^2, & \dot{M}_{\rm lc} \lesssim \dot{M} \lesssim \dot{M}_{\rm ns}, \\ L_{\rm em}, & \dot{M} \lesssim \dot{M}_{\rm lc} \end{cases} \quad (25)$$

where $L_{\rm em} := b_{\rm pol}^2 R_{\rm PNS}^6 \Omega^4/c^3$, $R_{\rm lc} = c/\Omega$ is the light-cylinder radius, and $R_{\rm m} := \left(1.5 b_{\rm pol}^2 R_{\rm PNS}^6/(\dot{M}\sqrt{GM_{\rm PNS}})\right)^{2/7}$ is the Alfvén radius (see Metzger et al. 2018, equation 13). The three branches in equation (25) result from different accretion thresholds, namely,

$$\dot{M}_{\rm ns} \simeq 0.086 b_{\rm pol,15}^2 M_{1.4}^{-1/2}\,M_\odot\,{\rm s}^{-1}, \quad (26)$$

that limits the accretion rate when $R_{\rm m} = R_{\rm PNS}$, and

$$\dot{M}_{\rm lc} \simeq 6.9 \times 10^{-4}\,b_{\rm pol,15}^2\,P_{\rm ms}^{-7/2}\,M_{1.4}^{-1/2} M_\odot\,{\rm s}^{-1}, \quad (27)$$
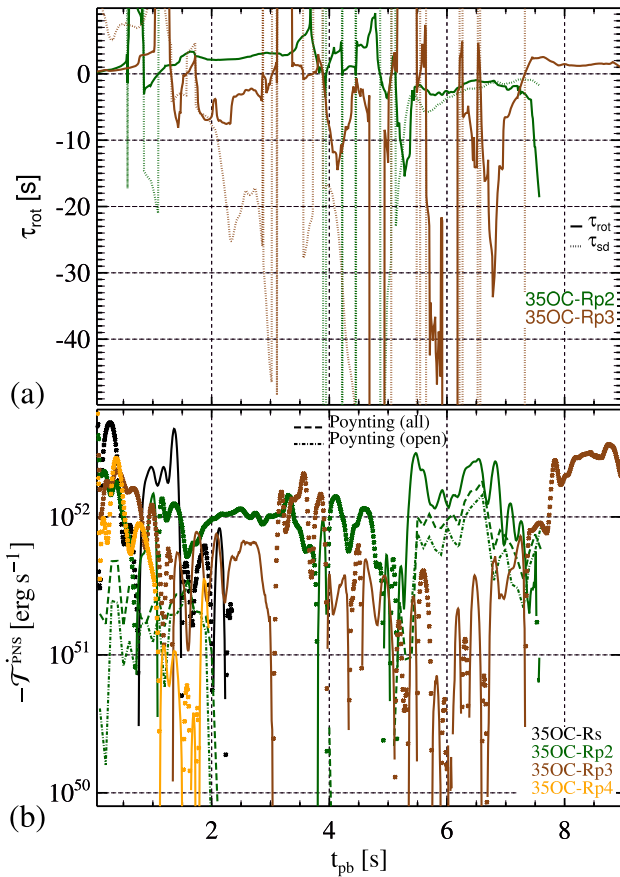
Figure 18. Panel (a): evolution of the rotational time-scale $\tau_{\rm rot}$ computed taking averages of the local value of $\mathcal{T}^{\rm PNS}/\dot{\mathcal{T}}^{\rm PNS}$ over intervals of 25 ms. Note that $\tau_{\rm rot} < 0$ ($\tau_{\rm rot} > 0$) correspond to times in which $\dot{\mathcal{T}}^{\rm PNS} < 0$ ($\dot{\mathcal{T}}^{\rm PNS} > 0$), corresponding to a spin-down (spin-up) of the PNS. Panel (b): rotational luminosity, $-\dot{\mathcal{T}}^{\rm PNS}$. The instants of time in which $-\dot{\mathcal{T}}^{\rm PNS} < 0$ (the PNS spins up) are represented with symbols, while solid lines correspond to times in which $-\dot{\mathcal{T}}^{\rm PNS} > 0$ (the PNS spins down). With dashed-dotted (dashed) green lines the Poynting flux enclosed by open (or all, open and closed) field lines is displayed for model 35OC-Rp2.

that operates enhancing the mass accretion rate when the Alfvén radius is smaller than the light-cylinder radius (hence, equation 27 results when $R_{\rm m} = R_{\rm lc}$). We point out that the absolute value of the mass accretion rate on to the PNS never falls below the threshold set by equation (27) in our models. Hence, the lower branch of equation (25) is never met. This is within our expectations, since the spin-down luminosity is mostly as that of a magnetic dipole spin-down for *effectively* non-accreting neutron stars (which is not the case in our models). In the previous equations, $M_{1.4}$ is the mass of the PNS is units of $1.4\,\mathrm{M}_\odot$ and $P_{\rm ms}$ is the rotational period measured in milliseconds. We have included the sign($\tau_{\rm rot}$) in equation (24) in order to easy the comparison with $\tau_{\rm rot}$.

The agreement between $\tau_{\rm rot}$ and $\tau_{\rm sd}$ during the epoch of spin-down for model 35OC-Rp2 is remarkable, reinforcing our interpretation that we are observing a transient PM spin-down episode in that model. The agreement between the theoretical spin-down time-scale and $\tau_{\rm rot}$ is only within one order of magnitude in the late (very mild) spin-down episode of model 35OC-Rp3 ($4 \lesssim t_{\rm pb} \lesssim 7.3\,$s) and within a factor of 3 during the first extended spin-down episode of this model ($1.3 \lesssim t_{\rm pb} \lesssim 3\,$s).
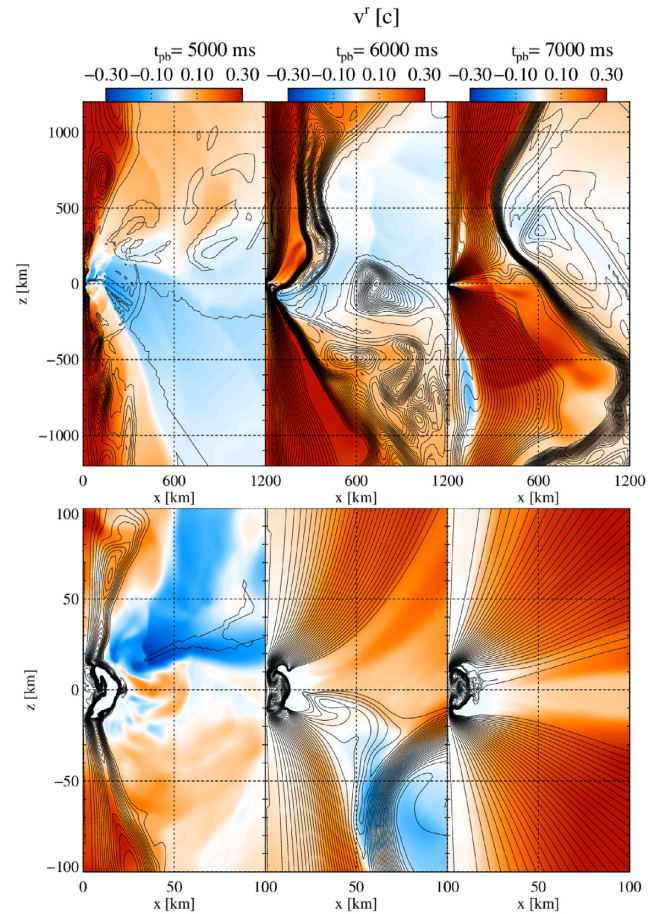

Figure 19. Generation of the late-stage rotationally-driven outflow of model 35OC-Rp2. We show the radial velocity in units of the speed of light and magnetic field lines. Top and bottom panels show a region of 1200 km and a zoom on to the innermost 100 km, respectively.

The spin-down phase is characterized by a layer of very strong field surrounding the rotational axis at a distance of several hundreds of kilometres and separating the outflow from falling matter outside (compare the late stages, $t_{\rm pb} = 6, 7\,$s in Fig. 19 to the earlier one at $t_{\rm pb} = 5\,$s). In this layer, the magnetic field dominates over the internal and kinetic energies, wherefore it is able to prevent the accretion on to the PNS. Approximately in spatial coincidence with the aforementioned layer, we may find the Alfvén surface. This Alfvén surface is located at a distance from the rotational axis which exhibits large variations in time, especially close to the equator. There it is not uncommon that it episodically shrinks until it hits the PNS surface. The epoch of spin-down is strongly correlated with periods in which the Alfvén surface is located further away along the equator (Fig. 19), hence enabling an efficient magnetorotational braking (as the ejected matter from the PNS is forced to nearly corotate -specially along closed magnetic field lines- with the angular frequency of the PNS surface; cf. Thompson et al. 2004). Indeed, the spin-down is so efficient during the late-time episode in model 35OC-Rp2 that it seems to be caused by a propeller mechanism (Romanova et al. 2004). However, our models do not enter the propeller regime, though they are not too far off. The magnetic field does not fully enforce corotation in the magnetically dominated layer around the PNS, but is not too far from that. Thus, rotation is not fast enough to expel matter by centrifugal forces.

Towards the end of the simulation, the PNS is at the centre of a magnetic field whose poloidal component is predominantly radial and has a monopolar geometry that transfers rotational energy to the surrounding gas. The field launches a wind that is, in contrast to earlier epochs and to all other models, highly isotropic. Only after several hundred km, the gas is collimated by the surrounding stellar core into a pair of jets streaming along the axis, in qualitative agreement with the findings of Uzdensky & MacFadyen (2007) and Bucciantini et al. (2007), Bucciantini et al. (2008).

M11 assume that the contraction of the NS happens at constant angular momentum. As we can see from Fig. 2(f), after ~ 2 s, the angular momentum of the PNS displays a moderate time evolution, that drives changes in J_{PNS} of less than a factor of 2 within $\sim 5-7$ s. Thus, even if the assumption of M11 does not strictly hold, it is broadly compatible with our results. Although neutrinos may contribute to reduce the angular momentum of the PNS by ~ 43 per cent in favourable cases (e.g. Janka 2004), here the main driver of angular momentum loss is the magnetic braking combined with the ejection of mass from the PNS surface.

5 OUTLOOK: 3D MODELS

Deferring a thorough investigation of our 3D models to a subsequent article, we conclude this section by placing them in the context of the present study. Key quantities discussed above for the axisymmetric models are presented in Fig. 20. As described in Paper I, model `35OC-RO-3d` undergoes a delayed shock revival driven by magnetic fields and neutrino heating, while model `35OC-Rs-3d` develops a prompt explosion powered by the strong magnetic field. Hence, despite quantitative differences, the models behave similarly to the axisymmetric versions. The similarities extend to the jet-like morphology of the ejecta propagating at moderately relativistic speeds along the rotational axis. Accretion on to the PNSs, on the other hand, is weaker in 3D than in 2D, causing their masses to stop growing already within the first half-second after bounce. Though the simulations could only be run for a shorter time, a collapse to a BH seems unlikely on time-scales similar to those observed in 2D. Hence, the parameter space for collapsars formation is more restricted in 3D.

The evolution of the PNSs puts both models into the regime of PMCs. Their rotational energy corresponds to up to $\beta_G \lesssim 2$ per cent with the gravitational energy, i.e., of the same order as in axisymmetry. Hence the development of dynamical instabilities seems limited in our 3D models, backing up our long-term 2D calculations. While model `35OC-RO-3d` approaches a roughly constant value of $\beta_G \approx 1.8$ per cent, the rotational energy of model `35OC-Rs-3d` enters a rapid decline after peaking at $\beta_G \approx 1.6$ per cent. Both tendencies parallel the evolution of the axisymmetric versions, though at a more quantitative level the early end of the accretion on to the PNS limits the 3D models to values that are below the 2D versions. Like in 3D, only a small fraction of the total rotational energy is in the form of free rotational energy. Both models reach similar levels $\mathcal{F}^{PNS} \approx 10^{51}$ erg corresponding to a fraction $\mathcal{F}^{PNS}/|\mathcal{W}| \sim 10^{-3}$ of the gravitational energy. Similarly to the rotational energy, the angular momentum grows, but not quite as much as in 2D. Both models reach a maximum of J_{PNS} around the time the PNS mass ceases to increase. In the case of model `35OC-RO-3d`, the subsequent decline eventually slows down and J_{PNS} levels off, whereas model `35OC-Rs-3d` does not reach a stationary value by the end of the simulation. The PNSs develop rotational frequencies exceeding 10^3 s^{-1}. The angular velocity on the PNS surface of model `35OC-RO-3d` exceeds the volume average, $\bar{\Omega}$, by at least 30 per cent
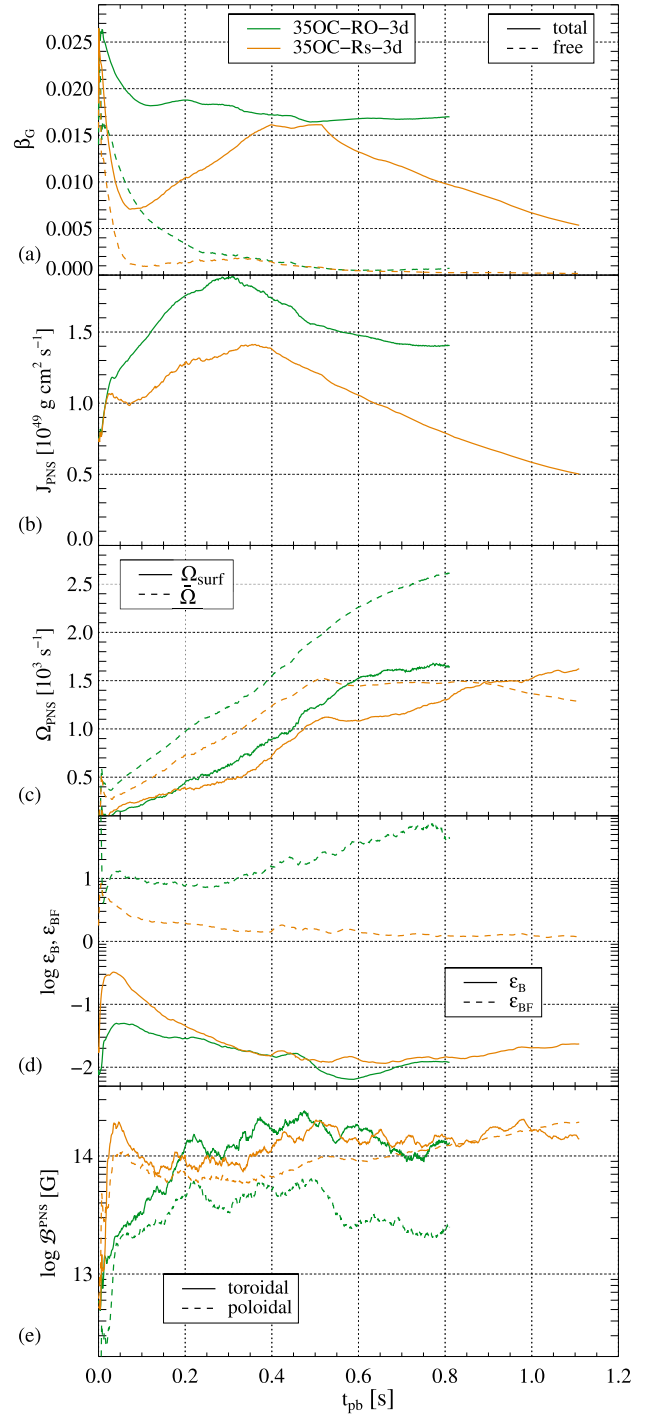

Figure 20. Global quantities of the PNSs of the 3D versions of models `35OC-RO` and `35OC-Rs`: from top to bottom, the panels show the ratio of the total and free rotational energy to the gravitational energy, the angular momentum, the angular frequency on the surface and averaged over the PNS, the ratio of the magnetic energy to the total and free rotational energy, and the average surface magnetic field strength.

throughout the evolution, indicating a high degree of differential rotation. In model `35OC-Rs-3d`, the two measures of the rotational velocity become similar after $t_{pb} \approx 0.7$ s, pointing toward a more rigid internal rotational profile. In both models, the growth of $\bar{\Omega}$ is only very gradual at late times.
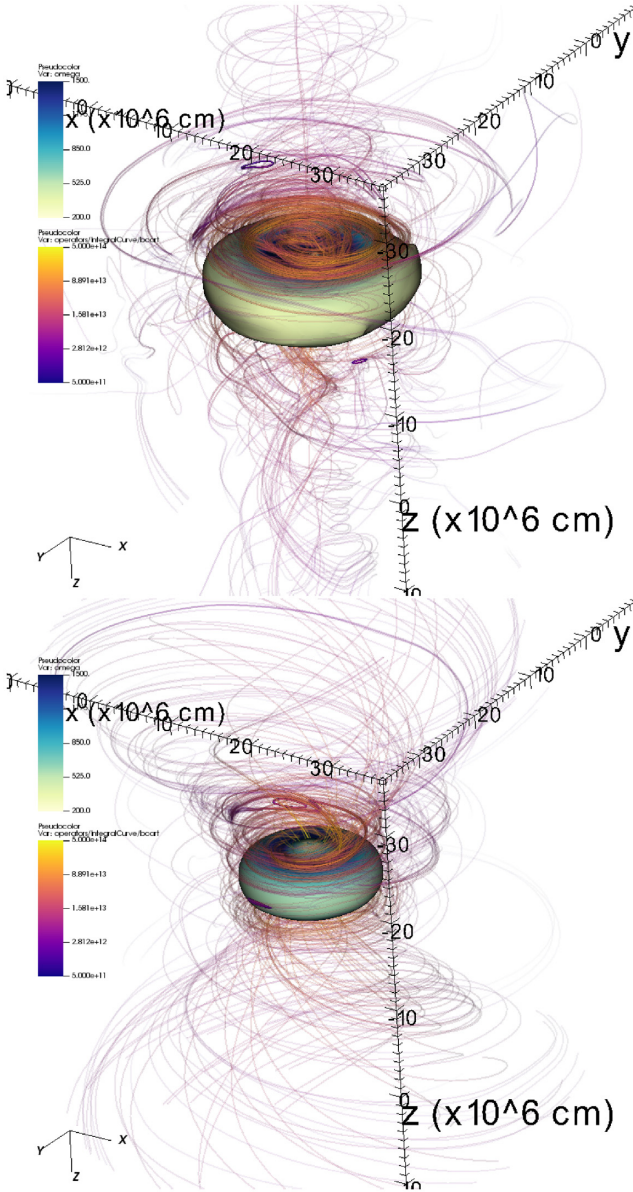
Figure 21. Structure of the PNS and its immediate surroundings in the 3D versions of models 35OC-RO ($t_{pb} \approx 0.81$ s, top) and 35OC-Rs ($t_{pb} \approx$ 1.15 s, bottom panel). Both panels present the angular velocity of the gas on isodensity surfaces of $\rho = 10^{10}$ g cm^{-3} and magnetic field lines with the colour scale showing the field strength.

Both PNSs possess strong magnetic fields, which, despite the large differences in pre-collapse magnetization, converge to similar magnitudes. Towards the end of the simulations, their energies account for around 1 per cent of the total rotational energy. They are in equipartition with the free rotational energy (35OC-Rs-3d) or surpass it by one order of magnitude. Hence, the ratio $\mathcal{B}/\mathcal{F}$ is larger than in 2D. The surface field strength slightly exceeds $b_{surf} \gtrsim 10^{14}$ G during most of the evolution with only the poloidal component of model 35OC-RO-3d falling short of this value by a factor of ≈ 3. In model 35OC-Rs-3d, on the other hand, both components develop the same strength.

The structure of the PNSs, visualized for late times in Fig. 21, is characterized by a high degree of rotational flattening (cf. the isodensity surface in the two panels). Deviations from an axisymmetric

shape are minor. The PNS surface shows a strong differential rotation between the equatorial bulge rotating at sub-kHz frequencies and much faster rotation at higher latitudes. The magnetic field, strongest near the polar axis, forms a helix around the $z-$axis. Close to the PNS, the field widens more in model 35OC-Rs-3d than in 35OC-RO-3d.

The results indicate that the structure of the PNS as well as its magnetic field are sufficiently similar to the axisymmetric versions of the two models for the 3D models to be possible GRB progenitors. The dimensionality may, however, have an influence on the threshold separating collapsars from PMCs, as suggested by the cessation of the growth of the PNS mass in model 35OC-RO-3d in contrast to the monotonic increase of M_{PNS} in axisymmetry.

6 DISCUSSION AND CONCLUSIONS

We followed the post-collapse, long-term evolution of the cores of several rotating and magnetized stars with zero-age main-sequence mass $M_{ZAMS} = 35 \, M_{\odot}$ and subsolar metallicities. Our main goal is to asses the robustness of the predictions stating that these models may form a collapsar or any other type of possible central engine of long GRBs. In particular, we aim at assessing the variance of the possible outcomes resulting from relatively small changes in the magnetic field strength and topology of the pre-collapse star, as well as on modifications of the rotational profile. Given the uncertainties still existing in (1D) stellar evolution, predicting whether a given massive, compact core may yield a BH after its gravitational collapse is still adventurous (but see the notable advances in cases where rotation and magnetic fields are less important, e.g. Ugliano et al. 2012; Sukhbold et al. 2016; Ertl et al. 2020; Woosley et al. 2020, employing a 1D approach). We point out that, specifically, the topology of the magnetic field in the mapping from 1D to multiple dimensions is not unanimously defined. Hence, variations in the ratio of poloidal to toroidal magnetic field components may be a source of variance in multidimensional initial models, since the 1D stellar progenitors only provide the toroidal and radial magnetic field components (see Appendix A). Due to the much larger computational costs of multidimensional models (compared to 1D models), we cannot explore systematically the influence of the stellar progenitor properties on the final outcomes. Instead, we have restricted to a couple of high-mass, low-metallicity cores, and considered what variations of the magnetic field and rotational profile produce BHs or PNSs as compact remnants. We have performed multidimensional (mostly 2D, but also some preliminary 3D) simulations coupling special-relativistic MHD with a neutrino-transport scheme based on the two-moment formulation of the spectral transport equation (see Paper I, section 2). Our initial cores (i.e. the progenitor stars) map into 2D or 3D the 1D stellar evolution models 35OC and 35OB of Woosley & Heger (2006), which explicitly include rotation and magnetic fields, although in a spherical approximation. They are, therefore, a subset of the stellar progenitors considered in Paper I. These models have been considered as a potential progenitors of long GRBs, due to the possibility of forming a collapsar engine, since their Kerr parameter is $a > 0.3$ at $3 \, M_{\odot}$ and the angular momentum increases outwards (Woosley & Heger 2006).

The high mass and fairly large compactness of our initial models (O'Connor & Ott 2011) cause their evolution after core bounce to transit along a borderline between producing either a BH or a PNS, with a broad range of intermediate possibilities in which the PNS dodges its collapse to a BH for a (very) long time. This final fate does naturally depend on the ability to minimize the post-bounce mass accretion rate and, hence, on the complex interplay of

the explosion dynamics and the compact remnant. Ultimately, the possible evolutionary paths depend on variations in the pre-collapse cores.

We performed eleven simulations: nine versions of core 35OC, and two of core 35OB. Most simulations used the original rotational profile of the stellar-evolution calculations, but a few control models were run with decreased and increased angular velocities. Some of the simulations of each core were run with the original magnetic field, others with an artificial magnetic field of mixed poloidal-toroidal topology and different normalization. All simulations were run until the cores collapsed to a BH or, if failing to do so, for various seconds post-bounce; in a couple of models for more than ~ 8 s. Our main results can be summarized as follows.

6.1 The key role of the pre-SN poloidal magnetic field

The strength and spatial smoothness of the poloidal field is decisive to determine the lifetime of the PNS post-bounce. Two-dimensional models run with the original progenitor magnetic field, e.g. 35OC-RO and 35OB-RO, produce BHs within less than~ 3.3 s after core collapse. The 3D version of the former has not been evolved for a sufficiently long time to confirm this possibility. However, its smaller mass growth rate after ~ 0.4 s compared to the 2D version of the core 35OC-RO suggests that BH collapse may take even longer for this model in 3D (see Paper I). Compared to the toroidal component, the original stellar progenitor includes a relatively weak poloidal field. A small change of a factor of 2 of the poloidal field strength in the pre-SN iron core while maintaining the same toroidal field suffices to halt the growth of the PNS mass, significantly delaying, if not completely preventing BH formation in the series of models with supra-stellar magnetic fields (models 35OC-Rp2, 35OC-Rp3, and 35OC-Rp4). We stress that this small change in the poloidal field in axial symmetry brings a negligible increase of the magnetic energy of the initial model. Our goal is not to find in this paper an extremely accurate magnetic field strength and topology which changes the fate of the original stellar progenitor, eventually producing a PM instead of a BH and (likely) a collapsar. There are (at least) two reasons for that. First, the very same mapping from the 1D stellar evolution model to our multidimensional grids introduces variations in the post-bounce evolution, which may significantly change the lifetime of the PNS. Secondly, in 3D the aforementioned value may be changed quantitatively and, hence, it does not pay off to explore with great accuracy the threshold dividing the formation of a PM from a collapsar. In a future work, we will explore additional models for longer post-bounce times in 3D to check our findings in axial symmetry. Besides, we have not found a monotonic trend stating that larger initial poloidal magnetic field guarantees the avoidance of BH formation. While the possibility of dodging BH formation seems evident in models 35OC-Rp2 and in 35OC-Rs, the fate fo model 35OC-Rp3 (with an initial poloidal field in between of the former cases) is not clear. Its late time ($\gtrsim 7$ s) increase of the accretion rate above $\dot{M}_{\mathrm{PNS}} \sim 0.1 \, \mathrm{M}_{\odot} \, \mathrm{s}^{-1}$ may let it collapse to a BH within the next couple of seconds (after the $t_{\mathrm{pb}} \simeq 9$ s of computed evolution). However, attending to the non-monotonic evolution of the PNS in our models (especially regarding the PNS mass in PMCs), a precise forecast of the fate of model 35OC-Rp3 is not possible.

6.2 Variations in the magnetic topology

The topology of the magnetic field is more important than the strength of the field in determining the evolutionary path of our models. Comparing the case in which we double the strength of the magnetic

field (multiplying by 2 both the -dominant- toroidal and poloidal components; model 35OC-RO2) with the case in which we double the strength of the poloidal field (35OC-Rp2), the former model forms a BH, while the latter staves off it. Since the main difference between the model with the original magnetic field and rotation (35OC-RO) and model 35OC-RO2 is the twice larger toroidal magnetic field in the latter, we conclude that a moderate increase of the toroidal magnetic field in the progenitor star does not alter the prospects for BH formation. In line with the results of Bugli et al. (2020), dipolar configurations tend to produce more collimated explosion ejecta and more oblate PNSs. Episodes of PNS spin-down (several seconds after bounce) tend to reduce the ellipticity of the models, increasing the polar-to-equatorial radius ratio. Indeed, the model with the largest, purely dipolar magnetic field (model 35OC-Rs) eventually undergoes a morphological transition from a revolution ellipsoid to a toroid, with a maximum density off-centre for $t_{\mathrm{pb}} \gtrsim 2.5$ s. It remains to be confirmed that a similar morphology may be attained by the 3D version of this model (which has, so far, been run up to $t_{\mathrm{pb}} \simeq 1.2$ s).

6.3 Variations in the rotational profile

For the pre-SN core 35OC (35OB), increasing the rotational rate by a factor of 1.50 (2) and, at the same time, reducing significantly the magnetic field strength does not prevent BH formation. Models with supra-stellar rotation tend to form centrifugally supported, toroidally shaped structures around the central PNS. These structures may survive to BH collapse for a few seconds by virtue of their larger specific angular momentum ($j > 1.5 \times 10^{16} \, \mathrm{cm}^2 \, \mathrm{s}^{-1}$; see below). This finding contrast with the expectations of Dessart et al. (2008), who argued that stars with large angular momentum in the core may not transition to a BH. These authors suggest that fast-rotating cores lead to magnetically driven, baryon-loaded, non-relativistic jets without any GRB signature. Although we have only tested two progenitors of the same ZAMS mass, our results hint towards a more intricate interplay between the rotational structure and the magnetic field dynamics, which hinders an unequivocal prediction of the high-energy signatures our models. In line with the expectations, a reduction of the rotational rate of the pre-SN core 35OC (model 35OC-Sw) facilitates an early BH formation ($t_{\mathrm{pb}} \lesssim 1.5$ s).

M11 suggest that there is a division between magnetorotationally and neutrino-powered SNe on the basis of the ratio between the envelope binding energy, E^{bd}, and the rotational energy of the PNS $\mathcal{T}^{\mathrm{PNS}}$. While $|E^{\mathrm{bd}}|/\mathcal{T}^{\mathrm{PNS}} > 1$ would lead to magnetorotational explosions, the complementary case, $|E^{\mathrm{bd}}|/\mathcal{T}^{\mathrm{PNS}} < 1$, may produce neutrino-driven SNe (see their fig. 1). This basic division does not account for the role of the magnetic fields except in a parametrized way (assuming that the magnetic energy is some fraction of the core rotational energy). The growth of magnetic fields partly happens at the expense of the rotational energy (mostly) of the pre-SN core, but it is also driven by vigorous convection in a bunch of our models, especially in PMCs (see below). Besides, $\mathcal{T}^{\mathrm{PNS}}$ is a time-evolving quantity in the collapsed core (Fig. 2c), while E^{bd} changes very moderately (within a factor of 2) throughout the post-bounce evolution. Interestingly, the ratio $|E^{\mathrm{bd}}|/\mathcal{T}^{\mathrm{PNS}}$ tends to decrease with time after bounce for BH-forming models (since $\mathcal{T}^{\mathrm{PNS}}$ grows for most of them, while E^{bd} decreases slightly). The reduction of $|E^{\mathrm{bd}}|/\mathcal{T}^{\mathrm{PNS}}$ tends to be less pronounced (or much shallower) for PMCs. We also observe exceptions to the basic scheme of M11. For instance, models 35OC-RRw and 35OB-RRw have both four times more rotational energy than the corresponding stellar evolution models 35OC-RO and 35OB-RO, respectively. All these models (35OC-RO,

350B-RO, 350C-RRw, and 350B-RRw) develop values $|E^{\text{bd}}|/\mathcal{T}^{\text{PNS}} \ll 1$ in the post-bounce evolution. In contrast to the latter models, the former ones produce either a neutrino driven explosion aided by rotational effects or a mixed type explosion, which is not clearly magnetorotationaly driven (see Table 1).

6.4 Angular momentum transport

Many of our models develop strong enough magnetic fields, which enable angular momentum transport from the inner regions of the PNS towards its surface, where it accumulates. There, high specific angular momentum matter forms extended toroidal structures with a low electron fraction. These neutron-rich regions are only loosely bound and may be dragged along the bipolar outflows that most models develop. Hence, the formation of *r*-process nuclei is an interesting possibility that is currently under investigation (Reichert et al. 2020). We cautiously suggest that some GRB precursor activity might be observed in connection to the accretion of these high-*j* layers in BH-forming cases. They may be accreted a few seconds before the definitive accretion disc forms (and hence fuels the outflow). The aforementioned transport does not slow down the PNS globally, because it does not reach the surrounding region, and the angular momentum remains in the envelope of the PNS. As a consequence, these layers expand, raising the axial ratio of the PNS.

6.5 Hypermassive NSs

Temporarily stable PNSs of high mass are formed by all our models. We find it significant that the β_{G} ratio (equation 3) maintains values smaller than ~ 3 per cent for the longest run models. These low values of β_{G} may not allow for the development of dynamical instabilities inducing collapse to BH. The 3D models, we have run appear to confirm these small values of β_{G}, albeit, so far, on a relatively short period of evolution after stellar core collapse. We find that PMCs systematically posses smaller values of β_{G} than PCs, which enhances their prospects to not collapse to BHs relatively soon after bounce, since PMCs may be less perturbed by the 'low-β_{G}' instability. As established in Paper I, and confirmed here with much longer evolutions post-bounce, the mass of the PNSs formed by our models are of the order of or larger than the masses of the iron core of the respective pre-SN model. This means that in case these PNSs do not collapse further to a BH (due to, e.g. prolonged episodes of late fall-back accretion on time-scales of hours), very heavy neutron stars (with masses $1.85 \lesssim M \lesssim 2.5\,\text{M}_\odot$) may result. These masses, especially the ones closer to the maximum mass allowed by the EoS in the absence of rotation are only marginally consistent with the current observational limits (Özel & Freire 2016), and, in any case, they would belong to the ~ 20 per cent fraction of the population of *massive* NSs (with $M > 1.8\,\text{M}_\odot$; Antoniadis et al. 2016). We would need to compute a much longer time-evolution (of minutes to hours) in order to ascertain the kind of NS that will finally develop from our models. The reason is that we cannot reliably know what fraction of the outer layers will be blown away by the very aspherical SN explosions that our models trigger and, consistently, which fraction may be accreted on to the PNS. Besides, not all the matter hitting the PNS surface will finally end up adding to its mass and angular momentum. During the computed time of evolution, a large fraction of it drifts from low to high latitudes to be incorporated to the outflow ejecta. Furthermore, the non-monotonic increase in the mass and other properties of the PNS (e.g. their magnetic energy and angular momentum as well as the surface magnetic fields) makes it difficult to extrapolate the properties of our massive PNSs on time-scales of hours. We note that this situation departs significantly from the evolution of non-rotating, unmagnetized cores, where relatively simple prescriptions for the mass evolution can be given and, hence, a solid extrapolation of the properties of NS at birth can be done (e.g. Woosley et al. 2020, for a recent example). It seems, however, difficult that the accretion of a few $0.01\,\text{M}_\odot$ may bury the magnetic fields already built at the end of their computed evolution, with values $b_{\text{surf}}^{\text{pol}}$ larger than 10^{14} G in our models with long-lasting PNSs (cautiously extrapolating the results of Torres-Forné et al. 2016). Thus, magnetar field strengths are expected in our high-mass PMCs. The rotational period is difficult to predict as a result of the alternation of spin-down and spin-up periods. By the end of our most evolved models (more than 7.5 s after core bounce), surface periods of $\sim 1.5 - 4$ ms and polar (equatorial) radii of $\sim 14 - 17$ km ($\sim 20 - 30$ km) are observed. Interestingly, these radii, which trace the location of the PNS neutrinosphere, tend to be larger than the radius of an equivalent spherical and homogeneous configuration with the same mass and moment of inertia than the PNS, with typical values $R_{\text{PNS},1} \simeq 12 - 14$ km at the end of the computed evolution. The difference between these two radii is accounted for by the layer of high specific angular momentum and relatively low-density surrounding the PNS that forms as a result of angular momentum transport (see above). Thus, we find it difficult to include the outcome of our PMCs within existing NS categories, but we tentatively classify them as *super-magnetars* (e.g. Rea et al. 2015). Because of the uncertainties in the mass estimations obtained in compact binary millisecond pulsars (black-widows and redbacks), they have not been included in most global studies of the NS mass distribution (Linares 2019). However, *supermassive* NSs, with more than $2\text{M}_\odot$ have been found in these systems (e.g. $2.3\,\text{M}_\odot$ in PSR J2215 + 5135, Linares, Shahbaz & Casares 2018; or $2.4\,\text{M}_\odot$ in PSR B1957 + 20, van Kerkwijk, Breton & Kulkarni 2011). Although our progenitors are single stars (not binaries), our results suggest a channel to produce supermassive NS also from isolated progenitors.

6.6 Magnetic field amplification

The strongly differentially rotating cores fulfil the criterion for the MRI in wide regions, both inside and outside the neutrinosphere. We are able to identify episodic growth of the MRI in various BH-forming models. For instance, we were able to resolve the growth of the instability in the simulation of core 350C with the original rotational profile and magnetic field. MRI channel modes grow in a single episode at about 150 ms post-bounce, most prominently just inside the PNS surface, yielding an increase of the energy of the poloidal field by a factor of a few. In contrast, NS forming models obtain their large magnetic fields chiefly as a result of the vigorous convection in their fast-rotating PNSs, not because of MRI. This is because the Rossby number inside the PNS is smaller than 1 in large regions. Contrasting with the very moderate growth that convection produces in non-rotating, magnetized models, in our fast-rotating models, it yields large amplification factors of ~ 1000, even larger than the theoretical expectations of Duncan & Thompson (1992).

6.7 Spin of the formed BHs

In general, all PNS possess fairly rapid rotation. The dimensionless spin parameter is $\sim 0.3 - 0.5$ for models with the rotational profile from stellar evolution. These values turn out to be very similar to the formal values computed from the mass and angular momentum of the inner $3\text{M}_\odot$ of the progenitor (Woosley & Heger 2006). The similarity between our measured a_{PNS} and the formal values happens in spite

of the complex accretion/ejection dynamics, which imprints a non-monotonic evolution of a_{PNS}. Furthermore, models with relatively mild increases in the magnetic field strength (in particular model 35OC-Rp2) yield significantly smaller values of a_{PNS} and no BH results in these cases. With the aforementioned values of the spin parameter, and noting that the strength of the magnetic field at the PNS surface in PCs is $\sim 7 \times 10^{14}$ G the *initial* Blandford–Znajek luminosity of a potential long GRB collapsar will be rather mild $\sim 8 \times 10^{49}(a_{PNS}/0.4)^2(M_{BH}/3\,M_\odot)^2(B/7 \times 10^{14}\,\text{G})^2$ erg s^{-1} (using the estimates of Mahlmann, Cerdá-Durán & Aloy 2018, and assuming that the spin of the BH coincides with the spin of the PNS at the brink of collapse). This relatively small value may be increased as the BH mass and spin increase due to the ongoing accretion.

6.8 Formation of collapsars

Among the models that undergo BH collapse, highly anisotropic explosions allow for continuing accretion increasing the PNS mass beyond the instability threshold. Collapse occurs after more than a second post-bounce. However, the exact time when this happens is sensitive to the choice of equation of state (e.g. Fischer et al. 2011; O'Connor & Ott 2011; Aloy et al. 2019, and references therein) and, in our case, to the approximate treatment of the general relativistic gravitational field. The ram-pressure of the explosion ejecta makes the fall of the stellar layers outside the central core happen on time-scales longer than the simple estimate for the disc formation time as twice the free-fall time (equation 1; $t_{DF} \sim 9.3$ s for the 35OC core). The practical consequence of this fact is that the mildly relativistic, collimated SN ejecta may break out of the stellar surface sooner than or at about the same time as the accretion disc forms around the central BH. Extrapolating their results, Dessart et al. (2008) suggest that these ejecta may yield a weak precursor polar jet, which may soon be overtaken by a baryon-free, collimated relativistic jet (see also Aloy et al. 2018). We basically agree with that forecast in case of BH-forming models, but in case of PMCs the scenario may be different (see below).

Since our models that may potentially form a collapsar are computed to the brink of BH formation, we cannot give a precise time after core bounce when collapsar formation may take place and, strictly speaking, whether a collapsar (understood as a BH girded by a suitable accretion disc) may form. The ongoing, quite energetic explosion (see Paper I) makes it difficult to estimate the amount of mass that may be available for accretion in the mid-term and, indeed, whether an accretion disc with the properties required by typical collapsar models (e.g. MacFadyen et al. 2001) may form at all. Our results suggest that it may not be strictly necessary to form an accretion disc in order to produce an ultrarelativistic jet. Once the BH is formed, a fraction of its rotational energy may be extracted by means of the Blandford–Znajek mechanism with luminosities broadly compatible with those of long GRBs (see above). There is no need of forming an accretion disc if down-flows keep going on along the equatorial regions (extrapolating the conditions at the brink of BH collapse in our models), even if the magnetic field is relatively disordered and clumps into relatively small-scale structures (see, e.g. Mahlmann, Levinson & Aloy 2020). If this possibility could materialize, it would open the prospects for a number of other stellar evolution models to be considered as potential progenitors of long GRBs.

The kind of collapsars that our models may form cannot be classified in any of the types defined by MacFadyen et al. (2001). The models that produce BHs relatively promptly yield also successful SN explosions, which disqualifies them as Type I collapsars. Besides,

if any of the models with supra-stellar magnetic fields would finally yield a BH by late-time, fall-back accretion, still the magnetorotational explosions produced are very energetic (with energies in the hypernova range; see Paper I). This could be the case of model 35OC-Rp3 (see above) or models with supra-stellar poloidal field in between of model 35OC-RO and 35OC-Rp2. Assuming that these models were able to form a collapsar (namely, by assembling an accretion disc around the new born BH), the expected explosion energy does not allow to classify them as Type II collapsars. The argument of MacFadyen et al. (2001), according to which more massive helium cores may fail to eject all matter outside the neutron star does not apply here. Even if it is true that the gravitational binding energy of the helium core increases with mass roughly quadratically, our magnetorotational explosions produce very collimated ejecta, which prevent their failure (as it would likely be the case under more isotropic explosion types). Given the different explosion properties of our models which do not collapse promptly to BH, we suggest a possible third type of collapsars (Type III) produced in the remnant of magnetorotational explosions, tens of seconds after core collapse. In these models, the progenitor envelope may be exploded by a combination of a disc wind and magnetorotational stresses, resulting in a hypernova-like SN with potentially large luminosity if the amount of ^{56}Ni mass produced in the disc wind is large enough (as suggested by e.g. Nagataki et al. 2007; Dessart et al. 2008).

6.9 Formation of PMs

Some of the models which do not form a BH promptly seem promising for PM-driven SNe and GRBs. The pre-SN models that may originate PMCs combine the high rotational energy available in the iron core and magnetic fields (a bit) stronger than in the original stellar evolution model. PMCs posses a PNS angular momentum significantly smaller ($J_{PNS} \lesssim 2 \times 10^{49}$ g cm^2 s^{-1}) than BH-forming models. In PMCs, BH collapse is prevented by very strong outflows that manage to suppress mass accretion or even turn it into mass ejection, with a significant loss of mass of the PNS. A decreasing PNS mass has been found in previous papers (e.g. Dessart et al. 2008; Obergaulinger & Aloy 2017), but here, owing to the very long evolutionary times computed, we find various episodic phases of mass decrease interleaved with a moderate PNS mass growth. The angular momentum of the PNS parallels the evolution of its mass, showing episodes of spin-down alternating with spin-up phases. This non-monotonic evolution shows that not only the journey to BH formation is arduous in potential GRB progenitors (Dessart et al. 2012), but also the path to PM formation is tortuous. In model 35OC-Rs with a modified magnetic field of dipolar topology, we also observe a decrease of the mass, of the rotational energy, and of the angular momentum of the PNS during the first second post-bounce. As in the case of models with supra-stellar poloidal magnetic field, the energy-momentum and mass lost end up in the jet-like outflows. While those are not highly relativistic yet, we consider this model also a potential PM central engine in its earliest stage. As BH-forming models, PMCs may launch magnetorotationally powered jets. Initially, these jets are quite baryon loaded and only mildly relativistic, but as time goes by the PM wind becomes progressively more relativistic and baryon-free. Furthermore, the PM wind has a predominantly radial geometry close to the PNS, which turns into a paraboloidally shaped one after several hundred kilometres, where it enters the highly collimated cavity blown by the ongoing SN shock. Hence, it is not unlikely that there is a relatively smooth transition from a mildly relativistic precursor ejecta to a relativistic jet (in the spirit of the model of M11). As in the case of

BH-forming models, a disc wind may produce the required amounts of ^{56}Ni to accompany the GRB jet with a luminous SN event. While a detailed analysis of the nucleosynthesis of our models will be the subject of a subsequent publication, we note that the explosion energies, ejecta masses, and the thermodynamic conditions of the ejecta are broadly compatible with the production of considerable Ni masses.

In spite of the long time evolution span by our axisymmetric models (nearly 10 s), they have not fully entered the KH phase, since accretion and convection are still on-going. This result is in strong contrast with the standard assumptions that place the beginning of the *quasy-stationary* phase a few hundred milliseconds after core collapse (e.g. Pons et al. 1999; Hüdepohl et al. 2010), and for models aiming to bridge from the post-bounce phase to the KH phase (e.g. Martinon et al. 2014). We cautiously note that our results need further validation with full-fledged 3D models.

6.10 PM spin-down

Our models with supra-stellar poloidal magnetic fields as well as model 35OC-Rs, if run long enough, display episodes of PNS spin-down. Confirming that we have not fully entered the KH phase and that the evolution remains highly dynamic for nearly 10 s after collapse (remarkably in the case of model 35OC-Rp3), we have not found a steady PM spin-down. However, it is reassuring that many quantitative and qualitative facets of our results are similar to the predictions of the PM model of M11 during the episodic spin-down phases. It is, however, necessary to consider even longer evolutions to sort out whether our most promising PMCs may generate a PM after a longer evolution. Whether or not the evolution does indeed confirm this possibility depends on additional factors eluding inclusion into an approximate model like the one of M11, such as the geometry and efficiency of ejection of matter necessary for evacuating the surroundings of the PNS and thereby reducing the baryon-loading of the potential GRB jet.

The magnetic breaking of the compact remnant is linked to the increased coupling between the magnetorotational evolution of the core and the surrounding envelope. As could be expected, the core-envelope coupling is more effective if large-scale poloidal magnetic fields are present in the pre-collapsing core. However, even without *artificial* large-scale poloidal fields, the PNS spins down in the long term by the ejection of magnetized winds from its surface. We observe that during the periods of spin-down the Alfvén surface moves a few hundred kilometres away from the rotational axis, facilitating the transport of angular momentum towards the surroundings of the PNS. Additional effects carrying away angular momentum such as neutrino emission or magnetorotational dynamical instabilities (though in our axisymmetric simulations they may not be relevant) carrying away angular momentum seem subdominant in our models. Spin down time-scales as short as $|\tau_{\rm rot}| = \mathcal{T}^{\rm PNS}/|\dot{\mathcal{T}}^{\rm PNS}| \sim 2-3$ s or, equivalently, $P/|\dot{P}| \sim 1-1.5$ s are typical during the late, more than ~ 2 s long spin-down phase of model 35OC-Rp2. These $P/|\dot{P}|$ time-scales may not be maintained for too long as they quickly rise to $\tau_{\rm rot} \lesssim 20$ s towards the end of the computed time for model 35OC-Rp2. As with other quantities, it is difficult to make a forecast for the value of $P/|\dot{P}|$ at NS birth, but a (simplistic) extrapolation of our results hints towards $P/|\dot{P}| \sim$ few $\times\, 100$ s at about $t \sim 10$ s post-bounce. According to the model of Metzger et al. (2018), with these spin-down time-scales and surface poloidal magnetic fields $\sim 10^{15}$ G, a long GRB, but unlikely an ultra-long GRB (with durations $\gtrsim 10^3$ s; e.g. Gendre et al. 2013; Levan et al. 2014), can be produced unless the evolution changes significantly. An order

of magnitude longer spin-down time-scales, $|\tau_{\rm rot}| \sim 10-40$ s, and smaller surface magnetic field strengths, $b_{\rm surf}^{\rm pol} \lesssim 10^{14}$ G, are found in other potential PMCs differing by less than 50 per cent in the initial poloidal field (e.g. model 35OC-Rp3). This remarkable variation of the spin-down time-scale with the initial poloidal field strength opens up the possibility that long GRBs with very different durations may result from relatively small variations in the properties of the pre-SN star. The episodic nature of the spin-down periods computed in our models suggests that the subrelativistic ejecta can be quite heterogeneous both in the radial and polar directions. The propagation of a relativistic jet on these heterogeneous environment is a source of variability that will be blended with that imprinted by, e.g. the development of instabilities during the crossing of the stellar envelope (Aloy et al. 2002; Morsony et al. 2010; Bromberg & Tchekhovskoy 2016; Aloy et al. 2018).

As we have commented in Paper I of this series, the main limitation of the present study is that most of our models are axisymmetric. The amplification of magnetic fields, the dynamics of the explosion, and the development of several instabilities can be quite different in 3D geometry (see Paper I). In order to partly cross-check some of the conclusions drawn on the basis of axisymmetric models, we have also presented preliminary results of 3D simulations with reduced grid resolution. These 3D models show outflows that develop similarly to the axisymmetric versions of the same models and thus seem to alleviate the concerns, but some caution remains appropriate before drawing overarching conclusions from the so far limited number of models. Hence, our efforts for improving upon this work should concentrate on simulating models in full 3D geometry, for which we are planning to address selected issues in different stages of the evolution.

From our results, we can draw the conclusion that high-mass stars offer a very wide range of potential post-collapse dynamics. Furthermore, strong rotation favours the development of possible GRB engines. As a consequence, we consider most models promising candidates for GRB engines in the long run after the end of our simulations. While our models do not cover the available parameter space comprehensively, a collapsar scenario seems as viable as a PM engine because the path to a PM is mostly dependant on relatively small variations of the poloidal magnetic field in the pre-SN core. The large variability observed in many of the variables after collapse (singularly, the spin period, the mass and the rotational energy) of the accreting PNS justifies our method for pushing as long as possible the computed post-bounce evolution and encourages us continuing pushing further in time our study in the future.

DATA AVAILABILITY

The data underlying this article will be shared on a reasonable request to the corresponding authors.

REFERENCES

Aguilera-Dena D. R., Langer N., Moriya T. J., Schootemeijer A., 2018, ApJ, 858, 115

Akiyama S., Wheeler J. C., Meier D. L., Lichtenstadt I., 2003, ApJ, 584, 954

Aloy M. A., Müller E., Ibáñez J. M., Martí J. M., MacFadyen A., 2000, ApJ, 531, L119

Aloy M., Ibáñez J., Miralles J., Urpin V., 2002, A&A, 396, 693

Aloy M. A., Cuesta-Martínez C., Obergaulinger M., 2018, MNRAS, 478, 3576

Aloy M. A., Ibáñez J. M., Sanchis-Gual N., Obergaulinger M., Font J. A., Serna S., Marquina A., 2019, MNRAS, 484, 4980

Andersson N., 2003, Class. and Quantum Gravity, 20, R105

Antoniadis J., Tauris T. M., Ozel F., Barr E., Champion D. J., Freire P. C. C., 2016, preprint (arXiv:1605.01665)

Balbus S. A., Hawley J. F., 1998, Rev. Mod. Phys., 70, 1

Bardeen J. M., Press W. H., Teukolsky S. A., 1972, ApJ, 178, 347

Barkov M. V., Komissarov S. S., 2008, MNRAS, 385, L28

Batta A., Lee W. H., 2016, MNRAS, 459, 2140

Bisnovatyi-Kogan G. S., Popov I. P., Samokhin A. A., 1976, Ap&SS, 41, 287

Bromberg O., Tchekhovskoy A., 2016, MNRAS, 456, 1739

Bruenn S. W. et al., 2016, ApJ, 818, 123

Bucciantini N., Quataert E., Arons J., Metzger B. D., Thompson T. A., 2007, MNRAS, 380, 1541

Bucciantini N., Quataert E., Arons J., Metzger B. D., Thompson T. A., 2008, MNRAS, 383, L25

Bucciantini N., Quataert E., Metzger B. D., Thompson T. A., Arons J., Del Zanna L., 2009, MNRAS, 396, 2038

Bucciantini N., Metzger B. D., Thompson T. A., Quataert E., 2012, MNRAS, 419, 1537

Bugli M., Guilet J., Obergaulinger M., Cerdá-Durán P., Aloy M. A., 2020, MNRAS, 492, 58

Burrows A., 1988, ApJ, 334, 891

Burrows A., Goshy J., 1993, ApJ, 416, L75

Burrows A., Dessart L., Livne E., Ott C. D., Murphy J., 2007, ApJ, 664, 416

Camarda K. D., Anninos P., Fragile P. C., Font J. A., 2009, ApJ, 707, 1610

Centrella J. M., New K. C. B., Lowe L. L., Brown J. D., 2001, ApJ, 550, L193

Chandrasekhar S., Fermi E., 1953, ApJ, 118, 116

Cuesta-Martínez C., Aloy M. A., Mimica P., Thöne C., de Ugarte Postigo A., 2015a, MNRAS, 446, 1737

Cuesta-Martínez C., Aloy M. A., Mimica P., 2015b, MNRAS, 446, 1716

Dessart L., Burrows A., Livne E., Ott C. D., 2007, ApJ, 669, 585

Dessart L., Burrows A., Livne E., Ott C. D., 2008, ApJ, 673, L43

Dessart L., O'Connor E., Ott C. D., 2012, ApJ, 754, 76

Donati J. F., Babel J., Harries T. J., Howarth I. D., Petit P., Semel M., 2002, MNRAS, 333, 55

Donati J. F., Howarth I. D., Bouret J. C., Petit P., Catala C., Landstreet J., 2006, MNRAS, 365, L6

Duncan R. C., Thompson C., 1992, ApJ, 392, L9

Ekström S. et al., 2012, A&A, 537, A146

Ertl T., Woosley S. E., Sukhbold T., Janka H. T., 2020, ApJ, 890, 51

Fischer T. et al., 2011, ApJS, 194, 39

Franci L., De Pietri R., Dionysopoulou K., Rezzolla L., 2013, Phys. Rev. D, 88, 104028

Fryer C. L., Heger A., 2000, ApJ, 541, 1033

Fryer C. L., Warren M. S., 2004, ApJ, 601, 391

Fujisawa K., 2015, MNRAS, 450, 4016

Gendre B. et al., 2013, ApJ, 766, 30

Giannios D., Mimica P., Aloy M. A., 2008, A&A, 478, 747

Guilet J., Müller E., Janka H.-T., 2015, MNRAS, 447, 3992

Harikae S., Takiwaki T., Kotake K., 2009, ApJ, 704, 354

Heger A., Langer N., Woosley S. E., 2000, ApJ, 528, 368

Heger A., Woosley S. E., Spruit H. C., 2005, ApJ, 626, 350

Hüdepohl L., Müller B., Janka H.-T., Marek A., Raffelt G. G., 2010, Phys. Rev. Lett., 104, 251101

Ito H., Matsumoto J., Nagataki S., Warren D. C., Barkov M. V., 2015, ApJ, 814, L29

Janka H., 2004, in Camilo F., Gaensler B. M., eds, Proc. IAU Symp. Vol. 218, Neutron Star Formation and Birth Properties. Kluwer, Dordrecht, p. 3

Janka H.-T., 2012, Ann. Rev. Nucl. Part. Sci., 62, 407

Just O., Obergaulinger M., Janka H.-T., 2015, MNRAS, 453, 3386

Keszthelyi Z., Meynet G., Georgy C., Wade G. A., Petit V., David-Uraz A., 2019, MNRAS, 485, 5843

Kotake K., Sawai H., Yamada S., Sato K., 2004, ApJ, 608, 391

Kumar P., Zhang B., 2015, Phys. Rep., 561, 1

Kuroda T., Arcones A., Takiwaki T., Kotake K., 2020, ApJ, 896, 102

Lattimer J. M., Prakash M., 2001, ApJ, 550, 426

Lattimer J. M., Schutz B. F., 2005, ApJ, 629, 979

Lazzati D., Morsony B. J., Margutti R., Begelman M. C., 2013, ApJ, 765, 103

Lee W. H., Ramirez-Ruiz E., 2006, ApJ, 641, 961

Levan A. J. et al., 2014, ApJ, 781, 13

Linares M., 2019, preprint (arXiv:1910.09572)

Linares M., Shahbaz T., Casares J., 2018, ApJ, 859, 54

López-Cámara D., Morsony B. J., Begelman M. C., Lazzati D., 2013, ApJ, 767, 19

López-Cámara D., Morsony B. J., Lazzati D., 2014, MNRAS, 442, 2202

López-Cámara D., Lazzati D., Morsony B. J., 2016, ApJ, 826, 180

MacFadyen A. I., Woosley S. E., 1999, ApJ, 524, 262

MacFadyen A. I., Woosley S. E., Heger A., 2001, ApJ, 550, 410

Maeder A., Meynet G., 2012, Rev. Mod. Phys., 84, 25

Mahlmann J. F., Cerdá-Durán P., Aloy M. A., 2018, MNRAS, 477, 3927

Mahlmann J. F., Levinson A., Aloy M. A., 2020, MNRAS, 494, 4203

Marek A., Dimmelmeier H., Janka H.-T., Müller E., Buras R., 2006, A&A, 445, 273

Margalit B., Metzger B. D., Thompson T. A., Nicholl M., Sukhbold T., 2018, MNRAS, 475, 2659

Martinon G., Maselli A., Gualtieri L., Ferrari V., 2014, Phys. Rev. D, 90, 064026

Masada Y., Takiwaki T., Kotake K., Sano T., 2012, ApJ, 759, 110

Meier D. L., Epstein R. I., Arnett W. D., Schramm D. N., 1976, ApJ, 204, 869

Metzger B. D., Thompson T. A., Quataert E., 2007, ApJ, 659, 561

Metzger B. D., Giannios D., Thompson T. A., Bucciantini N., Quataert E., 2011, MNRAS, 413, 2031 (M11)

Metzger B. D., Margalit B., Kasen D., Quataert E., 2015, MNRAS, 454, 3311

Metzger B. D., Beniamini P., Giannios D., 2018, ApJ, 857, 95

Meynet G., Maeder A., 2007, A&A, 464, L11

Mimica P., Giannios D., Aloy M. A., 2009, A&A, 494, 879

Mizuta A., Aloy M. A., 2009, ApJ, 699, 1261

Mizuta A., Yamasaki T., Nagataki S., Mineshige S., 2006, ApJ, 651, 960

Moiseenko S. G., Bisnovatyi-Kogan G. S., Ardeljan N. V., 2006, MNRAS, 370, 501

Morsony B. J., Lazzati D., Begelman M. C., 2007, ApJ, 665, 569

Morsony B. J., Lazzati D., Begelman M. C., 2010, ApJ, 723, 267

Mösta P. et al., 2014, ApJ, 785, L29

Mösta P., Ott C. D., Radice D., Roberts L. F., Schnetter E., Haas R., 2015, Nature, 528, 376

Muhlberger C. D. et al., 2014, Phys. Rev. D, 90, 104014

Nagakura H., 2013, ApJ, 764, 139

Nagakura H., Ito H., Kiuchi K., Yamada S., 2011, ApJ, 731, 80

Nagataki S., Takahashi R., Mizuta A., Takiwaki T., 2007, ApJ, 659, 512

Nakamura K., Takiwaki T., Kuroda T., Kotake K., 2015, PASJ, 67, 107

O'Connor E., Ott C. D., 2011, ApJ, 730, 70

Obergaulinger M., Aloy M. Á., 2017, MNRAS, 469, L43

Obergaulinger M., Aloy M. Á., 2020a, MNRAS, 492, 4613 (Paper I)

Obergaulinger M., Aloy M.-Á., 2020b, preprint (arXiv:2008.07205)

Obergaulinger M., Aloy M. A., Müller E., 2006a, A&A, 450, 1107

Obergaulinger M., Aloy M. A., Dimmelmeier H., Müller E., 2006b, A&A, 457, 209

Obergaulinger M., Cerdá-Durán P., Müller E., Aloy M. A., 2009, A&A, 498, 241

Obergaulinger M., Janka H.-T., Aloy M. A., 2014, MNRAS, 445, 3169

Obergaulinger M., Just O., Aloy M. Á., 2018, J. of Phys. G., 45, 084001

Ott C. D., Burrows A., Thompson T. A., Livne E., Walder R., 2006, ApJS, 164, 130

Özel F., Freire P., 2016, ARA&A, 54, 401

Pessah M. E., Chan C., 2008, ApJ, 684, 498

Pons J. A., Reddy S., Prakash M., Lattimer J. M., Miralles J. A., 1999, ApJ, 513, 780

Proga D., 2005, ApJ, 629, 397

Proga D., MacFadyen A. I., Armitage P. J., Begelman M. C., 2003, ApJ, 599, L5

Qian Y. Z., Woosley S. E., 1996, ApJ, 471, 331

Raynaud R., Guilet J., Janka H.-T., Gastine T., 2020, Sci. Adv., 6, eaay2732

Rea N., Gullón M., Pons J. A., Perna R., Dainotti M. G., Miralles J. A., Torres D. F., 2015, ApJ, 813, 92

Reboul-Salze A., Guilet J., Raynaud R., Bugli M., 2020, preprint (arXiv:2005.03567)

Reichert M., Obergaulinger M., Eichler M., Aloy M.-Á., Arcones A., 2020, preprint (arXiv:2010.02227)

Rembiasz T., Obergaulinger M., Cerdá-Durán P., Müller E., Aloy M. A., 2016a, MNRAS, 456, 3782

Rembiasz T., Guilet J., Obergaulinger M., Cerdá-Durán P., Aloy M. A., Müller E., 2016b, MNRAS, 460, 3316

Rembiasz T., Obergaulinger M., Cerdá-Durán P., Aloy M., Müller E., 2016c, J. Phys. Conf. Ser., 719, 012009

Rembiasz T., Obergaulinger M., Cerdá-Durán P., Aloy M.-Á., Müller E., 2017, ApJS, 230, 18

Romanova M. M., Ustyugova G. V., Koldoba A. V., Lovelace R. V. E., 2004, ApJ, 616, L151

Saijo M., Yoshida S., 2006, MNRAS, 368, 1429

Sawai H., Yamada S., Suzuki H., 2013, ApJ, 770, L19

Shibata M., Baumgarte T. W., Shapiro S. L., 2000, ApJ, 542, 453

Spruit H. C., 2002, A&A, 381, 923

Spruit H. C., 2013, preprint (arXiv:1301.5572)

Sukhbold T., Ertl T., Woosley S. E., Brown J. M., Janka H.-T., 2016, ApJ, 821, 38

Symbalisty E. M. D., 1984, ApJ, 285, 729

Taubenberger S. et al., 2006, MNRAS, 371, 1459

Thompson T. A., Chang P., Quataert E., 2004, ApJ, 611, 380

Thompson T. A., Quataert E., Burrows A., 2005, ApJ, 620, 861

Torres-Forné A., Cerdá-Durán P., Pons J. A., Font J. A., 2016, MNRAS, 456, 3813

Ugliano M., Janka H.-T., Marek A., Arcones A., 2012, ApJ, 757, 69

Uzdensky D. A., MacFadyen A. I., 2007, ApJ, 669, 546

van Kerkwijk M. H., Breton R. P., Kulkarni S. R., 2011, ApJ, 728, 95

Watts A. L., Andersson N., Jones D. I., 2005, ApJ, 618, L37

Wheeler J. C., Yi I., Höflich P., Wang L., 2000, ApJ, 537, 810

Winteler C., Käppeli R., Perego A., Arcones A., Vasset N., Nishimura N., Liebendörfer M., Thielemann F.-K., 2012, ApJ, 750, L22

Woosley S. E., Heger A., 2006, ApJ, 637, 914

Woosley S. E., Langer N., Weaver T. A., 1993, ApJ, 411, 823

Woosley S. E., Sukhbold T., Janka H. T., 2020, ApJ, 896, 56

Yoon S.-C., Langer N., 2005, A&A, 443, 643

Yoon S.-C., Langer N., Norman C., 2006, A&A, 460, 199

Zhang B., Kobayashi S., 2005, ApJ, 628, 315

Zhang B., Mészáros P., 2001, ApJ, 552, L35

Zhang W., Woosley S. E., MacFadyen A. I., 2003, ApJ, 586, 356

Zhang W., Woosley S. E., Heger A., 2004, ApJ, 608, 365

APPENDIX A: VARIANCE RESULTING FROM THE MAGNETIC FIELD INITIAL MAPPING

The initial grid of the stellar core 35OC (35OB) consists of 1053 (956) zones covering the range $[0, R_\star]$, where $R_\star$ is the radius of the progenitor star. We only map the inner $\sim 1.2 \times 10^{10}$ cm into our grid, i.e. only the inner 931 (867) zones of the stellar evolution model are mapped into a grid of $n_r \times n_\theta = 400 \times 128$ zones (the radial zones are not uniform; see Section 2). As our radial grid is coarser than that of the stellar evolution model, direct interpolation dissipates part of the energy, $\mathcal{B}^{\rm pol}$, stored in the smallest scales of the poloidal magnetic field ($b_{\rm preSN}^{\rm pol}$). This is neither the case for the toroidal magnetic field ($b_{\rm preSN}^{\rm tor}$) nor for the rest of the physical hydrodynamical variables. In the pre-SN core, $b_{\rm preSN}^{\rm tor}$ is much smoother than $b_{\rm preSN}^{\rm pol}$. The poloidal magnetic field displays a large variability on small scales, close to the grid resolution employed in the stellar evolution code. As a result a sizeable fraction of $\mathcal{B}^{\rm pol}$ resides on scales below the typical size of our numerical grid. This is a consequence of the fact that the magnetic field in the stellar evolution of the models here considered is not based on a consistent MHD modelling, which would result in a smoother distribution of $b_{\rm preSN}^{\rm pol}$ due to the magnetic solenoidal constraint. In the following, we show how different strategies to bridge from $b_{\rm preSN}^{\rm pol}$ to the 2D axisymmetric grid introduce variegated paths in the post-collapse evolution.

Our default procedure to obtain the initial magnetic field consists of setting the ϕ-component of the initial field as

$$b^\phi = \beta_0^\phi b_{\rm preSN}^{\rm tor}, \tag{A1}$$

and computing the r-component from its poloidal component

$$b^r = \beta_0^r b_{\rm preSN}^{\rm pol} \cos(n^r \theta), \tag{A2}$$

where $\beta_0^{\rm r/\phi}$ and n^r are dimensionless parameters (normally, we set $\beta_0^{\rm r/\phi} = n^r = 1$). The θ-component follows directly from the solenoidal condition.

The procedure to map the magnetic field from the 1D stellar evolution models to our 2D (or 3D) computational grids is not unanimously defined. In view of the fact that the small-scale variability of $b_{\rm preSN}^{\rm pol}$ is likely an artefact of the model to include magnetic torques in stellar evolution, we have also considered the possibility of smoothing the stellar evolution profile by taking the running average over several neighbouring zones, i.e. for the radial magnetic field at each radial position, r_i, we consider

$$b_{\rm preSN,smth}^{\rm pol}(r_i) = \frac{1}{2s+1} \sum_{j=i-s}^{i+s} b_{\rm preSN}^{\rm pol}(r_j), \tag{A3}$$

with $s = 10$. We compute b^r using equation (A2), replacing $b_{\rm preSN}^{\rm pol}$ by the smoothed poloidal magnetic field profile, $b_{\rm preSN,smth}^{\rm pol}$. With this
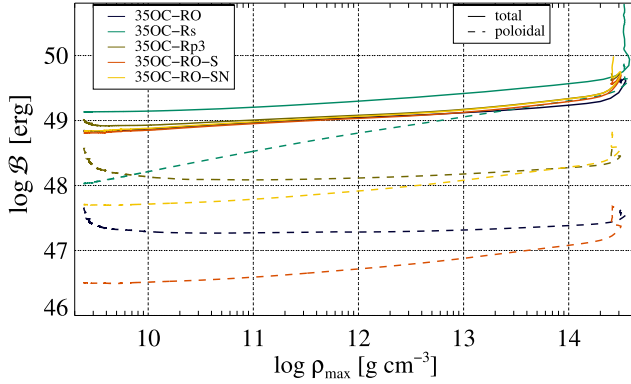
Figure A1. Evolution of $\mathcal{B}$ and of $\mathcal{B}^{pol}$ (solid and dashed lines, respectively) as a function of the maximum rest-mass density until core bounce in the variants of the model 35OC-RO: 35OC-RO with the standard mapping from the stellar evolution model to our 2D grid, 35OC-RO-S with the smoothing of the poloidal magnetic field set by equation (A3) before the mapping to our grid, and 35OC-RO-SN, which in addition to the smoothing includes a renormalisation of $\mathcal{B}^{pol}$ to compensate the energy loss in the smoothing procedure. For comparison, models 35OC-Rp3 and 35OC-Rs are also shown.

procedure we evolve a new setup dubbed 35OC-RO-S. The process of smoothing yields a loss of $\mathcal{B}^{pol}$. In order to avoid it, we renormalize the obtained results selecting appropriately the factor β_0^r, so that the initial energy in the b^{pol} component equals the same quantity in the stellar evolution model. In this way, we setup model 35OC-RO-SN.

Fig. A1 compares the evolution of the magnetic energy as a function of the maximum density in the pre-bounce phase. Model 35OC-RO (blue dashed line) begins its evolution with the same $\mathcal{B}^{pol}$ as model 35OC-RO-SN (yellow dashed line), but after a quick initial readjustment phase, $\mathcal{B}^{pol}$ levels off until the bounce takes place. At that time, $\mathcal{B}^{pol}$ is the same as in the model with the smoothed poloidal magnetic profile (35OC-RO-S; red dashed line). The total magnetic energy (dominated by the contribution of the toroidal magnetic field) runs in parallel for all the variants of the 35OC-RO (yellow, blue, and red solid lines). Thus, we conclude that, during the collapse a significant fraction of $\mathcal{B}^{pol}$ is *dissipated* in model 35OC-RO, (note the difference of a factor ~ 16 between the initial values of $\mathcal{B}^{pol}$ in models 35OC-RO and 35OC-RO-S, which disappears at the time of bounce). The dissipated energy corresponds to the smallest scales mapped from the initial stellar evolution model.

For comparison, we also display in Fig. A1 model 35OC-Rp3, which reaches nearly the same value of $\mathcal{B}^{pol}$ than model 35OC-RO-SN, even having started with an energy in the poloidal magnetic field component ~ 10 times larger than the latter. The pre-bounce evolution of $\mathcal{B}^{pol}$ in model 35OC-Rp3 parallels (at a higher level though) that of model 35OC-RO and, hence, we also conclude that the part of $\mathcal{B}^{pol}$ of the former model stored in the smallest scales has been dissipated as in the latter case.

Finally, Fig. A1 also illustrates the fact that the much smoother poloidal magnetic structure of model 35OC-Rs is more efficiently amplified during collapse as that corresponding to models with similar initial values of $\mathcal{B}^{pol}$, but with (much) more energy stored in smaller scales (e.g. models 35OC-RO-Rp3, 35OC-RO). The growth of $\mathcal{B}^{pol}$ in model 35OC-Rs (green dashed line) is even faster than in the smoothed versions of model 35OC-RO, whose growth until collapse is nearly parallel (though starting from different initial values; compare yellow and red dashed lines). Hence, we conclude
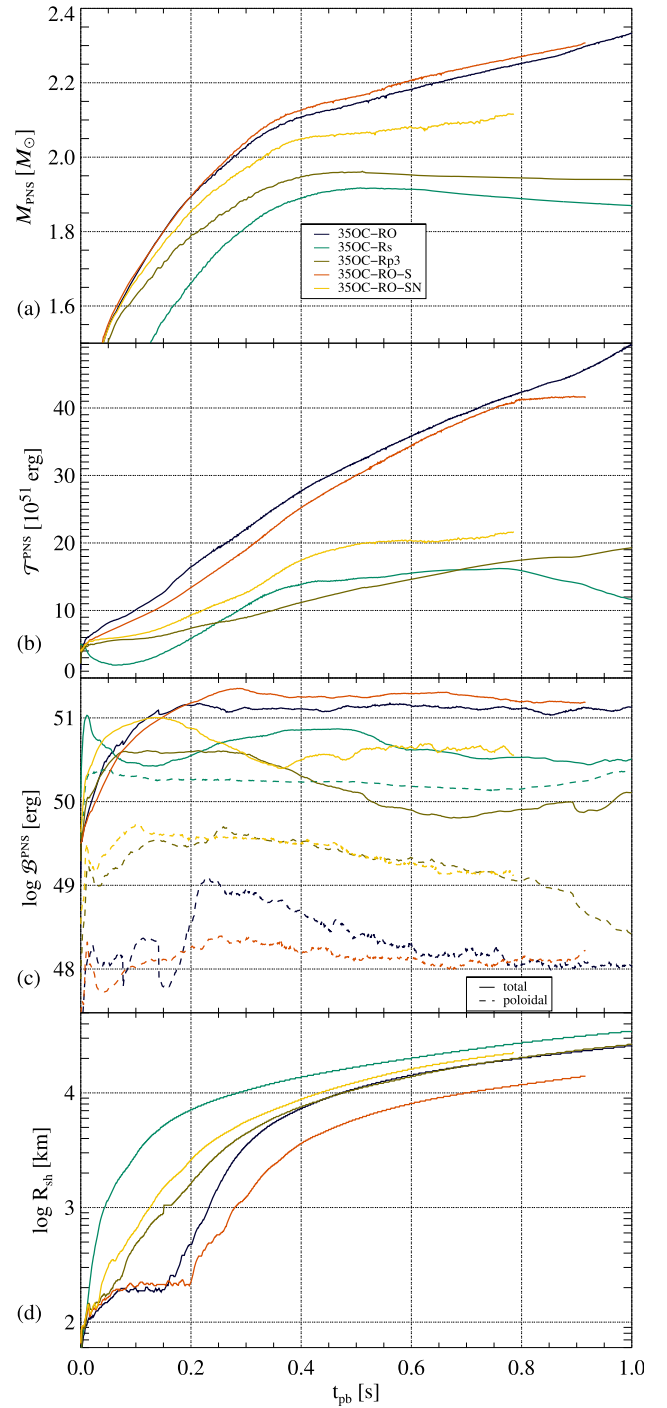
Figure A2. Post-bounce evolution of different quantities of the PNS (from top to bottom panels: mass, rotational energy, and logarithm of the magnetic energy) as well as the shock radius for the same models as in Fig. A1.

that the dissipation of $\mathcal{B}^{pol}$ during collapse is closely connected to the smoothness of the topology of b^{pol}_{presN}.

The variegated evolutions of $\mathcal{B}^{pol}$ resulting from different initial mapping procedures of b^{pol}_{presN} on to our computational grid yields also a significant variance in the post-bounce evolution, which is illustrated in Fig. A2. There, we only consider the first second post-bounce and we can see that the PNS properties are sensitively impacted by the initial mapping. While the model with the smoothed

initial profile follows an evolutionary path very close to our default model `35OC-RO`, model `35OC-RO-SN` displays an smaller PNS mass growth (a), and significantly smaller rotational (b) and magnetic (c) energy. Not only the PNS properties are modified, also the explosion properties, e.g. the shock radius evolution (Fig. A2d). While the model with initially smoothed poloidal magnetic field (red line) develops a successful explosion later than model `35OC-RO`, the model with an smoothed profile and renormalized initial $\mathcal{B}^{\mathrm{pol}}$ yields and early magnetorotational explosion akin to that of model `35OC-Rp3`.

As a final note, the shown pre- and post-bounce evolution of the variants of model `35OC-RO` with smoothing and with/without renormalization, fully justifies our choice of enhancing the poloidal magnetic field component of the original `35OC` pre-SN core and consider the evolution of models `35OC-Rp2`, `35OC-Rp3`, and `35OC-Rp4`.

This paper has been typeset from a TEX/LATEX file prepared by the author.